

---

Electronic Theses and Dissertations, 2004-2019

---

2006

## Fast Response Liquid Crystal Devices

Yung-Hsun Wu  
*University of Central Florida*

 Part of the [Electromagnetics and Photonics Commons](#), and the [Optics Commons](#)  
Find similar works at: <https://stars.library.ucf.edu/etd>  
University of Central Florida Libraries <http://library.ucf.edu>

This Doctoral Dissertation (Open Access) is brought to you for free and open access by STARS. It has been accepted for inclusion in Electronic Theses and Dissertations, 2004-2019 by an authorized administrator of STARS. For more information, please contact [STARS@ucf.edu](mailto:STARS@ucf.edu).

---

### STARS Citation

Wu, Yung-Hsun, "Fast Response Liquid Crystal Devices" (2006). *Electronic Theses and Dissertations, 2004-2019*. 823.  
<https://stars.library.ucf.edu/etd/823>

# **FAST RESPONSE LIQUID CRYSTAL DEVICES**

by

YUNG-HSUN WU

BS in Department of Electro-physics, National Chiao Tung University, 1997

MS in the institute of Electro-optical Engineering, National Chiao Tung University, 1999

A dissertation submitted in partial fulfillment of the requirements  
for the degree of Doctor of Philosophy  
in the College of Optics and Photonics  
at the University of Central Florida  
Orlando, Florida

Spring Term  
2006

Major Professor: Shin-Tson Wu

© 2006 Yung-Hsun Wu

## ABSTRACT

Liquid crystal (LC) has been widely used for displays, spatial light modulators, variable optical attenuators (VOAs) and other tunable photonic devices. The response time of these devices is mainly determined by the employed liquid crystal material. The response time of a LC device depends on the visco-elastic coefficient ( $\gamma_1 / K_{11}$ ), LC cell gap ( $d$ ), and applied voltage. Hence, low visco-elastic coefficient LC materials and thinner cell gap are favorable for reducing the response time. However, low visco-elastic coefficient LCs are usually associated with a low birefringence because of shorter molecular conjugation. For display applications, such as LCD TVs, low birefringence ( $\Delta n < 0.1$ ) LCs are commonly used. However, for optical communications at 1550 nm, low birefringence requires to a thick cell gap which, in turn, increases the response time. How to obtain fast response for the LC devices is a fundamentally important and technically challenging task.

In this dissertation, we investigate several methods to improve liquid crystal response time, for examples, using dual-frequency liquid crystals, polymer stabilized liquid crystals, and sheared polymer network liquid crystals. We discover a new class of material, denoted as sheared polymer network liquid crystal (SPNLC) which exhibits a submillisecond response time. Moreover, this response time is insensitive to the LC cell gap. This is the first LC device exhibiting such an interesting property.

Chapters 1 and 2 describe the motivation and background of this dissertation. From chapter 3 to chapter 6, dual-frequency liquid crystals and polymer network methods are demonstrated as examples for the variable optical attenuators. Variable optical

attenuator (VOA) is a key component in optical communications. Especially, the sheared PNLC VOA shows the best result; its dynamic range reaches 43 dB while the response time is in the submillisecond range at 1550 nm wavelength, which is 50 times faster than the commercial LC-based VOA.

In Chapter 7, we report a new device called axially-symmetric sheared polymer network liquid crystals (AS-SPNLC) and use it as LC devices. Through analyzing the structure of this axially-symmetric SPNLC, we construct a 3-D model to explain the observed phenomena. An axially-symmetric sheared polymer network liquid crystal has several attractive features: 1) it is polarization independent, 2) it has gradient phase change, and 3) its response time is fast. It can be used for polarization converter and divergent LC lens. In addition, a new method for simultaneously measuring the phase retardation and optic axis of a compensation film is demonstrated using an axially-symmetric sheared polymer network liquid crystal. By overlaying a tested compensation film with a calibrated SPNLC cell between crossed polarizers, the optic axis and phase retardation value of the compensation film can be determined. This simple technique can be used for simultaneously measuring the optic axis and phase retardations of both A- and C-plates. These compensation films have been used extensively in wide-view LCD industry. Therefore, this method will make an important impact to the LCD industry.

## **ACKNOWLEDGMENTS**

I would like to express my thankfulness to my advisor, Professor Shin-Tson Wu, for his guidance and support throughout my studies at CREOL, the College of Optics and Photonics in the University of Central Florida. I greatly appreciate his technical insights and providing the laboratory facilities in the development process of this dissertation. I sincerely believe that his advices and directions will benefit my future life both professionally and personally. I highly appreciate his effective mentoring, as I know that without his support, I would not be able to make such impressive achievements, progress and success in my research work.

I would also like to take this chance to express my thankfulness to my Ph.D. committee members, Dr. Glenn D. Boreman, Dr. Nabeel A. Riza, and Dr. Thomas X. Wu for their evaluating this dissertation and my doctoral qualifications.

Appreciations also go to all of my colleagues and friends, especially to Dr. Yanqing Lu, Dr. Ju-Hyun Lee, Dr. Hongwen Ren and Dr. Yun-Hsing Fan. I want to thank them for their help on laboratory experiments and constant supports. The great friendship and entertainment from all these people was an important ingredient in my daily work life.

Finally and foremost, I want to express my sincere appreciations to my parents, Chieh-Ping Chang and Fu-Tsng Wu, for their priceless love and blessings. My mother, Chieh-Ping Chang, contributes her whole life to me and my family. She spent her valuable time and worked hard to nourish my family as a single parent. Without her endless love and nurture, I would not have the accomplishments today.

Most importantly, I want to thank my wife, Yi-Hsin Lin, for her love and help on my research work to make all my dreams possible. I deeply appreciated her supports and discussions on my experiment and thesis. With her help, this thesis becomes more comprehensive.

*To my Parents, Chieh-Ping Chang and Fu-Tsan Wu*

*To my Brother, Yung-Chang Wu*

*To my Wife, Yi-Hsin Lin*



Psalm 111:10-

“The fear of the LORD is the beginning of wisdom”

## TABLE OF CONTENTS

LIST OF FIGURES .....	xiii
LIST OF TABLES .....	xx
LIST OF ACRONYMS/ABBREVIATIONS .....	xxi
LIST OF PUBLICATIONS .....	xxiii
CHAPTER 1: INTRODUCTION .....	1
1.1 Motivation .....	1
1.2 Thesis overview .....	6
CHAPTER 2: INTRODUCTION TO LIQUID CRYSTAL OPTICS .....	10
2.1 Introduction to liquid crystals .....	10
2.2 Physics of liquid crystals .....	12
2.2.1 Liquid crystal order .....	12
2.2.2 Liquid crystal phases .....	13
2.2.3 Electric and magnetic field effects .....	17
2.2.4 Freedericksz transition .....	17
2.2.5 Surface preparations .....	18
2.2.6 Liquid crystal deformation models .....	18
2.3 Optics of liquid crystals .....	20
2.3.1 Light and polarization .....	20
2.3.2 Birefringence of liquid crystals .....	22
2.3.3 EO properties of liquid crystal .....	24
2.4 Polymer network liquid crystal (PNLC) .....	26

2.5 Variable optical attenuator (VOA).....	26
CHAPTER 3: DUAL-FREQUENCY LIQUID CRYSTAL PHASE MODULATORS ..	28
3.1 Theory of dual-frequency liquid crystal .....	28
3.2 Dual-frequency liquid crystal phase modulators for long IR applications .....	31
3.2.1 Sample fabrication .....	31
3.2.2 Experimental results and discussions.....	32
3.3 Dual-frequency addressed variable optical attenuator .....	37
3.3.1 Introduction.....	37
3.3.2 Sample fabrication and experimental setup .....	38
3.3.3 Experimental results.....	41
3.3.4 Discussions .....	46
3.3.5 Conclusion .....	47
CHAPTER 4: DUAL-FREQUENCY ADDRESSED HYBRID-ALIGNED NEMATIC LIQUID CRYSTAL.....	48
4.1 Introduction.....	48
4.2 Operation principle .....	49
4.3 Sample preparation .....	51
4.4 Experimental results and discussions.....	52
4.5 Conclusion .....	57
CHAPTER 5: POLYMER STABILIZED DUAL FREQUENCY LIQUID CRYSTAL MODULATORS.....	58
5.1 Introduction.....	58
5.2 Light Modulation Mechanism for fast response variable optical attenuator .....	59
5.3 Experimental results and discussions.....	61

5.4 Discussion.....	65
5.5 Conclusion .....	67
CHAPTER 6: SHEARED POLYMER NETWORK LIQUID CRYSTALS .....	69
6.1 Introduction.....	69
6.2 Sample fabrication .....	71
6.3 Theory of sheared polymer network liquid crystal.....	71
6.4 Properties of sheared polymer network liquid crystal .....	73
6.4.1 Cell gap independent response time .....	73
6.4.2 SPNLC composite layer.....	77
6.4.3 SPNLC morphologies .....	79
6.5 Sheared vertical aligned polymer network liquid crystal .....	81
6.5.1 Motivation.....	81
6.5.2 VA-SPNLC fabrication process.....	83
6.5.3 Experiment results .....	84
6.5.4 Discussion and future work .....	87
6.6 VOA experiment and results.....	88
6.7 Conclusions.....	96
CHAPTER 7: AXIALLY SYMMETRY SHEARED POLYMER NETWORK LIQUID CRYSTALS .....	97
7.1 Introduction.....	97
7.2 Sample preparation .....	98
7.3 Properties of axially sheared polymer network liquid crystals.....	100
7.3.1 Polarization independence .....	100
7.3.2 Fast response time.....	101

7.3.3 Gradient phase retardation distribution.....	102
7.3.4 AS-SPNLC properties in different diameter.....	107
7.3.5 Physics model of the AS-SPNLC .....	109
7.3.6 Simulation of axially sheared polymer network liquid crystals.....	113
7.4 Formation analysis of the axially sheared polymer network liquid crystals.....	114
7.5 Phase retardation measurement methods using AS-SPNLC .....	119
7.5.1 Introduction.....	119
7.5.2 Measurement methods .....	121
7.5.3 Experimental results.....	125
7.5.4 Discussions .....	127
7.6 Other applications .....	131
7.6.1 Spatial polarization converter .....	131
7.6.2 Tunable-focus liquid crystal lens.....	135
7.7 Conclusion .....	136
LIST OF REFERENCES.....	138

## LIST OF FIGURES

Figure 1: The photo of liquid crystal phases near the nematic to isotropic point. ....	11
Figure 2: The general form of temperature-dependent order parameter of a LC. ....	13
Figure 3: Nematic Liquid crystal phase illustration.....	14
Figure 4: Smectic liquid crystal phase illustration (a) smectic A, (b) smectic C, and (c) smectic C* .....	15
Figure 5: Schematic illustration of cholesteric liquid crystals.....	16
Figure 6: The electric field effect on liquid crystal molecule.....	17
Figure 7: Three LC deformation models (a) splay, (b) twist, and (c) bend .....	19
Figure 8: Illustration of the transverse electromagnetic wave .....	20
Figure 9: (a) Cross polarizer pair (b) Parallel polarizer pair.....	21
Figure 10: (a) 45° linearly polarized light, (b) 135° linearly polarized light, and (c) circularly polarized light. ....	22
Figure 11: (a) Parallel, (b) 45°, and (c) Perpendicular to the LC directors.....	23
Figure 12: The voltage dependent transmittance of a homogeneous cell between crossed and parallel polarizers. ....	25
Figure 13: Dielectric anisotropy $\Delta\epsilon$ ( $\epsilon_{//} - \epsilon_{\perp}$ ) of LCs changes sign from positive (+) to negative (-) while increasing the frequency of applied electric field. ....	29
Figure 14: The operating principles of a VA cell containing DFLC. (a) On state: High frequency driving $\sim 30$ kHz, (b) Off state: low frequency driving $\sim 1$ kHz .....	30
Figure 15: Overdrive and undershoot voltage methods.....	31

Figure 16: Turn-on and -off time of the DFCL-VA cell with overdrive and undershoot voltages. $\lambda=1.55 \mu\text{m}$ and $T=22 \text{ }^\circ\text{C}$ . .....	32
Figure 17: The LC response curves at $\lambda=1.55 \mu\text{m}$ : (a) rise time and (b) decay time. ....	33
Figure 18: Reflective IR projector setup.....	34
Figure 19: Turn-on and turn-off time of the DFCL cell with overdrive and undershoot voltages. $\lambda=1.55 \mu\text{m}$ .....	35
Figure 20: The estimated LC phase response curve at $10.6 \mu\text{m}$ (a) rise time, and (b) decay time.....	36
Figure 21: Schematic diagram of DFCL-based variable optical attenuator, where “1”, “2”, “3” and “4” represent polarization beam displacer, half-wave plate, master LC cell, and compensation cell, respectively.....	39
Figure 22: Measured VOA attenuation on dB scale as function of applied voltage. The VOA is addressed by a 1 kHz square-wave ac source. ....	42
Figure 23: (a) Optical response curves of DFCL VOA when 1 kHz $6 V_{\text{rms}}$ voltage is applied to turn VOA to off state. (b) Optical response curves that reflect LC directors’ relaxation process when applied field is removed. The solid line and dot line correspond to cases without and with a $2 V_{\text{rms}}$ -bias voltage ( $f=1 \text{ kHz}$ ), respectively.....	43
Figure 24: Overdrive and undershoot voltages and corresponding optical responses.....	45
Figure 25: Schematics of a HAN cell. The rods represent the LC molecules with the director orientation of $\phi(z)$ . (a) Initial state at $V=0$ ; (b) a high voltage state at $f < f_c$ ; (c) a high voltage state at $f > f_c$ . ....	50
Figure 26: The measured phase change of an $8.5 \mu\text{m}$ HAN cell as a function of the applied voltage under different driving frequencies. From bottom to top, $f=1, 4, 5.5, 8,$ and $30 \text{ kHz}$ .....	53

Figure 27: The total achievable phase changes of two 8.5 $\mu\text{m}$ LC cells in different alignments. The solid line is for the HAN cell, while the dashed lines are for a homogeneous cell. ....	54
Figure 28: The optical decay time of an 8.5 $\mu\text{m}$ DFLC HAN cell based VOA. The solid line is the normal decay curve by instantly turning off the 5.8 Vrms driving voltage. The dashed lines are for the dual frequency driving, where a 35 ms, 30 kHz voltage burst is used to assist the LC directors relaxation. ....	56
Figure 29: Light modulation mechanism of a PS-DFLC cell. (a) At low frequency (1 kHz), light scattering occurs for the extraordinary ray. (b) At high frequency (30 kHz), the device is highly transparent. ....	60
Figure 30: Polarization independent PS-DFLC-based VOA. HW: Half wave plate, BD: Beam displacer. $\lambda=1.55 \mu\text{m}$ . ....	61
Figure 31: Voltage-dependent transmittance of a PS-DFLC-based VOA. $\lambda=1.55 \mu\text{m}$ . ....	63
Figure 32: Wavelength-dependent attenuation ratio of the PS-DFLC VOA. ....	64
Figure 33: The measured polarization dependent loss (PDL) of the PS-DFLC VOA. $d=16 \mu\text{m}$ . ....	65
Figure 34: Curing temperature dependent response time of a PS-DFLC (circles) and a PSLC (triangles) cells. ....	66
Figure 35: Shearing processes and LC domain orientations of the SPNLC film. (a) Before and (b) after shearing. ....	73
Figure 36: Voltage dependence transmittance curve in various cell gaps. ....	74
Figure 37: Maximum phase retardation change increases with the cell gap. ....	75
Figure 38: Transient phase decay time of four SPNLC cells. ....	76
Figure 39: Relaxation time constant as the function of the cell gaps. ....	77



Figure 40: SPNLC sample with a composite film which has the compensation film effect. .....	78
Figure 41: SPNLC cell with or without a compensator.....	79
Figure 42: SPNLC morphologies (a) without and (b) with a shearing force.....	80
Figure 43: The transmittance with respect to the rotation angle of SPNLC cell.....	81
Figure 44: The VA-SPNLC shearing process.....	84
Figure 45: The voltage dependent transmittance curve of the VA SPNLC and pure E44 sample between crossed polarizers. The cell gap $d \sim 9 \mu\text{m}$ , and $\lambda = 1.55 \mu\text{m}$ .....	85
Figure 46: Optical response time of the VA-SPNLC cell at $V = 160 V_{\text{rms}}$ : (a) rise time, and (b) decay time. Cell gap $d \sim 9 \mu\text{m}$ and $\lambda = 1.55 \mu\text{m}$ . ....	86
Figure 47: Optical response time of the VA-SPNLC cell at $V = 75 V_{\text{rms}}$ : (a) rise time, and (b) decay time. Cell gap $d \sim 9 \mu\text{m}$ and $\lambda = 1.55 \mu\text{m}$ . ....	87
Figure 48: The schematic diagram of a SPNLC-based VOA. ....	89
Figure 49: The detailed operation mechanisms of the phase modulator module: (a) VOA ON state, $V = 0$ , and (b) VOA OFF state, $V = 35 V_{\text{rms}}$ . HW: half-wave plate, QW: quarter-wave plate, and SPNLC: sheared polymer network liquid crystal. ....	91
Figure 50: The VOA attenuation at different drive voltages. $\lambda = 1.55 \mu\text{m}$ . ....	92
Figure 51: Optical response time of the 9- $\mu\text{m}$ SPNLC VOA: (a) decay time, and (b) rise time.....	93
Figure 52: Wavelength-dependent transmittance of the E7 SPNLC cell. $d \sim 9 \mu\text{m}$ . ....	95
Figure 53: The wavelength-dependent attenuations of the VOA at different attenuation range.....	96
Figure 54: The illustration of the off-axis shearing of the SPNLC cell.....	99
Figure 55: SPNLC structure observed under crossed polarizers. ....	100

Figure 56: Voltage-dependent transmittance of the axially symmetric SPNLC cell. $d=9$ $\mu\text{m}$ and $\lambda=633$ nm. ....	101
Figure 57: Optical response time of the 9- $\mu\text{m}$ axially-symmetric SPNLC: (a) rise time, and (b) decay time. ....	102
Figure 58: (a) Top view and cross-section of the LC structure; (b) Measured gradient distribution of the phase retardation. ....	103
Figure 59: Simulated pretilt angle distribution of the axially-symmetric SPNLC cell... ..	104
Figure 60: Measured V-T curves at different positions of the axially-symmetric SPNLC cell. ....	105
Figure 61: Measured response time at different positions of the axially-symmetric SPNLC cell.....	106
Figure 62: Experimental setup for measuring the AS-SPNLC properties in different diameter .....	107
Figure 63: Diameter definitions of the axially symmetric SPNLC structure.....	108
Figure 64: The simulation results of the elastic constant v.s. voltage-dependent transmittance (VT) curve as the elastic constants increase from 10 to 600 times.....	110
Figure 65: Elastic constants v.s. LC response time curve.....	111
Figure 66: VT-curves of different weak surface anchoring factors .....	112
Figure 67: Simulation and experimental results of the AS-SPNLC .....	113
Figure 68: (a) Experimental results when a voltage is applied to the AS-SPNLC, and (b) simulated results. ....	114
Figure 69: (a)-(f) A sequential change of the pattern while pushing the top glass substrate. ....	116

Figure 70: Illustration of external force and movement of the liquid crystal directors (a) initial state, and (b) relaxed state.....	117
Figure 71: An example of the bulk distortion.....	118
Figure 72: Top view and side view of the cell distortion.....	118
Figure 73: Soleil-Babinet compensator measurement method.....	120
Figure 74: PEM compensator measurement method.....	120
Figure 75: Phase retardation ( $d\Delta n$ ) profile of the axially-symmetric SPNLC layer. Cell gap $d=9\ \mu\text{m}$ .....	122
Figure 76: (a) Measurement setup and (b) illustration of the measurement methods. ....	123
Figure 77: The measurement setup of the C-plate.....	124
Figure 78: (a) The transmitted image recorded by a CCD camera, and (b) the converted transmittance distribution.....	126
Figure 79: (a) The relative distance of the two transmission minima recorded by a CCD camera. (b) The corresponding phase retardation of the quarter-wave film. ....	127
Figure 80: CCD images taken under three different color filters (a) 486 nm, (b) 532 nm, and (c) 632 nm.....	128
Figure 81: (a) A series of pictures show the real dynamic image changes when the quarter-wave plate rotates at different angles; and (b) The simulation results show the same trend when we rotate the slow axis of the quarter-wave plate from $0^\circ$ to $135^\circ$ ...	130
Figure 82: Polarized light of orders (a) $P = 1$ , (b) $P = 2$ , and (c) $P = 3$ analyzed with a linear polarizer.....	132
Figure 83: Methods for generating the radially and azimuthally polarized light using circularly rubbing cell. ....	133

Figure 84: Generation of the spatial polarized light using interference of two linearly polarized beams .....	134
Figure 85: (a) Incident light with vertical linear polarization, (b) Rotationally symmetric half wave plate, and (c) Output light with polarization P=2 field.....	135
Figure 86: A tunable-focus lens using AS-SPNLC .....	136

## LIST OF TABLES

Table 1: Specifications of the VOA (from Lightwaves2020 Company <a href="http://www.lightwaves2020.com">http://www.lightwaves2020.com</a> ).....	27
Table 2: Response time results of AS-SPNLC properties in different diameter .....	109
Table 3: Linear polarized light with axially symmetry properties.....	132

## **LIST OF ACRONYMS/ABBREVIATIONS**

3-D	Three-Dimensions, Three-Dimensional
AS-SPNLC	Axially Symmetry Shear Polymer Network Liquid Crystal
CCD	Charge Coupled Device
CR	Contrast Ratio
CREOL	Center for Research and Education in Optics and Lasers
DFLC	Dual Frequency Liquid Crystal
PS-DFLC	Polymer-Stabilized Dual Frequency Liquid Crystal
FPCE	Florida Photonics Center of Excellence
GRIN	Gradient-Index
He-Ne	Helium-Neon
Hz	Hertz
HW	Half wave plate
IP	Integral Photography
IR	Infrared
ITO	Indium-tin-oxide
kHz	Kilo-Hertz
LC	Liquid Crystal
LCD	Liquid Crystal Display
MBBA	(4-methoxybenzylidene)-4'-butylbenzenamine
NOA	Norland Optical Adhesives
PI	Polyimide

PDL	Polarization dependent loss
PDLC	Polymer-Dispersed Liquid Crystal
PNLC	Polymer Network Liquid Crystal
PSLC	Polymer-Stabilized Liquid Crystal
PBS	Polarizing Beam Splitter
QW	Quarter Wave Plate
UV	Ultraviolet
VA-SPNLC	Vertical Aligned Shear Polymer Network Liquid Crystal
VOA	Variable Optical Attenuator

## LIST OF PUBLICATIONS

### **Journal papers:**

1. Y. H. Wu, Y. H. Lin, J. H. Lee, H. Ren, X. Nie , and S. T. Wu,"Axially-symmetric sheared polymer network liquid crystals and applications", Mol. Cryst. Liq. Cryst. (Accepted, 2006)
2. Y. H. Lin, H. Ren, S. Gauza, Y. H. Wu, Y. Zhou, and S. T. Wu,"High contrast and fast response polarization-independent reflective display using a dye-doped dual-frequency liquid crystal gel", Mol. Cryst. Liq. Cryst. (Accepted, 2006)
3. X. Nie, T. X. Wu, Y. Lu, Y. H. Wu, X. Liang, and S. T. Wu, "Dual-frequency addressed infrared phase modulator with sub-millisecond response", Mol. Cryst. Liq. Cryst. (Accepted, 2006)
4. Y. H. Lin, H. Ren, S. Gauza, Y. H. Wu, Y. Zhao, J. Fang, and S. T. Wu, "IPS-LCD using a glass substrate and an anisotropic polymer film," J. Display Technology **2**, 21-25 (March, 2006)
5. Y. H. Lin, H. Ren, S. Gauza, Y. H. Wu, X. Liang, and S. T. Wu," Reflective direct-view displays using a dye-doped dual-frequency liquid crystal gel," J. Display Technology **1**, 230-233 (Dec. 2005)
6. Y. H. Lin, H. Ren, Y. H. Wu, Y. Zhao, J. Fang, Z. Ge and S. T. Wu, "Polarization-independent liquid crystal phase modulator using a thin polymer-separated double-layered structure," Opt. Express **13**, 8746-8752 (Oct. 31, 2005)



7. J. H. Lee, D. W. Kim, Y. H. Wu, C. J. Yu, S. D. Lee, and S. T. Wu, "High-speed infrared phase modulators using short helical pitch ferroelectric liquid crystals," *Opt. Express* **13**, 7732-7740 (Oct. 3, 2005).
8. Y. H. Wu, J. H. Lee, Y. H. Lin, H. Ren and S. T. Wu, "Simultaneous measurement of phase retardation and optical axis using an axially-symmetric sheared polymer network liquid crystal," *Opt. Express* **13**, 7045-7051 (Sept. 5, 2005).
9. Y. H. Lin, H. Ren, Y. H. Fan, Y. H. Wu, and S. T. Wu, "Polarization-independent and fast-response phase modulation using a normal-mode polymer-stabilized cholesteric texture," *J. Appl. Phys.* **98**, 043112 (August 15, 2005).
10. Y. H. Wu, X. Liang, Y. Q. Lu, Fang Du, Y. H. Lin, and S. T. Wu "Variable optical attenuator using polymer-stabilized dual-frequency liquid crystal," *Appl. Opt.* **44**, 4394-4397 (July 10, 2005).
11. Y. H. Wu, Y. H. Lin, H. Ren, X. Nie, J. H. Lee, and S. T. Wu, "Axially-symmetric sheared polymer network liquid crystals," *Opt. Express* **13**, 4638-4644 (June 13, 2005).
12. X. Liang, Y. Q. Lu, Y. H. Wu, F. Du, H.Y. Wang and S. T. Wu "Dual-frequency addressed variable optical attenuator with submillisecond response time," *Jpn. J. Appl. Phys.* **44**, 1292-1295 (Mar. 8, 2005).
13. Y. H. Lin, H. Ren, Y. H. Wu, X. Liang and S. T. Wu, "Pinning effect on the phase separation dynamics of thin polymer-dispersed liquid crystals," *Optics Express* **13**, 468-474 (Jan. 24, 2005).
14. Y. Q. Lu, F. Du, Y. H. Wu, and S. T. Wu "Liquid crystal based Fourier optical spectrum analyzer without moving parts," *Jpn. J. Appl. Phys.* **44**, 291-293 (Jan. 11, 2005).

15. Y. H. Wu, Y. H. Lin, Y. Q. Lu, H. Ren, Y. H. Fan, J. R. Wu, and S.T. Wu, "Submillisecond response variable optical attenuator based on sheared polymer network liquid crystal," Opt. Express **12**, 6377-6384 (Dec. 13, 2004).
16. Y. Q. Lu, X. Liang, Y. H. Wu, F. Du, and S. T. Wu "Dual-frequency addressed hybrid-aligned nematic liquid crystal," Appl. Phys. Lett. **85**, 3354-6 (Oct. 18, 2004).
17. Jin-Jei Wu, Fu-Chen Chen, Yeong-Shiun Wu and Shu-Hsia Chen, "Phase Gratings in Pretilted Homeotropic Cholesteric Liquid Crystal Films," Jpn. J. Appl. Phys. **41**, 6108-6109 (Oct.15, 2002).
18. Jin-Jei Wu, Yeong-Shiun Wu, Fu-Chen Chen and Shu-Hsia Chen, "Formation of Phase Grating in Planar Aligned Cholesteric Liquid Crystal Film," Jpn. J. Appl. Phys. **41**, L1318-L1320 (Nov.15, 2002).

**Conference paper:**

1. Y. H. Wu, J. H. Lee ,Y. H. Lin, H. Ren and S. T. Wu, "A New Method for Simultaneous Measurement of Phase Retardation and Optical Axis of a Compensation Film", SPIE Photonics West (Jan. 21, 2006) (Invited Talk).
2. Y. H. Wu and S. T. Wu, "Axially-symmetric sheared polymer network liquid crystals and applications", ROC Taiwan Liquid Crystal Society annual meeting (Dec. 30, 2005) (Invited Talk)
3. S. T. Wu, Y. H. Lin, H. Ren, Y. H. Wu, Y. Zhao, J. Fang, and S. Gauza, "Novel liquid crystal alignment layer using an anisotropic polymer film", (Invited Talk) The 61<sup>st</sup> Southwest and the 57<sup>th</sup> Southeast Joint Regional Meeting of the American Chemical society ( Memphis, Nov. 1-4, 2005)

4. Y. H. Wu, Y. H. Lin, J. H. Lee, H. Ren, X. Nie and S.T. Wu, "Axially-symmetric sheared polymer network liquid crystals and applications", The 11th International topical meeting on optics of liquid crystal, 164 (Florida, Oct. 2-7, 2005)
5. Y. H. Lin, H. Ren, S. Gauza, Y.H. Wu, and S.T. Wu, "High contrast and fast response polarization-independent reflective display using a dye-doped dual-frequency liquid crystal gel", The 11th International topical meeting on optics of liquid crystal, 154 (Florida, Oct. 2-7, 2005)
6. Y. H. Lin, H. Ren, Y. H. Wu, X. Liang and S. T. Wu, „Surface pinning effect of thin polymer-dispersed liquid crystals“, Proc. Of the 3<sup>rd</sup> student-organizing international mini-conference on information electronics system (SOIM-COE05), 107-110 (Sendai, Japan, Oct. 6-7, 2005) (Invited Lecture).
7. Y. H. Lin, H. Ren, S. Gauza, Y. H. Wu, and S. T. Wu, “ High contrast and fast response polarization-independent reflective display using a dye-doped dual-frequency liquid crystal gel”, 11<sup>th</sup> International topical meeting on optics of liquid crystal, 154 (Florida, Oct. 2-7, 2005)
8. Y. H. Wu, Y. H. Lin, Y. Q. Lu, H. Ren, Y. H. Fan, J. R. Wu, and S.T. Wu, “Sheared polymer network liquid crystal for fast-response variable optical attenuators”, SPIE 50th Annual Meeting (San Diego, 31 July - 4 August, 2005)
9. Y. H. Lin, H. Ren, S. Gauza, Y. H. Wu, and S. T. Wu,“ Single-substrate IPS-LCD using an anisotropic polymer film”, SPIE 50th Annual Meeting (San Diego, 31 July - 4 August, 2005)
10. Y. H. Lin, H. Ren, Y. H. Wu, X. Liang and S. T. Wu, “Surface Anchoring Effect on the Morphology and Performance of PDLC” Photonics West (Jan, 2005) (Invited Talk).

11. Y. H. Lin, H. Ren, Y. H. Wu, X. Liang and S. T. Wu “High Contrast Reflective Display using a Polymer-Dispersed Liquid Crystal” 17th IEEE/LEOS Annual Meeting, Puerto Rico, 39-40 (2004).
12. S. Gauza, C. H. Wen, B. Tan, Y. H. Wu, Y. H. Lin and S. T. Wu “High-birefringence and low-viscosity isothiocyanate liquid crystals and applications to 50- $\mu$ s response switching device” SID Tech. Digest 35, 1304-7 (2004).
13. J. J. Wu, Fu-Chen Chen and Shu-Hsia chen, “Diffraction of the phase grating in a planar-parallel aligned cholesteric liquid crystal (CLC) film,” 19th International Liquid Crystal Conference, Edinburgh, U.K. (2002).
14. Shu-Hsia Chen, Yeong-Shiun Wu, Fu-Chen Chen and J. J. Wu, “Cholesteric liquid crystal (CLC) phase grating used as a pre-polarizer,” 19th International Liquid Crystal Conference, Edinburgh, U.K. (2002).
15. Hiap L. Ong, Yung-Hsun Wu, “New Two-Domain TN/LCD with Identical, Symmetrical and  $\pm 80^\circ$  Viewing Cone in Left, Right, Up and Down Viewing Zones “, SPIE Conference on Display Technologies III, July 26-28, (2000). (Invited Talk)
16. Chih-Yeong Hsieh, Yeong-Shiun Wu, Yang-An Wu and Shu-Hsia Chen, ”The Optimization of Compensation Films for TNLCDs”, ASID’99, (1999).
17. Yeong-Shiun Wu, Chih-Yeong Hsieh, Yang-An Wu and Shu-Hsia Chen, “The compensation films for TN-LCDs using the O-plates and C-plates”, International Chinese Liquid Crystal Seminar, (1998).
18. Yeong-Shiun Wu, Jin-Jei Wu, Y. C. Chen and Shu-Hsia Chen, “Electro-optical properties of the cholesteric liquid crystal film”, International Chinese Liquid Crystal Seminar, (1998)

# CHAPTER 1: INTRODUCTION

## 1.1 Motivation

Liquid crystal (LC) has been used extensively for information display, laser beam steering, spatial light modulator, tunable photonic crystal, and variable optical attenuator (VOA). For most applications, fast response time and high contrast ratio are key issues. Therefore, it is important to develop fast-response LC modulators.

The response time of a LC device is mainly determined by the visco-elastic coefficient ( $\gamma_1/K_{11}$ ), LC cell gap ( $d$ ), and applied voltage<sup>1</sup>. In the infrared region, to achieve  $1\pi$  phase retardation using a homogeneous cell the required  $d\Delta n$  (where  $\Delta n$  is the LC birefringence) is  $\lambda/2$ . High birefringence LC materials<sup>2</sup> help to reduce the required cell gap and therefore reduce the response time. However, high birefringence liquid crystals are usually associated with an increased viscosity and high melting temperature.

To obtain fast response time at room temperature, various polymer-stabilized liquid crystal (PSLC; also known as anisotropic gel) approaches have been investigated.<sup>3,4,5,6</sup> In a PSLC, the polymer concentration is 3-8 wt %. The response time decreases as the polymer concentration increases. Two problems associated with the LC gels are strong light scattering and high operating voltage. As the polymer concentration increases, the operating voltage increases substantially.

Recently, stressed liquid crystal<sup>7</sup> and polymer-network liquid crystal (PNLC)<sup>8</sup> have been developed for achieving fast response time and scattering-free phase modulators. In a PNLC, rod-like monomers are used and the substrate surfaces are treated with homogeneous alignment. Usually, a PNLC exhibits strong light scattering in the visible spectral region. To suppress light scattering at  $\lambda=1.55 \mu\text{m}$ , a minimal polymer concentration of  $\sim 10\%$  is required in order to make domain sizes smaller than the wavelength. Under such a circumstance, the LC domains are surrounded by polymer networks so that the required operating voltage is increased substantially ( $\sim 7 V_{rms} / \mu\text{m}$ ).

For dynamic infrared scene projection, high contrast ratio and fast response time are two critical issues. High contrast enables us to distinguish the background noises and fast response time allows us to detect the incoming threats. Homeotropic LC alignment offers an unprecedented contrast ratio for a broadband infrared light source. The dual-frequency LC exhibits a cross-over frequency ( $f_c$ ) where  $\Delta\epsilon$  changes sign. In the low frequency regime ( $f < f_c$ ),  $\Delta\epsilon$  is positive and at  $f > f_c$   $\Delta\epsilon$  becomes negative. When a dual-frequency LC is aligned in a homeotropic cell, we apply a high-frequency electric field to reorient the LC directors and apply a low-frequency electric field to assist LC directors decay. As a result, both fast rise and decay times can be obtained.

Mechanical shearing of LC layer has been investigated on the starching plasticized PVA films containing 5-20 wt % LC for making scattering-type polarizers.<sup>9,10</sup> Similar shearing technique has also been applied to the polymer-dispersed LC composites for improving response time and reducing light scattering.<sup>7,11</sup> The major difference between stressed LC and PNLC is that the stressed LC uses a softer monomer NOA-65 ( $\sim 15 \text{ wt } \%$ ) and does not require surface alignment. A major technical challenge for the stressed LC is that it requires mechanical shearing after the two-step UV curing in order

to eliminate light scattering. Before shearing, the cell scatters light strongly. After shearing, the cell becomes highly transparent in the near IR region. The stressed LC has potential for display applications, provided that the operating voltage can be reduced and the light scattering in the blue region can be eliminated.

To obtain submillisecond response time, we have studied several methods: 1) dual-frequency liquid crystal (DFLC) with overdrive and undershoot voltages, 2) dual-frequency addressed hybrid-aligned liquid crystal, 3) polymer stabilized dual-frequency liquid crystal (PS-DFLC), and 4) sheared polymer network liquid crystal (SPNLC).

During developing the sheared polymer network liquid crystal (SPNLC), we discover the axially-symmetric sheared polymer network liquid crystal (AS-SPNLC). An axially-symmetric liquid crystal (LC) structure can be used as a wavelength selection Fabry-Perot filter and a spatial polarization converter. A particularly attractive feature of the axially-symmetric LC structure is its polarization independence because the LC directors are oriented symmetrically in the radial directions. Therefore, we can use it as an optical device which is insensitive to the polarization change<sup>12</sup>. Besides, there is an emerging interest in developing the space-variant polarized light with axial symmetry.<sup>13,14,15</sup> Several approaches for achieving this kind of spatial polarization characteristic has been explored. One approach uses the interference of two linearly polarized beams.<sup>16</sup> The major shortcoming of this method is the relatively low light efficiency and complicated fabrication process. Others use special LC cells with circularly rubbing<sup>13,14</sup> or subwavelength gratings<sup>15</sup> to realize the radially or azimuthally polarized light. However, these approaches require a complicated fabrication procedure such as circular rubbing or micro-fabrication process.

To provide a better solution, we have proposed an axially-symmetric sheared polymer network liquid crystal (AS-SPNLC).<sup>7,17</sup> This structure has attractive features such as fast response time and polarization independence. However, the physical mechanism and structure formation are not yet completely understood. In this paper, we explore the formation processes of an AS-SPNLC structure. By observing of the pattern change of the sheared polymer network liquid crystal (SPNLC) structure, we investigate the formation mechanism of the AS-SPNLC. Besides, through analyzing the structure of the AS-SPNLC, we construct a 3-dimensional model to explain the observed phenomena. The simulation results agree well with experiment. The AS-SPNLC can be used as a tunable-focus negative lens and a spatial polarization converter.

Phase compensation films play an important role for improving the viewing angle and contrast ratio of liquid crystal display devices. Refractive indices and optic axis are the two most critical parameters for a compensation film. Several methods, such as Soleil-Babinet compensator and photoelastic modulator, have been developed for measuring the phase retardation value of a phase compensation film.<sup>18,19,20,21,22</sup> The former is a mechanically adjustable retardation plate using two crystal wedges and the latter is an electrically controllable compensator. By analyzing the modulated signal from photoelastic modulators, we can determine the phase retardation information. The major shortcoming of these methods is that they cannot determine the retardation and optical axis simultaneously.

In this thesis, we develop a new method for simultaneous detection of phase retardation and optic axis of a phase compensation film using an Axially-Symmetric Sheared Polymer Network Liquid Crystal (AS-SPNLC).<sup>17,23</sup> The AS-SPNLC is a liquid crystal structure with a radial director distribution. After shearing, the LC directors align



toward the center of the pattern. Polymer network forms a radial structure and constrains the LC directors within a circle. The formation of the axially-symmetric structure is caused by the external force toward the center. This external force is generated by the distortion of the liquid crystal bulk while applying an off-axis torque to the SPNLC. The axially-symmetric SPNLC exhibits two unique features: 1) its optic axis is radial in all directions, and 2) its phase retardation has a gradient distribution from center to edges. In experiment, we first characterize the phase retardation profile of our axially-symmetric SPNLC film. Then we overlay a phase compensation film, whose retardation value and optical axis is yet to be determined, on top of our SPNLC film. The transmitted image between crossed polarizers is recorded by a CCD camera. After analyzing the compensation pattern of the CCD image, we can precisely identify the phase retardation value and optical axis of the tested phase compensation film. To demonstrate this powerful technique, we use a quarter-wave plate with an arbitrary axis as an example to illustrate the measurement principles. Excellent agreement between experiment and simulation is obtained. This new method is particularly useful for those optical systems whose optical axis and phase retardation are dynamically changing.

## **1.2 Thesis overview**

The research work of this thesis can be divided into several parts. We develop several methods to improve the liquid crystal response time, such as using pure dual-frequency liquid crystals, polymer stabilized liquid crystals and sheared polymer network liquid crystals. In this thesis, we not only develop new driving methods but also discover a new material, SPNLC, to shorten the response time of liquid crystal devices. Variable optical attenuator (VOA) <sup>34,35,36,71,72</sup> is a key component in optical communications. Several variable optical attenuators are demonstrated by using the above methods in this thesis. They show faster response time than the commercial LC based VOA. One of them also shows a submillisecond response time which is 50 times faster than that of the prior art. Meanwhile, we also discover the axially-symmetric sheared polymer network liquid crystals and demonstrate its applications. An axially-symmetric sheared polymer network liquid crystal has several attractive features, such as polarization independence, gradient phase change, and fast response time. It can be used for polarization converter, negative LC lens and phase retardation reader. The thesis is organized as follows:

In Chapter 2, a brief review of the liquid crystal optics and the basic applications of the liquid crystal devices are given. We will start from the history of the liquid crystal and basic liquid crystal physics. These basic liquid crystal properties include the dielectric constants, birefringence and viscosity. The electro-optical properties of LC such as phase retardation, voltage-dependent transmittance curve and response time issues are also discussed. At the end of this chapter, the common LC based applications

such as variable optical attenuators and the polymer network liquid crystals are discussed as well.

In Chapter 3, we present a submillisecond response time and low-voltage variable optical attenuator (VOA) using a dual-frequency liquid crystal. The dynamic range of the VOA reaches 43 dB at a 1.55  $\mu\text{m}$  wavelength. A normally on VOA with a flat wavelength response is obtained using a phase compensation cell. Fast rise and decay times are achieved using low-frequency overdrive and high-frequency undershoot voltages. Other approaches to further improve the VOA's performances are discussed.

In Chapter 4, we show a dual-frequency addressed hybrid-aligned nematic (HAN) liquid crystal cell as a variable optical attenuator at 1.55  $\mu\text{m}$  wavelength. By controlling the low- and high-frequency electric fields, the dual-frequency liquid crystal (DFLC) directors can be reoriented parallel or perpendicular to the substrates so that the maximum obtainable phase modulation is doubled. In comparison to a homogeneous cell, the DF LC HAN cell shows a lower operating voltage and faster response time. Furthermore, the DF LC HAN cell exhibits three stable states that have some applications such as ternary photonic devices.

In Chapter 5, a transmission-type variable optical attenuator based on polymer-stabilized dual-frequency liquid crystal (PS-DFLC) is demonstrated at  $\lambda=1.55$   $\mu\text{m}$ . The VOA is highly transparent in the voltage-off state but scatters light in the voltage-on state. By using a birefringent beam displacer incorporated with half-wave plates, the VOA is polarization independent and exhibits a 31 dB dynamic range. The polymer networks and dual-frequency effect together reduce the response time (rise + decay) of a 16- $\mu\text{m}$  PS-DFLC cell to 30 ms at room temperature and  $V=24$   $V_{\text{rms}}$ .

Chapter 6 demonstrates a VOA at  $\lambda=1.55 \mu\text{m}$  using a sheared polymer network liquid crystal (SPNLC). The SPNLC exhibits a fast response time and weak wavelength dependency. In comparison to other polymer-stabilized liquid crystals, the SPNLC has lower driving voltage and negligible light scattering loss when the wavelength exceeds 700 nm. A reflection type VOA with  $\sim 0.24$  ms response time and  $-32$  dB dynamic range is demonstrated at room temperature and  $35 V_{\text{rms}}$  voltage.

Chapter 7 shows an axially-symmetric sheared polymer network liquid crystal (AS-SPNLC) device. Its properties and performances are characterized. Because of the axial symmetry, the device is polarization independent using the radially polarized light. Through analyzing the structure of this axially-symmetric SPNLC, we construct a 3-D model to explain the observed phenomena. The simulation results agree well with the experiment. The formation mechanism of the AS-SPNLC is also investigated by observing the dynamic pattern change of the structure during the fabrication process. We also analyze the structure from the electro-optic properties and then construct a simulation model to explain the observed phenomena. Several potential applications, such as tunable-focus negative lens and spatial polarization converter, are discussed.

Moreover, a new method for simultaneously measuring the phase retardation and optic axis of a compensation film is demonstrated using an axially-symmetric sheared polymer network liquid crystal (SPNLC). By overlaying a tested compensation film with a calibrated SPNLC cell between crossed polarizers, two dark spots are clearly observed in a CCD image. From the orientation direction and distance of these two spots, the optic axis and phase retardation value of the compensation film can be determined. This method is particularly useful for those optical systems whose optic axis and phase retardation are dynamically changing. It also can be used for measuring phase

retardations of both A- and C-plates. These compensation films have been used extensively in wide-view LCD industry and will make an important impact to the LCD industry.

## CHAPTER 2: INTRODUCTION TO LIQUID CRYSTAL OPTICS

### 2.1 Introduction to liquid crystals

The liquid crystalline state has been known for more than a century.<sup>24</sup> In 1888, the Austrian botanist Friedrich Reinitzer, working at the University of Prague, discovered a strange phenomenon. He noted that cholesteryl benzoate exhibits two melting points;<sup>25</sup> At 145.5°C, the solid crystal is melted into a cloudy liquid and then suddenly disappeared until 178.5°C and became a clear transparent liquid. Reinitzer realized that the cloudy liquid was a new matter state and he named it "liquid crystal" (LC). The new state of matter is lying between liquid and solid and has important properties of both liquid and solid. Another key person in the history of liquid crystals was George Friedel whose work was on the classification of liquid crystal phases.<sup>26</sup> Friedel's work led to recognition that liquid crystal is a separate phase of matter which is different from liquid and crystalline phases. Therefore, he introduced the term *mesophase* (meaning 'in-between' phase) as an alternative name for liquid crystal phases and the term *mesogen* for the molecules that form these phases.

Between 1910 and 1930, many important experiments and theories supported the liquid crystal concept. Several new types of liquid crystalline states of order were discovered at that time as well. In the 1960s, a French physicist, Pierre-Gilles de Gennes, who had been working with magnetism and superconductivity, turned his interest to liquid crystals and soon discovered the liquid crystals as magnetic materials. He won the

1991 Nobel Prize in Physics. Until today, many modern liquid crystal sciences and technologies are affected by the work of de Gennes.

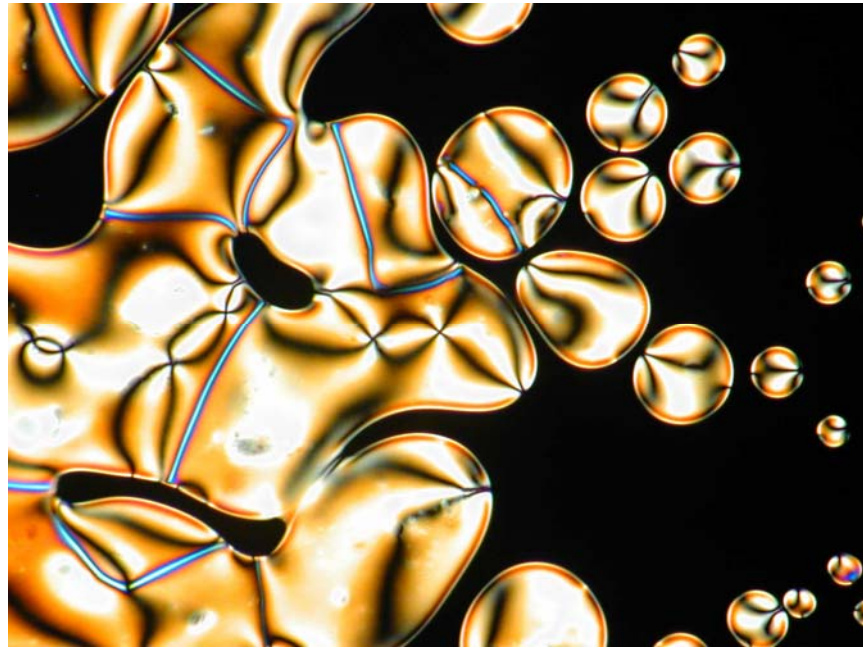


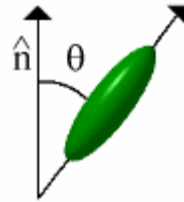
Figure 1: The photo of liquid crystal phases near the nematic to isotropic point.

Figure 1 shows the photograph of liquid crystal phases near the nematic to isotropic (NI) point viewed using a polarized optical microscope. The liquid crystals in the photo show different domains divided by the disclination lines. The dark portion shows the liquid phase, which is over the NI point. Therefore, there is no phase change in that area. Liquid crystals are partially ordered materials between their solid and liquid phases. The order of liquid crystals can be controlled by the electric or magnetic fields. The LC molecules can have rod-like or layered structure. They can be aligned along a certain direction. Moreover, liquid crystals are also temperature sensitive. They turn into solid if it is too cold and into liquid if it is too hot. For example, this phenomenon can be observed on some thermometers which are made by the cholesteric liquid crystals.

## 2.2 Physics of liquid crystals

### 2.2.1 Liquid crystal order

Order parameter is an important parameter for liquid crystal materials. To define how much order is present in a LC material, an order parameter ( $S$ ) is defined as follows:



$$S = \frac{1}{2} \langle 3 \cos^2 \theta - 1 \rangle \quad (1)$$

where  $\theta$  is the angle between the LC director ( $\hat{n}$ ) and the long optic axis of molecules. This is an average statistical effect of the liquid crystal molecules because of the molecular thermal fluctuations. The equation is an average over all of the molecules in the sample. The average of the cosine terms is zero for an isotropic liquid. Therefore, the order parameter of an isotropic liquid is zero. In contrast, the order parameter equals to unit for a perfect crystal. General speaking, the order parameter of a liquid crystal is between 0.3 and 0.9. Actually, the order parameter is sensitive to the temperature. Figure 2 shows the general temperature dependency of a LC order parameter. As the temperature increases, the order parameter decreases and then vanishes abruptly as the temperature approaches the clearing point. This is because the liquid crystal becomes isotropic phase like water and the long range order disappears in the isotropic state.



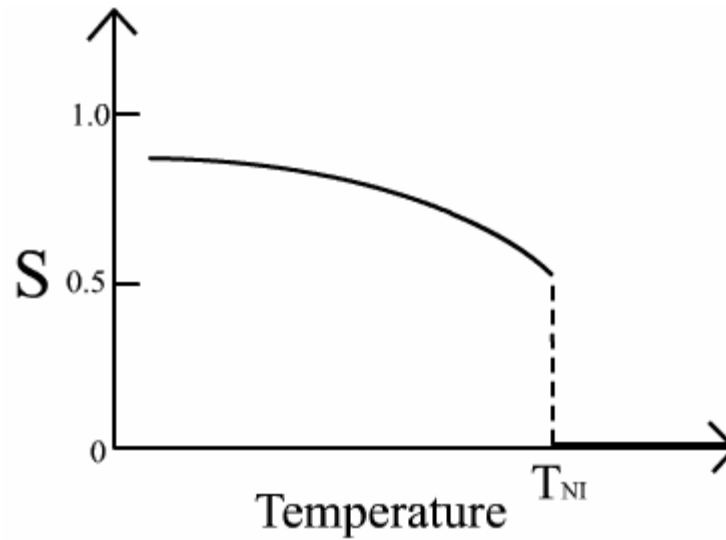


Figure 2: The general form of temperature-dependent order parameter of a LC.

We define the liquid crystal director as the average pointing direction of the liquid crystal molecules. This leads to a condition known as anisotropy, such as optical, dielectric, and elastic anisotropies. Optical anisotropy means that the refractive index of a material depends on the orientation where they are measured. An aligned liquid crystal has  $n_e$  (extraordinary ray) along the long optic axis and  $n_o$  (ordinary ray) along the short optic axis. This anisotropic nature of liquid crystals is a unique optical property, which can apply to many engineering applications.

### 2.2.2 Liquid crystal phases

The liquid crystal state is a distinct phase of matter observed between the crystalline (solid) and isotropic (liquid) states. There are many types of liquid crystal

states, depending upon the molecular arrangement in the material. This section briefly introduces the phase behaviors of liquid crystal materials.

### (1) Nematic Phase

The nematic liquid crystal phase is characterized by molecules that have no positional order but tend to point in the same direction (along the director). In Fig.3, the LC molecules, on average, point vertically with no particular order.

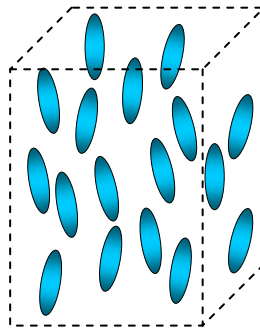


Figure 3: Nematic Liquid crystal phase illustration

A special class of nematic liquid crystals is called chiral nematic. Chiral nematic liquid crystals are similar to nematic liquid crystals except that the molecules tend to align in a helical structure with the helical axis perpendicular to the director. The term chiral nematic is used interchangeably with cholesteric. Refer to the section on cholesteric liquid crystals for more information about this mesophase.

### (2) Smectic Phases

Smectic phase is another class of liquid crystals. Molecules in this phase have larger degree of order than the nematic liquid crystal. The molecules tend to align themselves in layers or planes in the smectic state.

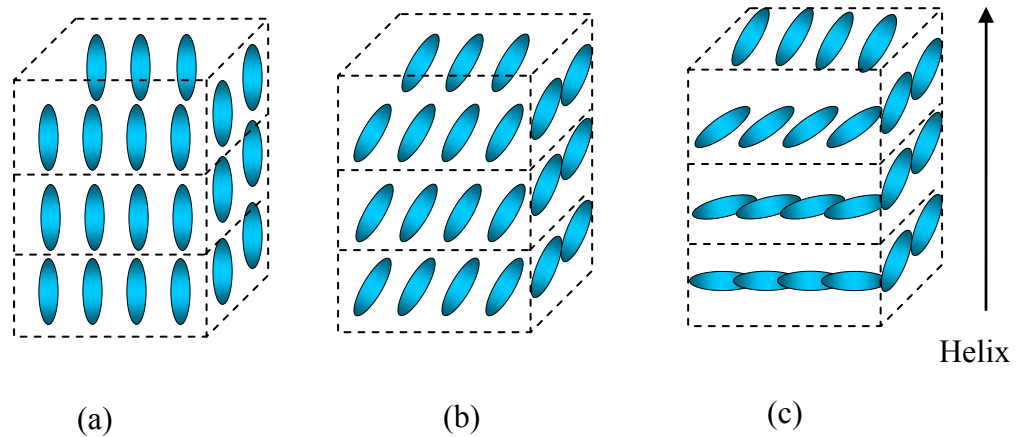


Figure 4: Smectic liquid crystal phase illustration (a) smectic A, (b) smectic C, and (c) smectic C\*

Figure 4 shows three kinds of smectic liquid crystals. The first one is smectic A in Figure 4(a). In the smectic-A phase, the director is perpendicular to the smectic plane, and there is no particular positional order in the layer. Figure 4(b) shows the smectic-C phase, molecules are arranged as in the smectic-A phase, but the director is at a constant tilt angle measured normally to the smectic plane. Figure 4(c) shows the smectic-C\*. Compared with the smectic-C, the LC directors in the smectic-C\* make a tilt angle with different smectic layers. The tilted angle of each layer rotates along a helix. The director of the smectic-C\* phase is not parallel or perpendicular to the layers, and it rotates from one layer to the adjacent one.

### (3) Cholesteric Phases

The cholesteric liquid crystal phase is composed of nematic molecules which contains a chiral center. The chiral center produces molecular forces that make alignment between directors at a small angle to adjacent one. This structure can be visualized as a

stack of two-dimensional (2-D) layers with the director in each layer twisted with respect to each other.

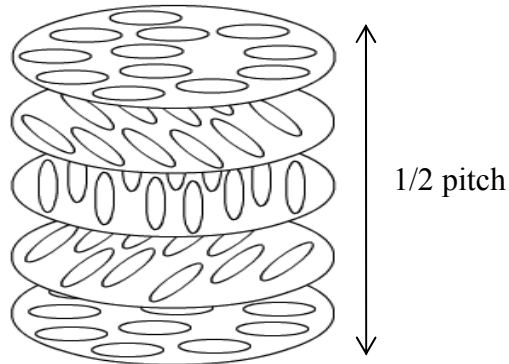


Figure 5: Schematic illustration of cholesteric liquid crystals

Figure 5 shows a schematic illustration of cholesteric liquid crystals. An important characteristic of the cholesteric phase is the helical pitch. The pitch is defined as the distance it takes for the director to rotate  $360^\circ$  as shown in the Figure 5. Figure 5 shows only  $180^\circ$  rotations, i.e., only half a pitch. The chiral nematic phase has ability to selectively reflect light of wavelengths equal to the pitch length. Therefore, the structure of cholesteric LCs reflects the incident light at wavelengths centered at  $\lambda = \langle n \rangle \cdot P$  in the visible spectrum. The Bragg reflection is also temperature dependent. There are so many applications of this function, such as thermometer film which can detect flaws in circuit board connections, condition of batteries and the presence of radiation.

The wavelength of the reflected light can also be controlled by adjusting the chemical composition, since cholesterics can either consist of exclusively chiral molecules or of nematic molecules with a chiral dopant dispersed throughout. In the latter case, the pitch can be tuned by adjusting the chiral dopant concentration.

### 2.2.3 Electric and magnetic field effects

Liquid crystals are widely used in a variety of applications because both electric and magnetic fields can be used to induce the changes of the molecular orientations. Figure 6 shows the ability of the LC director to align along an external field. Permanent electric dipoles result when one end of a molecule has a net positive charge while the other end has a net negative charge. In Figure 6, the black arrows represent the electric field direction. When an electric field is applied, the polar molecules tend to orient themselves along the direction of the red arrows (electric force on the molecule).

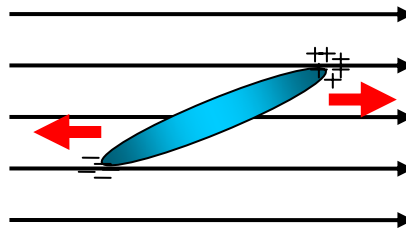


Figure 6: The electric field effect on liquid crystal molecule

The effects of magnetic fields on liquid crystal directors are similar to electric fields. When a magnetic field is applied, the LC directors will align with or against the field, depending on whether the LC is diamagnetic or paramagnetic.

### 2.2.4 Freedericksz transition

The Freedericksz transition is fundamental to many liquid crystal devices because the director reorientation can be easily manipulated by applying a field. The dynamic response of LC directors is governed by the surface anchoring, elastic torque, electric

field-induced torque, and viscous torque of the liquid crystal devices. For example, let us assume that the liquid crystal molecules are aligned parallel to the substrate surface and an electric field is applied in the perpendicular direction. If the applied voltage is below the Freedericksz transition threshold, the LC directors would not be reoriented. However, when the applied voltage exceeds a threshold, the LC deformation would occur. This deformation is called “Freedericksz transition” as it changes from an aligned to a deformed state.

### **2.2.5 Surface preparations**

Without surface treatment or an external field, the LC directors would be randomly distributed. However, it is possible to align the LC director to a specific direction by coating an alignment layer onto the glass substrates. For instance, liquid crystal molecules would align along the rubbing direction when a thin polyimide layer is coated on a glass substrate and rubbed in a single direction. Moreover, the LC layer would exhibit a pretilt angle which is essential for guiding the relaxation direction after the electric field is removed.

### **2.2.6 Liquid crystal deformation models**

There are three principal director deformations in nematic liquid crystals, which are twist, splay, and bend. The elastic energy equation is called the Oseen-Frank equation. This equation has three contributions which can be regarded as deformations of the

ordering due to twist, bend, and splay. General deformations are a mixture of these three types. Figure 7 shows these three LC deformations.

Splay: 
$$F_1 = \frac{1}{2} K_{11} (\nabla \cdot \hat{n})^2 \quad (2)$$

Twist: 
$$F_2 = \frac{1}{2} K_{22} (\hat{n} \cdot \nabla \times \hat{n})^2 \quad (3)$$

Bend: 
$$F_3 = \frac{1}{2} K_{33} (\hat{n} \times (\nabla \times \hat{n}))^2 \quad (4)$$

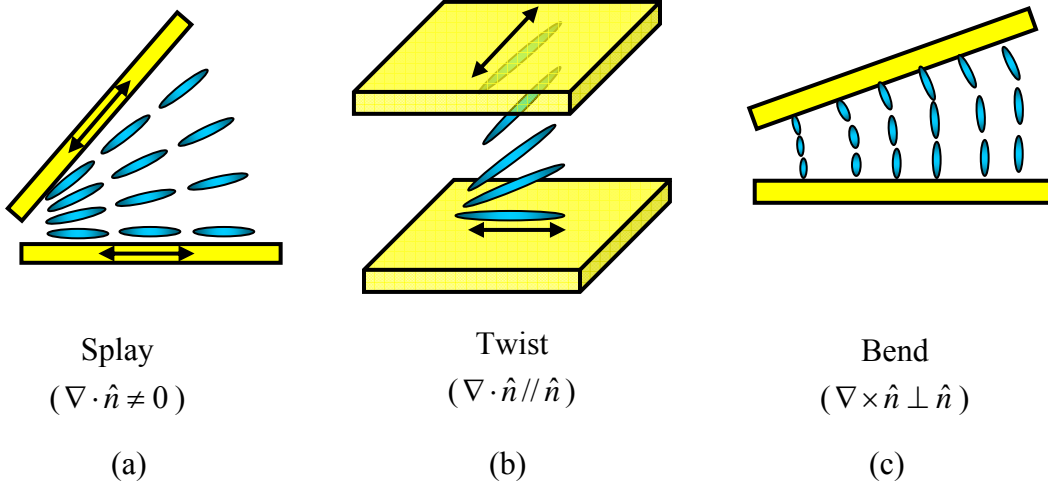


Figure 7: Three LC deformation models (a) splay, (b) twist, and (c) bend

The elastic constants of splay, twist and bend represent as  $K_{11}$ ,  $K_{22}$ , and  $K_{33}$ , respectively. The order of magnitude of these three elastic constants is around  $10^{-11} \sim 10^{-12}$  N in MKS units. Usually,  $K_{22}$  has the smallest value and  $K_{33}$  has the largest value.  $K_{11}$  and  $K_{33}$  have twice the value than  $K_{22}$ . For instance, the elastic constants  $K_{11}$ ,  $K_{22}$ , and  $K_{33}$  of the MBBA are  $5.8 \times 10^{-12}$ ,  $3.4 \times 10^{-12}$ , and  $7.0 \times 10^{-12}$  N, respectively.

## 2.3 Optics of liquid crystals

### 2.3.1 Light and polarization

This section will give a brief introduction of some basic concepts of light and polarization. They are important for the optical behavior of liquid crystals. As we know, light can be represented as a transverse electromagnetic wave, which contains the electric and magnetic fields perpendicular to each other. Figure 8 shows the electric field in the xy plane, the magnetic field in the xz plane and the propagation of the wave in the x direction. The right most shows a track of the electric field propagation. In general, we only deal with the electric field because the behavior of magnetic field component is almost the same.

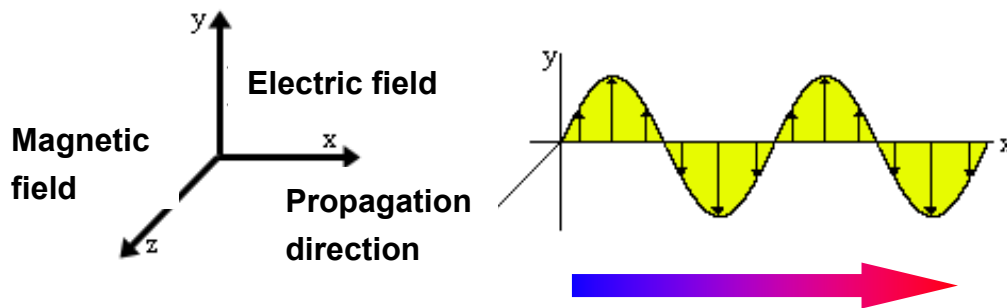


Figure 8: Illustration of the transverse electromagnetic wave

White light consists of waves that oscillate at all possible angles in y-z plane. Linearly polarized light is defined as the wave only fluctuates in one specific plane. A polarizer is a plate that allows only light with a specific angle to pass through. The axis



with this specific angle is called “transmittance axis”. Figure 9 shows the crossed and parallel polarizer configurations. If the transmittance axes are set at 90 degrees (crossed), the polarized light from the first is absorbed by the second polarizer as Figure 9(a) shows. However, if two polarizers (transmittance axes) are parallel, the light can pass through the analyzer as Figure 9(b) shows. The light transmittance decreases as the analyzer’s transmission axis rotates from 0 to 90 degrees.

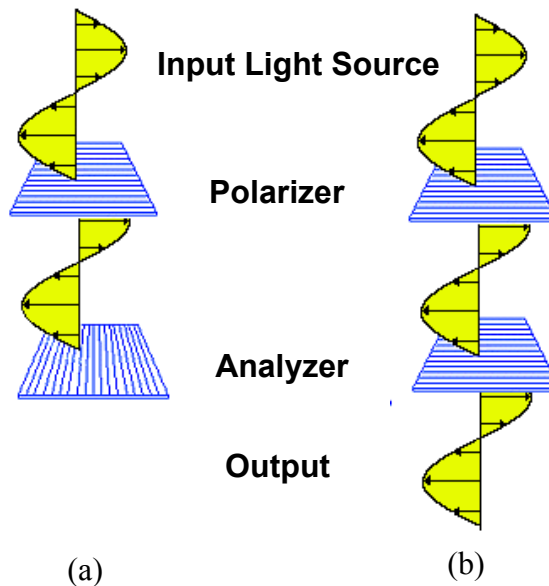


Figure 9: (a) Cross polarizer pair (b) Parallel polarizer pair

A linear polarization can be decomposed into two basic linearly polarized lights, one polarized in the YZ plane and the other in the XY plane. If they are in phase, the waves reach their maximum and minimum points at the same time, that leads to a linearly polarized at  $45^\circ$ . Figure 10(a) shows the  $45^\circ$  linearly polarized light. By the same way, if the two waves are  $180^\circ$  out of phase, the result is linearly polarized at  $135^\circ$ . Figure 10(b) shows the  $135^\circ$  linearly polarized light. If the two waves are 90 degrees out of phase, one is at an extremum and the other is at zero, which results in circularly polarized light.

Figure 10(c) shows the circularly polarized light. In fact, the general case is an elliptical polarization, which has phase difference at an arbitrary angle. The electric field traces look like an ellipse.

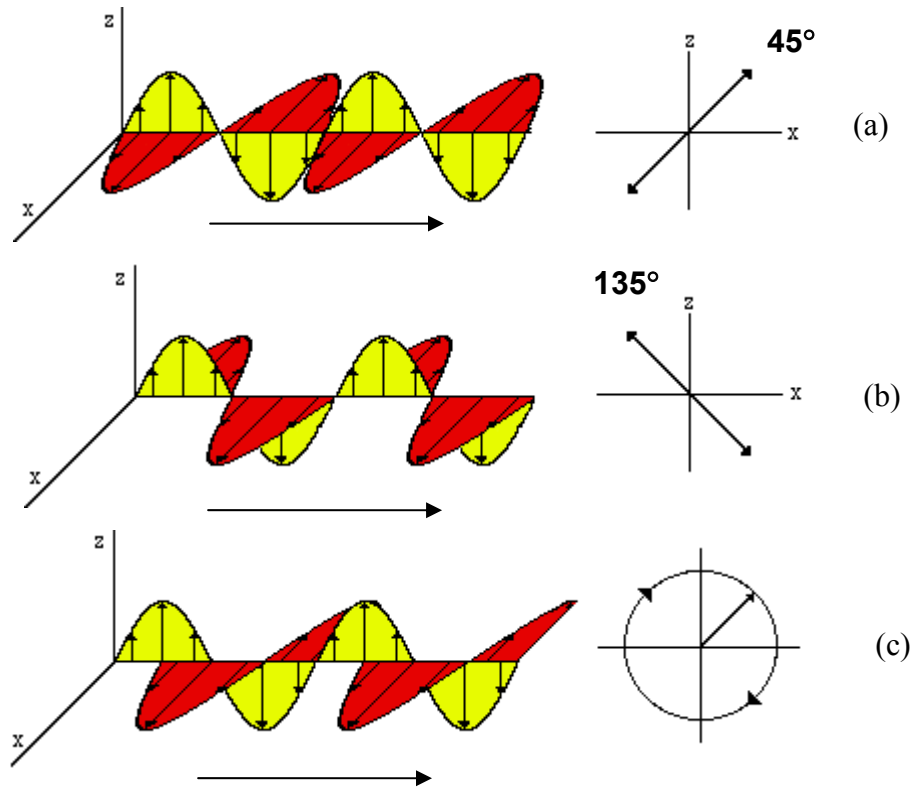


Figure 10: (a)  $45^\circ$  linearly polarized light, (b)  $135^\circ$  linearly polarized light, and (c) circularly polarized light.

### 2.3.2 Birefringence of liquid crystals

The previous section introduces the concepts of polarized light and polarizers. This section will describe the optical properties of liquid crystals.

Due to their anisotropic nature, liquid crystals are found to be birefringent. In other words, they have two indices of refraction in different directions. The light polarized parallel to the director has a different refraction index than the light polarized perpendicular to the director. In Figure 11, the red lines represent the LC directors and the arrows show the direction of the polarized light. From Figure 11(a), the polarized light which is parallel to the LC director has the refractive index  $n_e$  as it passes through the sample. However, for Figure 11(c), the polarized light which is perpendicular to the director has different refractive index  $n_o$  as it passes through the sample. Therefore, the polarized light with  $45^\circ$  to the director will have refractive index  $n_{eff}$  whose value is between  $n_o$  and  $n_e$ .

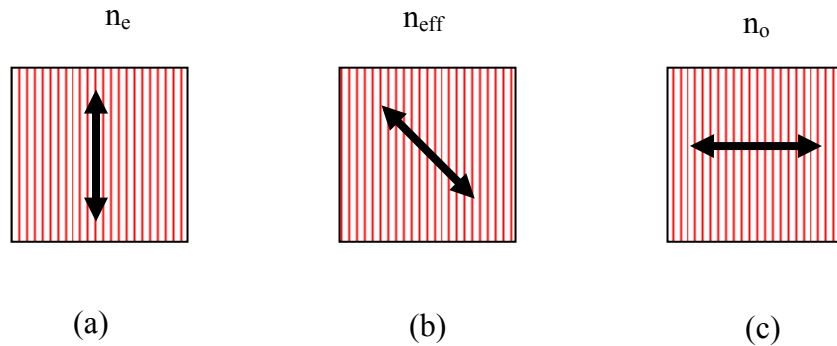


Figure 11: (a) Parallel, (b)  $45^\circ$ , and (c) Perpendicular to the LC directors

When light enters a nematic liquid crystal sample, the process is modeled in terms of the light being broken up into the fast (called the ordinary ray) and slow (called the extraordinary ray) components. Since the two components travel at different directions, the waves encounter different refractive indices and travel at different speed. As they exit the LC sample, their phase retardation is different. As a result, the polarization state will change according to the phase retardation accumulated in the LC layer..

The birefringence of a material is defined as  $\Delta n = n_e - n_o$ . When  $\Delta n > 0$ , the LC material is called positive birefringence while  $\Delta n < 0$  is called negative birefringence. About 99.9% of the LC compounds discovered have a positive birefringence. Typically,  $n_o$  is approximately 1.5 and  $\Delta n$  could vary from 0.05 to 0.5, strongly depends on the molecular conjugation.

Phase retardation of a LC cell is defined as  $\delta = 2\pi d \Delta n / \lambda$ , where  $d$  is the cell gap and  $\lambda$  is the wavelength. The phase retardation accumulates as long as the light propagates in the birefringent material. When the applied voltage exceeds the Freedericksz threshold, the LC directors are tilted. Under this circumstance, the  $\Delta n$  becomes an effective birefringence. Its value depends on the applied voltage. By controlling the voltage, continuous phase retardation change can be obtained. The output polarization state can then be manipulated.

### 2.3.3 EO properties of liquid crystal

As we mentioned previously, if we applied the voltage to the liquid crystal, the orientation of the liquid crystal molecule will be controlled by the electric field. While the orientation of the liquid crystal changes, the phase retardation of the input light will also change. Therefore, the optical properties can be manipulated by the electric field. The equations below show the transmittance of a homogenous cell as a function of the applied voltage  $V$  between crossed and parallel polarizers:

$$\text{Crossed :} \quad T_{\perp} = \sin^2\left(\frac{\pi \cdot \Delta n(V) \cdot d}{\lambda}\right) \quad (5)$$

$$\text{Parallel:} \quad T_{\parallel} = \cos^2\left(\frac{\pi \cdot \Delta n(V) \cdot d}{\lambda}\right) \quad (6)$$

Figure 12 shows an example of the voltage dependent transmittance curve for a homogenous cell. The transmittance curves of the crossed polarizers and the parallel polarizers are complementary. In theory, the transmittance curve of the crossed polarizers should decrease to zero in a high voltage regime. This is because all the liquid crystal directors are reoriented perpendicular to the substrates, except the boundary layers. Hence, the incoming light passes through the LC sample without experiencing any phase retardation and is blocked by the crossed polarizers.

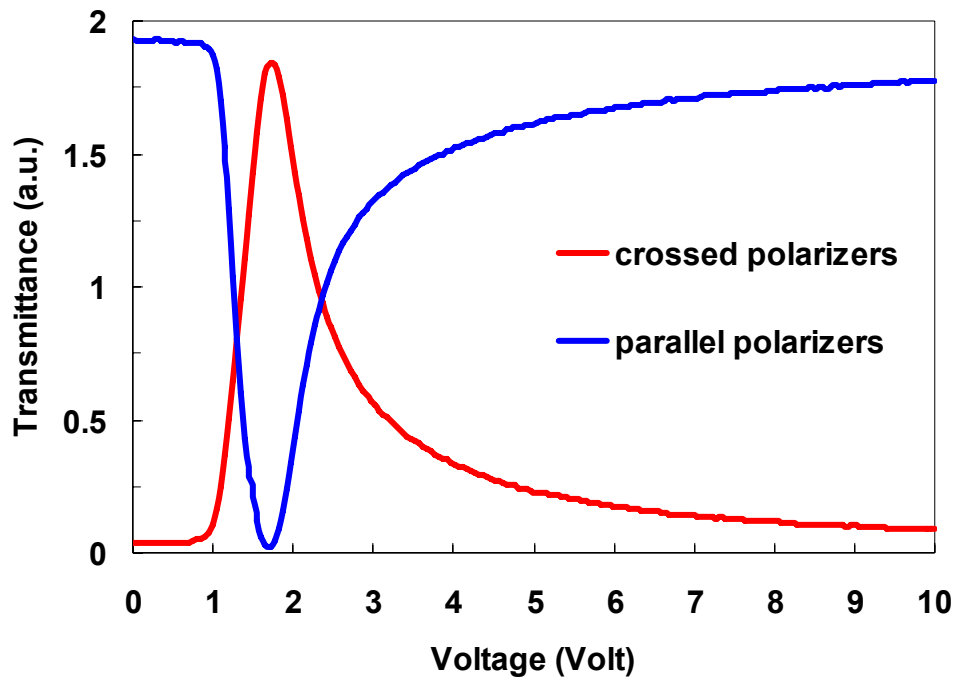


Figure 12: The voltage dependent transmittance of a homogeneous cell between crossed and parallel polarizers.

## **2.4 Polymer network liquid crystal (PNLC)**

The polymer network liquid crystal (PNLC) cell consists of liquid crystal and polymer network. Compared to the polymer-dispersed liquid crystal (PDLC), PNLC has a much higher LC concentration. In general, the monomer concentration of a PNLC is less than 15 %. The PNLC exhibits a very strong light scattering in the visible spectral range when the monomer concentration is low ( $< 2$  wt%).<sup>27,28</sup> Although the polymer concentration is low, the response time of the LC cell can be improved by the polymer network restoring force. For the larger concentration of PNLC ( $\sim 3$ -8 wt %), the polymer-stabilized LC (PSLC) is formed.<sup>3,29</sup> These PSLC cells have anisotropic light scattering properties and have been investigated for telecom applications.<sup>55,59</sup>

Polymer network liquid crystals are made from mixtures of liquid crystals and monomers. The monomer consists of 1-5 wt% photo-initiator. For the low concentration of the monomer, the monomer can be directly dissolved in the liquid crystal. Before UV curing process, the mixture of the monomer and the liquid crystal is in a liquid crystal phase. During the curing process, the monomers start to polymerize along the liquid crystal alignment direction. The anisotropic polymer networks mimic the structure of the liquid crystal during the polymerization.<sup>31,32</sup> The photo-initiated polymerization is fast and is a popular way to fabricate the PNLC cell. For fast-response LC modulator, we use a homogeneous PNLC with  $\sim 10\%$  polymer concentration.

## **2.5 Variable optical attenuator (VOA)**

An attenuator, by definition, is a device which precisely reduces an optical signal from point-to-point. The loss can be achieved through various technologies such as

absorption, scattering, interference (thin film) filter, or air-gap. The most common use of the optical attenuator, whether fixed or variable, is in optical networks where erbium-doped fiber-optic amplifiers are being used. An attenuator is used for adjusting the optical signal levels thereby increasing the network flexibility and providing management of optical power.

Liquid crystal-based variable optical attenuator is a good candidate for fiberoptic communication because it has the good properties, such as high contrast ratio, good gray scales, and low power consumption. Table 1 shows the specifications of the LC-based VOA in present market.

Table 1: Specifications of the VOA (from Lightwaves2020 Company  
<http://www.lightwaves2020.com>)

Specifications							
Parameters		Unit	Normal-on		Normal-off		
			Grade P	Grade A	Grade P	Grade A	
Operating Wavelength Range	-	nm	C-band , L-band or C- & L-band				
Attenuation Range	Min	dB	20 , 30 or 40		21 or 33		
Insertion Loss	Max	dB	1.0	1.2	1.1	1.3	
Polarization Dependent Loss	@10dB	Max	dB	0.15	0.2	0.25	0.3
	@20dB	Max	dB	0.25	0.4	0.35	0.5
Wavelength Dependent Loss	@10dB	Max	dB	0.4 @C-band or L-band			
Polarization Mode Dispersion	Max	ps	0.1				
Chromatic Dispersion	Max	ps/nm	0.2				
Return Loss	Min	dB	45				
Attenuation Resolution	Min	dB/mV	Continuous				
Maximum Optical Power	Min.	mW	300				
Response Rise Time (attenuation increase)	Max	ms	5				
Response Fall Time (attenuation decrease)	Max	ms	35 (-5°C ~ 23°C), 15 (23°C ~ 70°C)				
Driving Voltage (without driver)	-	V	0 ~ 30 Peak to Peak, 10 KHz Square Wave				
Driving Voltage (with driver )	-	V	0 ~ 5 DC				
Operating Temperature	-	°C	-5 ~ 70				
Storage Temperature	-	°C	-40 ~ 85				
Fiber Pigtail	-	-	SMF-28, 250µm bare fiber or 900µm loose tube, 1.0±0.1m				
Dimensions	-	mm	φ7.2 × 23.5 without driver,				
			36.3 × 12.7 × 11.5 with driver				

## CHAPTER 3: DUAL-FREQUENCY LIQUID CRYSTAL PHASE MODULATORS

### 3.1 Theory of dual-frequency liquid crystal

Fast response time is a critical issue for the IR scene projector. The goal is to achieve  $<10$  ms at  $\lambda=10.6$   $\mu\text{m}$ . We demonstrated a fast-response LC modulator at  $\lambda=1.55$   $\mu\text{m}$  using a dual-frequency liquid crystal (DFLC) with overdrive and undershoot voltages. The DF LC mixture formulated in our labs exhibits a crossover frequency in the 5-10 kHz range. Figure 13 shows the important properties of the dual-frequency liquid crystal. It shows the dielectric anisotropic constant as the function of the frequency. When the frequency is lower than the crossover frequency, the DF LC has a positive dielectric anisotropy ( $\Delta\epsilon>0$ ). However, above crossover frequency the dielectric anisotropy turns to negative. By using this unique property of dielectric anisotropy change, we could drive the LC medium in both rise and decay periods by a low- and a high-frequency electric field, respectively. Both fast rise and decay times can be achieved.



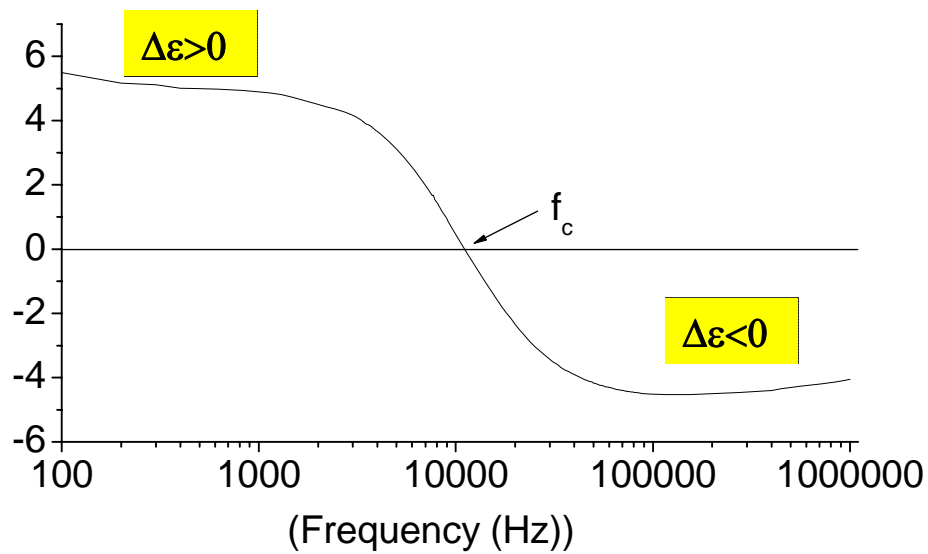


Figure 13: Dielectric anisotropy  $\Delta\epsilon$  ( $\epsilon_{\parallel} - \epsilon_{\perp}$ ) of LCs changes sign from positive (+) to negative (-) while increasing the frequency of applied electric field.

In order to obtain a high contrast ratio, we align the DFLC in a homeotropic cell, also known as vertical alignment (VA). In a VA cell, the LC molecules are aligned perpendicular to the cell substrates. In the crossed-polarizer configuration, the incident light sees no phase retardation. As a result, the outgoing light is absorbed by the crossed analyzer. If the pretilt angle is small ( $< 2^\circ$ ), the contrast ratio is basically limited by the crossed polarizers.

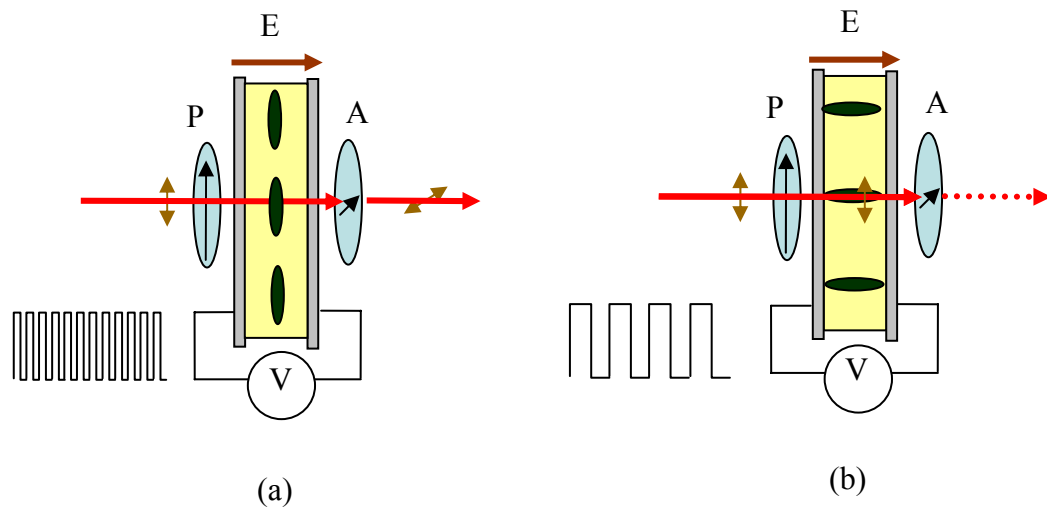


Figure 14: The operating principles of a VA cell containing DF-LC. (a) On state: High frequency driving  $\sim 30$  kHz, (b) Off state: low frequency driving  $\sim 1$  kHz

Figure 14(a) and (b) show the operating principles of the DF-LC-VA cell. In the beginning, the LC directors are aligned perpendicular to the substrates. To reorient the LC directors, a high-frequency electric field is applied because the LC has a negative  $\Delta\epsilon$  in the high frequency region. In the decay period, a low-frequency electric field is applied to assist the LC relaxation. Thus, both fast rise and decay times can be obtained.

To further shorten the response time, we can apply the overdrive and undershoot voltages. Figure 15 shows the overdrive and undershoot voltage methods. The figure shows the applied voltage and corresponding optical response. Blue solid line represents the normal driving method. The LC response is fairly slow because the driving voltage is low. If we try to apply 2~3 periods of high voltage waveform like the red dish lines, the LC response time becomes faster due to the larger torque applied to the LC directors. As the LC response reaches the desired transmittance level, we can reduce the driving

voltage in order to hold the transmittance. Based on the LC response curve, the overdrive and undershoot methods significantly improve the response time.

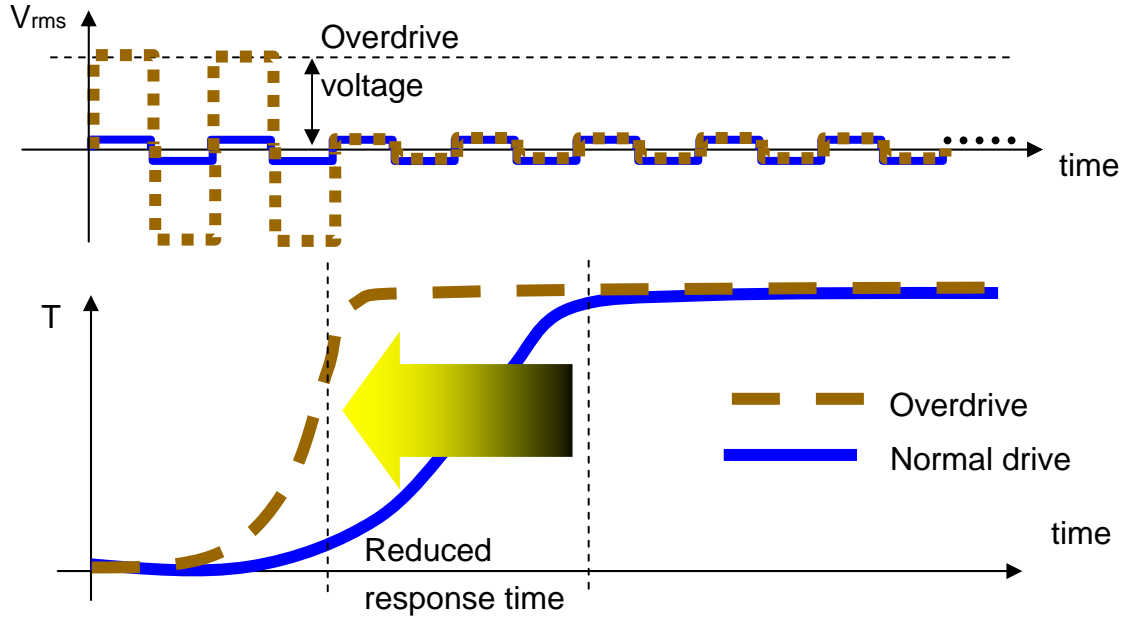


Figure 15: Overdrive and undershoot voltage methods

### **3.2 Dual-frequency liquid crystal phase modulators for long IR applications**

#### **3.2.1 Sample fabrication**

To evaluate the device performance, we filled a 7  $\mu\text{m}$  VA cell with our own DF-LC-25 mixture. The physical properties of DF-LC-25 mixture are listed as follows: birefringence  $\Delta n=0.24$  at  $\lambda=1.55 \mu\text{m}$ , dielectric anisotropy  $\Delta\epsilon=+5$  at  $f=1 \text{ kHz}$  and  $\Delta\epsilon=-4$  at  $f=30 \text{ kHz}$ , and the crossover frequency is  $f_c=6 \text{ kHz}$  at  $T=22^\circ\text{C}$ .

### 3.2.2 Experimental results and discussions

Figure 16 demonstrates the turn-on and -off times of a transmissive DF-LC VA cell with overdrive and undershoot voltages. The top trace shows the applied signal to the DF-LC VA cell and the bottom trace is the corresponding optical response. To obtain fast response time, we applied an overdrive waveform ( $f=30\text{ kHz}$ ,  $V=41.5\text{ V}_{\text{rms}}$ ,  $0.4\text{ ms}$  duration) to turn on the device rapidly. Once the LC modulator reaches a  $\pi$  phase change, i.e., maximum transmittance, we applied a holding voltage with  $f=30\text{ kHz}$ ,  $V=12\text{ V}_{\text{rms}}$ , and  $2.5\text{ ms}$  duration. In the turning-off stage, we applied a low-frequency high voltage waveform ( $f=1\text{ kHz}$ ,  $V=41.5\text{ V}_{\text{rms}}$ ) for  $0.4\text{ ms}$ . A good dark state is achieved, as shown in Figure 16. Since the LC decay process is also assisted by a low frequency undershoot voltage, the response time is much faster than the conventional LC modulator.

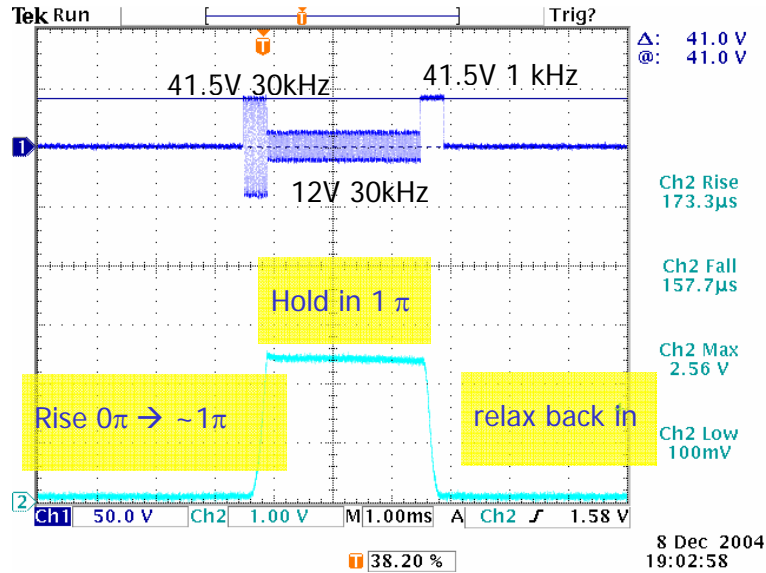


Figure 16: Turn-on and -off time of the DF-LC-VA cell with overdrive and undershoot voltages.  $\lambda=1.55\text{ }\mu\text{m}$  and  $T=22\text{ }^\circ\text{C}$ .

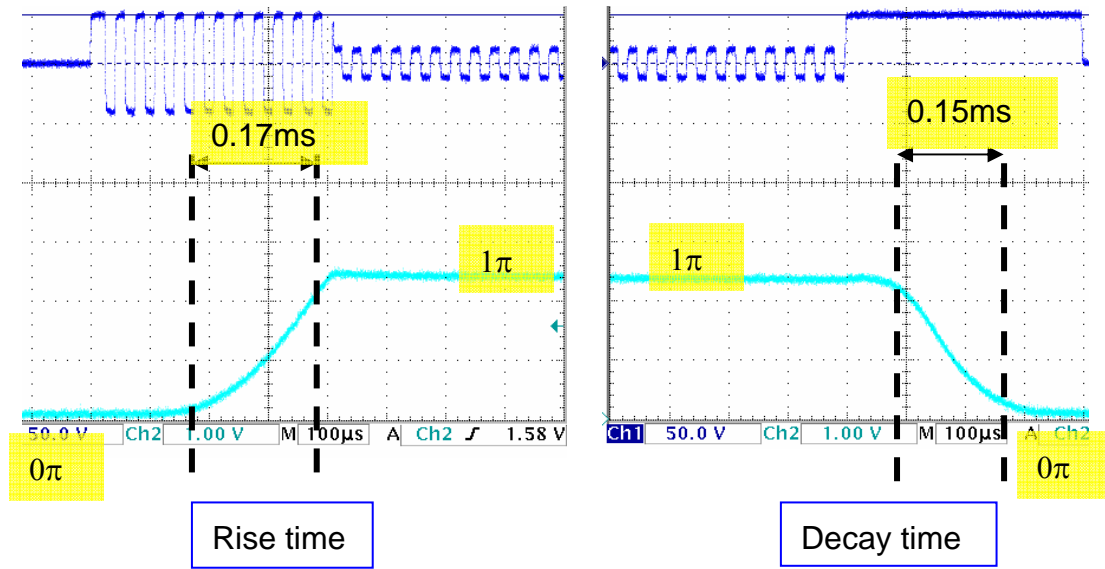


Figure 17: The LC response curves at  $\lambda=1.55 \mu\text{m}$ : (a) rise time and (b) decay time.

Figure 17 shows the response time of the LC modulator. The rise and decay time are measured from 10% to 90% and 90% to 10% transmittance. The rise and decay time is 0.17 ms and 0.15 ms, respectively.

Figure 18 shows the reflective long IR ( $\lambda=10.6 \mu\text{m}$ ) projector setup. Our target is to achieve  $1 \pi$  phase in this reflective projector. In the long infrared ( $\lambda=10.6 \mu\text{m}$ ) region, to achieve  $1 \pi$  phase retardation using a homogeneous cell the required  $d\Delta n$  is  $\lambda/2$ , or  $5.6 \mu\text{m}$ . In order to obtain a high speed LC modulator at  $\lambda=10.6 \mu\text{m}$ , we calculate the phase change based on our  $1.55 \mu\text{m}$  result shown in Figure 19. The results show 2 ms response time with  $0.45 \pi$  phase change in a reflective device.

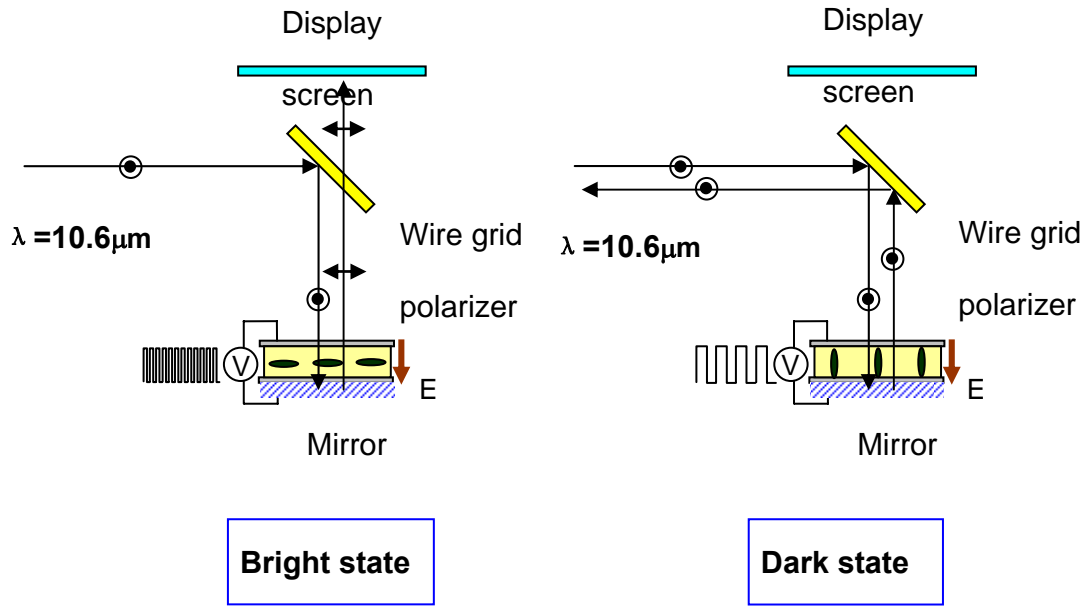


Figure 18: Reflective IR projector setup

Figure 19 demonstrates the turn-on and -off times of the transmissive DF-LC cell with overdrive and undershoot voltages at  $\lambda=1.55\ \mu\text{m}$ . During the rise period, a high frequency voltage ( $f=10\ \text{kHz}$ ,  $V=40\ \text{V}_{\text{rms}}$ , 1.2 ms duration) was applied. The LC directors were aligned in the direction perpendicular to the electric field. In order to hold the LC directors in the ON period, a high frequency holding voltage ( $f=10\ \text{kHz}$ ,  $V=20\ \text{V}_{\text{rms}}$ ) was applied to the cell. During the relaxation process, a low frequency voltage ( $f=100\ \text{Hz}$ ,  $V=40\ \text{V}_{\text{rms}}$ ) is applied to accelerate the LC relaxation back to its original homeotropic state. Therefore, a  $1.5\pi$  phase change at  $1.55\ \mu\text{m}$  within 1 ms (rise and decay time) was achieved.

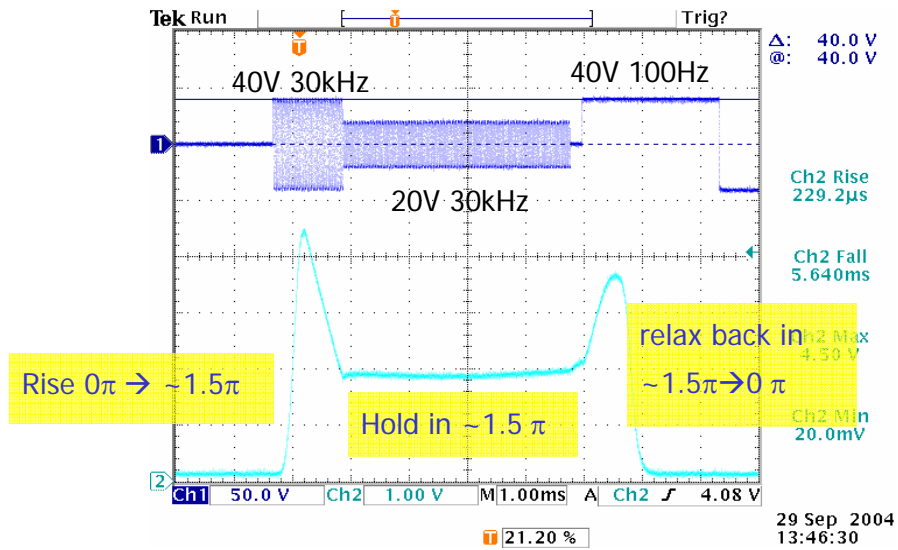
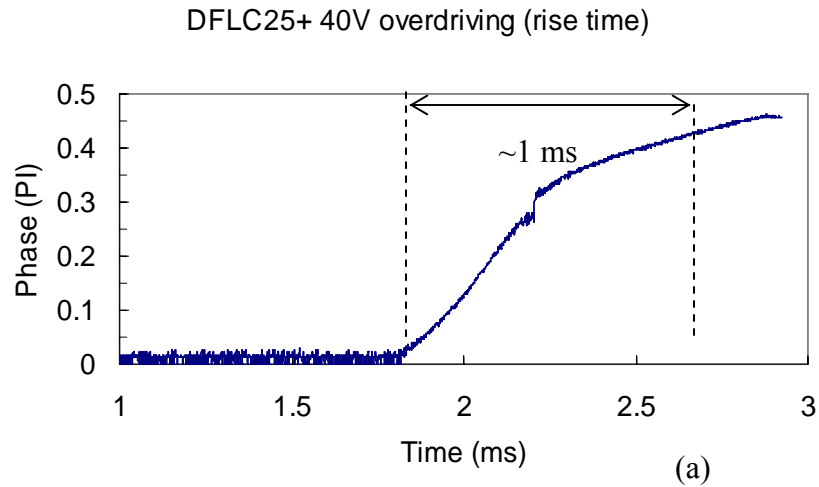


Figure 19: Turn-on and turn-off time of the DFCL cell with overdrive and undershoot voltages.  $\lambda=1.55 \mu\text{m}$ .



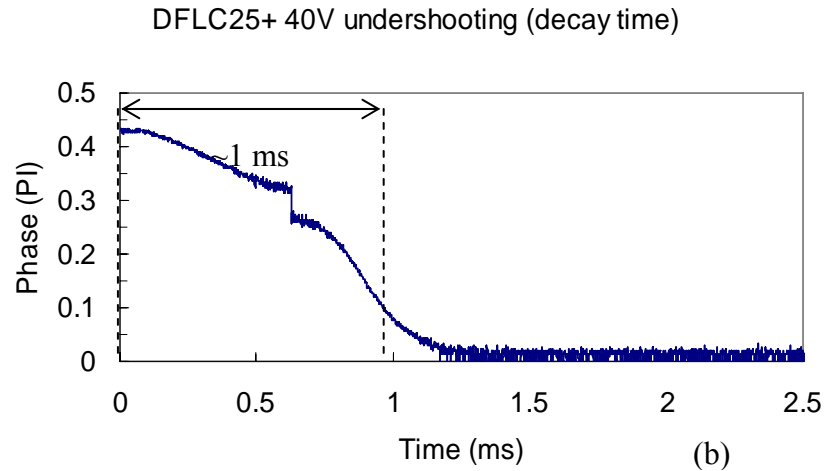


Figure 20: The estimated LC phase response curve at  $10.6 \mu\text{m}$  (a) rise time, and (b) decay time.

Based on the  $7 \mu\text{m}$  DFLC cell results, we could estimate the response time of a reflective device operating at  $\lambda=10.6 \mu\text{m}$ . In the near and long IR region, the LC birefringence remains basically unchanged if we ignore the local resonance effect. Thus, the  $7\text{-}\mu\text{m}$  DFLC cell has  $\delta\sim 0.6\pi$  for the reflective mode operation. Figure 20(a) and (b) show the LC phase response times. The rise ( $\delta=0\rightarrow 0.45\pi$ ) and decay ( $\delta=0.45\pi\rightarrow 0$ ) times are 1 ms and 1 ms, respectively.

From Figure 20, the phase retardation of the  $7 \mu\text{m}$  DFLC cell is still not high enough for  $10.6 \mu\text{m}$  application. Therefore, a larger cell gap or a higher birefringence LC material is needed. To obtain  $1 \pi$  phase change, the cell gap should be  $\sim 15 \mu\text{m}$ .



### **3.3 Dual-frequency addressed variable optical attenuator**

#### **3.3.1 Introduction**

Liquid crystal (LC)-based variable optical attenuators (VOAs) have been developed for fiber-optic communications at  $\lambda=1.55 \mu\text{m}$  because of their low cost, low loss, and low power consumption.<sup>34,35</sup> However, for most telecommunications applications, a fast response time and a large dynamic range ( $>30 \text{ dB}$ ) are required. Two types of LC-VOAs have been developed, nematic and ferroelectric.<sup>36</sup> The latter is capable of achieving a microsecond response time, but it is a bistable device. To obtain gray scales, a pulse width modulation method has to be implemented. However, it is difficult to apply this technique to telecommunications products due to rigorous stability and reliability requirements. There are two major technical challenges for ferroelectric LCs: an ultra-thin cell gap ( $d < 2 \mu\text{m}$ ) and a residual DC voltage effect. The thin-cell requirement lowers the manufacturing yield and the residual DC voltage causes gray-scale instability. On the other hand, nematic VOA is easy to fabricate and it has natural gray scales. The major disadvantage is a slow response time. To achieve a fast response time, a small cell gap,<sup>37</sup> a high-temperature effect,<sup>38,39</sup> dual-frequency LC materials,<sup>40,41,42</sup> a voltage effect,<sup>43,44</sup> and a polymer-network LC<sup>4</sup> were realized. A typical nematic LC-based VOA has a response time of approximately 5-15 ms, which is still slower than a mechanical shutter whose response time is approximately 1 ms. To outperform the mechanical shutter, the nematic VOA should have a submillisecond response time at room temperature while maintaining a wide dynamic range and low operating voltage ( $\leq 20 V_{\text{rms}}$ ).

In this study, we demonstrated a fast-response and wide-dynamic-range nematic VOA using a high-birefringence and low-viscosity dual-frequency LC mixture. To achieve a submillisecond response time at room temperature ( $T \sim 21^\circ\text{C}$ ), we used a low-frequency ( $f=1$  KHz) overdrive voltage to decrease rise time and a high-frequency ( $f=30$  KHz) undershoot voltage to accelerate the decay process. The measured dynamic range exceeds 40 dB at  $\lambda=1.55$   $\mu\text{m}$ .

### 3.3.2 Sample fabrication and experimental setup

Figure 21 shows a schematic of the LC-based VOA where two polarization beam displacers and a LC cell are sandwiched between two identical fiber collimators with an 80 mm working distance. The light from the input fiber is collimated by the first GRIN (gradient refractive index) lens collimator. When the light is incident to the first polarization beam displacer (PBD), a 10-mm-thick  $45^\circ$ -cut calcite crystal, it is separated into an ordinary beam and an extraordinary beam. A quartz half-wave plate (HWP) is laminated to the calcite PBD to rotate the polarization state of the top beam. Therefore, both beams have the same polarization before entering the LC cell. Here, we use a 3.7  $\mu\text{m}$  homogeneous cell with its rubbing direction oriented at  $45^\circ$  to the input light polarization. Its phase retardation ( $\delta = 2\pi d\Delta n / \lambda$ ) is approximately  $1.2 \pi$  at  $\lambda=1.55$   $\mu\text{m}$ . To ensure a high transmittance at  $V=0$ , an identical LC cell, i.e., with the same cell gap, LC material and alignment but with no voltage applied, was placed behind the master LC cell to act as a phase compensation cell. The rubbing direction of the compensation cell is orthogonal to that of the master cell so that the net phase retardation at  $V=0$  is zero. This

master compensation cell configuration exhibits an excellent wavelength tolerance.<sup>45</sup> Under such circumstances, the top and bottom beams are recombined by the second PBD and HWP and then coupled into the collecting fiber collimator, as shown in the upper part of Figure 21. This is the high-transmittance state of the VOA. To make the device compact, the compensation LC cell can be replaced with a polymeric film, which is used in display devices to increase the viewing angle.<sup>1</sup>

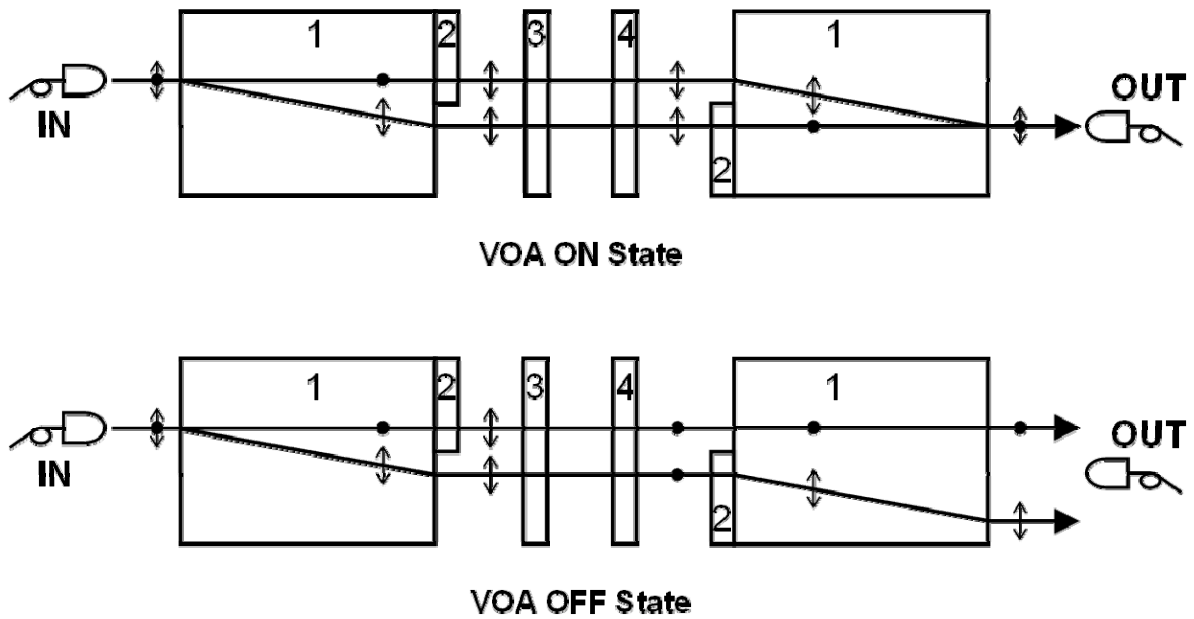


Figure 21: Schematic diagram of DFLC-based variable optical attenuator, where “1”, “2”, “3” and “4” represent polarization beam displacer, half-wave plate, master LC cell, and compensation cell, respectively.

When a proper voltage is applied to the master LC cell to make a  $\pi$  phase change, the incident beams could not retain their original polarizations. As a result, they are separated by the second beam displacer. No light is coupled into the collecting fiber collimator and the off-state results, as shown in Figure 21. By tuning the master cell voltage, different gray scales can be obtained. If the LC cell gaps are all uniform, then the

VOA should have no polarization-dependent loss (PDL) and no polarization mode dispersion (PMD). In our experiments, the beam displacers and the LC cell are tilted at a small angle to avoid back reflections (not illustrated in the diagram).

The VOA performance is mainly determined by the LC material employed. To achieve a fast response time, we decided to use a dual-frequency liquid crystal (DFLC). The key feature of a DFLC is that it exhibits a cross-over frequency ( $f_c$ ). In the  $f < f_c$  region, the dielectric anisotropy ( $\Delta\epsilon$ ) is positive, while in the  $f > f_c$  region the  $\Delta\epsilon$  becomes negative. In the low-frequency region, the electric-field-induced torque reorients the LC molecules along the field direction. This leads to the fast rise time. During the relaxation period, a high-frequency electric field is applied to the cell. Because the  $\Delta\epsilon$  is negative, the high-frequency electric field helps to accelerate the relaxation of the LC molecules to their original positions. As a result, a fast decay time is achieved.

Most of the commercially available DFLC mixtures have a low birefringence, high viscosity, and small  $|\Delta\epsilon|$  values.<sup>41</sup> Due to their low birefringence, a thick LC layer is required, particularly for the 1.55  $\mu\text{m}$  infrared wavelength. The thick LC layer leads to a slow response time and a high operating voltage. To overcome these drawbacks, we prepared a high-birefringence and low-viscosity DFLC mixture using 30% biphenyl esters and 70% lateral difluoro tolanes. The physical properties of our DFLC mixture at room temperature ( $T=21^\circ\text{C}$ ) are summarized as follows: cross-over frequency  $f_c \approx 4$  kHz;  $\Delta n = n_e - n_o = 0.25$  at  $\lambda = 1.55 \mu\text{m}$ ;  $\Delta\epsilon = 4.73$  at  $f = 1$  kHz; and  $\Delta\epsilon = -3.93$  at  $f = 30$  kHz.

For VOA demonstration, we used an Ando AQ4321D tunable laser operated at  $\lambda = 1.55 \mu\text{m}$  as the light source. The output fiber was connected to an Ando AQ8201-21 power monitor for measuring transmittance. A computer-controlled LabVIEW system was used for data recording and processing. The insertion loss (IL) of our VOA at  $V=0$  was measured to be approximately  $-2.0 \text{ dB}$  (without connector). The PDL remains less than  $0.1 \text{ dB}$  over the whole ITU (International Telecommunication Union) C-band ( $1.53 - 1.57 \mu\text{m}$ ) as expected. Although the measured IL is still not sufficiently low, the actual fiber-to-fiber coupling loss is only approximately  $0.8 \text{ dB}$  when taking into account the  $\sim 1.2 \text{ dB}$  propagation loss which is mainly contributed by the uncoated LC cells.

### 3.3.3 Experimental results

Figure 22 shows the VOA attenuation measured at different driving voltages. The VOA is addressed by square waves at  $f=1 \text{ kHz}$ . Because of the positive  $\Delta\epsilon$  in the low-frequency region, the LC molecules are reoriented along the electric-field direction as the voltage exceeds  $2.5 V_{\text{rms}}$  (threshold voltage). At  $V=6 V_{\text{rms}}$  which corresponds to a  $\pi$  phase change, an off state with  $-43 \text{ dB}$  attenuation is achieved. As shown in Figure 22, this off state is quite stable. Within  $\pm 0.3 V_{\text{rms}}$  voltage variation, the measured attenuation remains of over  $-30 \text{ dB}$ , which is important if this VOA is to be used as a light switch or wavelength blocker. As the applied voltage exceeds  $6 V_{\text{rms}}$ , the net phase change due to the orthogonal master and compensation cells is deviated from  $1\pi$  so that the optimal off state condition is no longer satisfied. As a result, the VOA attenuation gradually decreases.

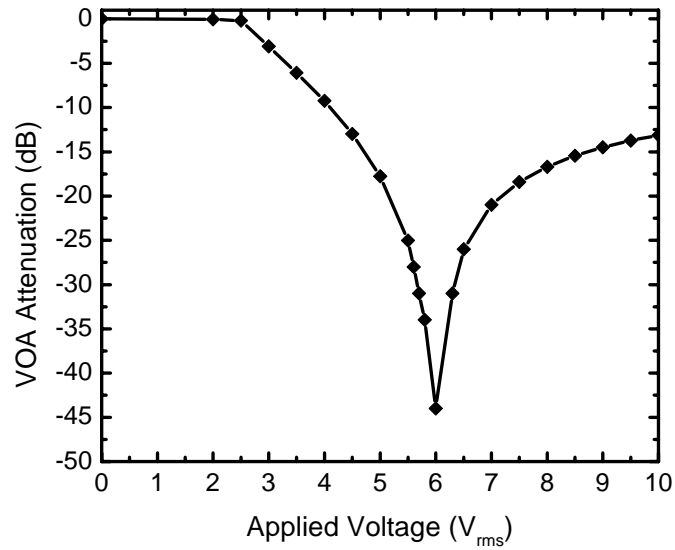


Figure 22: Measured VOA attenuation on dB scale as function of applied voltage. The VOA is addressed by a 1 kHz square-wave ac source.

To improve the VOA response time, we applied the overdrive and undershoot voltage waveforms during the low- and high-frequency periods, respectively, to drive the master cell while keeping the compensation cell uncharged. The low-frequency voltage was used to reorient the LC molecules and the high-frequency voltage was used to erase this reorientation. Results are compared with those using the conventional single-frequency driving method as shown in Figure 23. The solid lines in Figure 23(a) and (b) show the turn-off and turn-on times, when a  $6 V_{rms}$  single-frequency ( $f=1$  KHz) voltage is applied and removed from the cell, respectively. The 90-10% and 10-90% transmittance transition times are 11 ms and 35 ms, respectively. From Figure 23(a), the unbiased case has a delay time of  $\sim 4$  ms. To reduce the delay time, we applied a 1 KHz,  $2 V_{rms}$  biased voltage, which is somewhat lower than the threshold voltage ( $V_{th} \sim 2.5 V_{rms}$ ).

The turn-off time, the dashed line in Figure 23(a), is indeed reduced. However, the relaxation time (dashed lines) as depicted in Figure 23(b) was increased to ~60 ms.

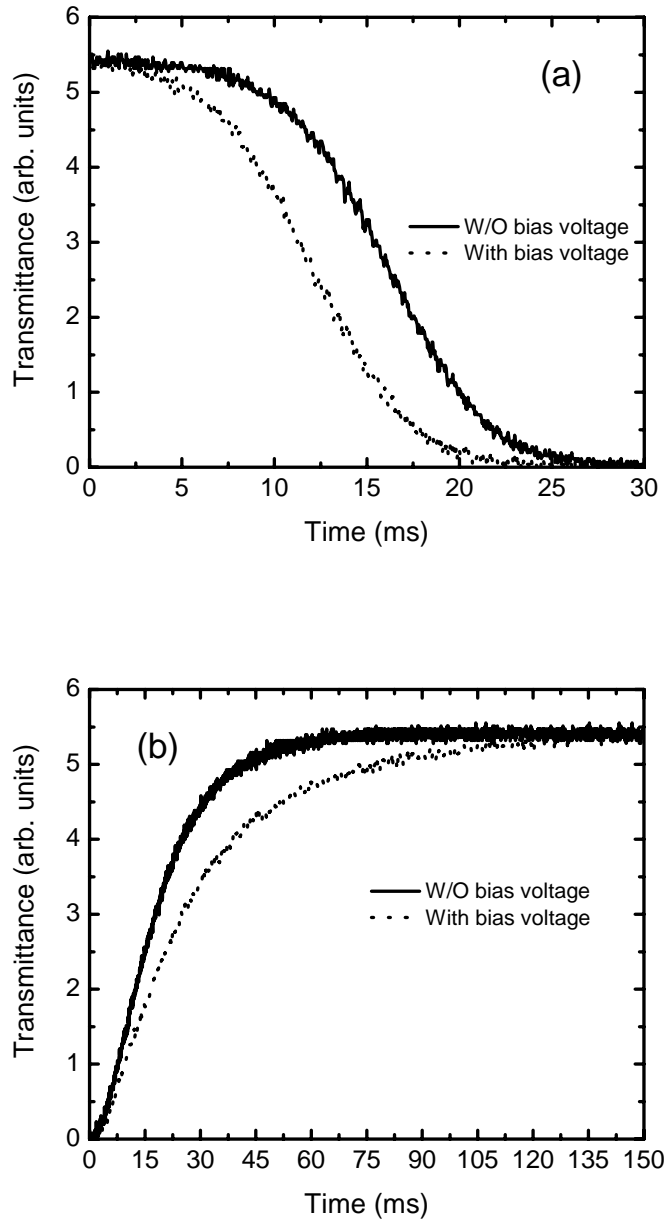


Figure 23: (a) Optical response curves of DFLC VOA when 1 kHz 6  $V_{\text{rms}}$  voltage is applied to turn VOA to off state. (b) Optical response curves that reflect LC directors' relaxation process when applied field is removed. The solid line and

dot line correspond to cases without and with a  $2 V_{\text{rms}}$ -bias voltage ( $f=1$  kHz), respectively.

Figure 24 shows the turn-on and turn-off times of the DFCLC cell with the overdrive and undershoot voltages applied during the rise and decay periods. The commercial LC-VOA is normally driven by a 20V ac voltage source. For a fair comparison, we also limited our overdriving voltage to  $20 V_{\text{rms}}$ . The  $20 V_{\text{rms}}$  low-frequency voltage burst was applied for 2 ms between the  $2 V_{\text{rms}}$  bias and  $6 V_{\text{rms}}$  holding voltages. The turn-on time (90-10%) was measured to be 0.73 ms. The overdrive voltage signals and the corresponding optical responses are illustrated in Figure 24(a).



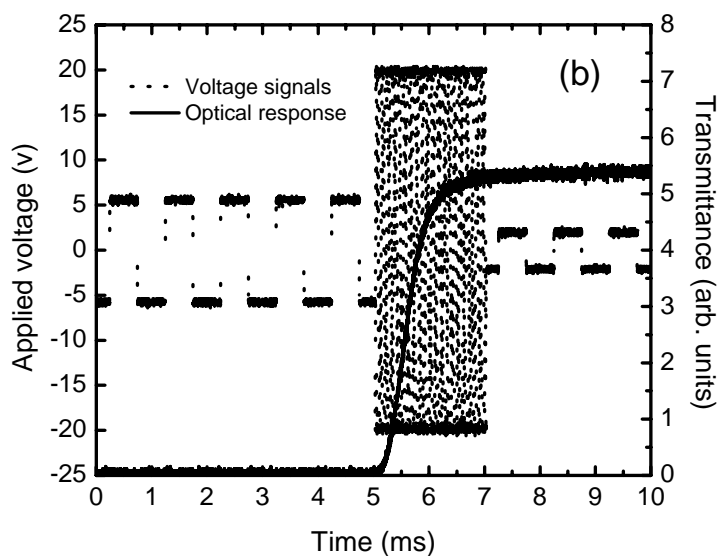
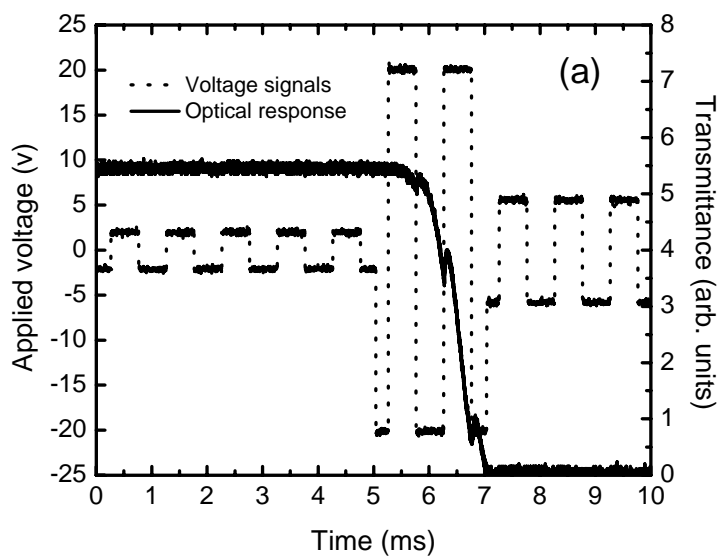


Figure 24: Overdrive and undershoot voltages and corresponding optical responses.

During the relaxation process, the constant bias voltage exerts a torque to resist LC molecules returning to their original positions. To overcome this bottleneck, a high-frequency ( $f=30$  KHz) voltage was imposed before applying the bias voltage. The

LC decay was thus accelerated, as depicted in Figure 24(b). This is known as the undershoot effect. The decay time (10-90%) was suppressed to 0.78 ms, which is approximately an order of magnitude faster than that of a commercial LC-VOA. From Figure 24(b), the 2 ms undershooting pulses are slightly longer than the required duration, which means that the decay process may even be somewhat improved for an optimized undershooting burst.

### 3.3.4 Discussions

The response times studied above are all between the VOA's "on" and "off" states. However, the dual frequency overdriving and undershooting also apply to the fast gray-scale transition between two arbitrary attenuation states. A high-voltage (e.g., 20  $V_{\text{rms}}$ ) burst of suitable frequency and duration may be inserted between the initial and target states to accelerate the LC director's rise or decay.

To further improve the VOA's response time, a DFLC with a higher dielectric anisotropy and a lower rotational viscosity is preferred. For some specific applications, we could increase the overdrive and undershoot voltages to further reduce response time. However, for normal fiber-optic applications, a high voltage is rarely used. Another simple and effective alternative is to use a reflective-type VOA, where the incident light passes the LC layer twice so that a cell with a half thickness may provide the same phase retardation. Because the free-relaxation response time  $\tau_0$  is proportional to the square of the cell gap, a four-times-faster response may be achieved. The only performance sacrifice is the slightly increased insertion loss due to the double pass. Although our

demonstrated VOA is a normally on device, it can also work in the normally off mode if the phase compensation cell changes  $\pi$  (or  $\pi/2$ ) phase retardation, where  $\pi$  (and  $\pi/2$ ) corresponds to that of transmissive-type (and reflective-type) VOAs.

### **3.3.5 Conclusion**

In summary, we proposed a DF-LC-based infrared VOA with a 43 dB dynamic attenuation range at room temperature. The submillisecond rise and decay times were achieved by integrating a 3.7  $\mu\text{m}$  small cell gap and high-performance dual-frequency LC material, as well as the overdrive and undershoot voltage technique.

## **CHAPTER 4: DUAL-FREQUENCY ADDRESSED HYBRID-ALIGNED NEMATIC LIQUID CRYSTAL**

### **4.1 Introduction**

Liquid crystal (LC) has been used extensively for information display,<sup>1</sup> laser beam steering,<sup>46</sup> spatial light modulator,<sup>47</sup> tunable photonic crystal,<sup>48</sup> and variable optical attenuator (VOA).<sup>71,72</sup> For intensity modulation, twisted nematic<sup>50</sup> and homeotropic<sup>51</sup> cells are commonly used because of their high contrast ratio and low operation voltage. However, for phase modulation, thin homogeneous cell is a favored choice because of fast response time and low operating voltage.<sup>52</sup> To obtain submillisecond response time, stressed LC,<sup>7</sup> polymer-network LC,<sup>8</sup> and high-pretilt dual-frequency LC<sup>53</sup> have been proposed. A common drawback of these approaches is that the operating voltage is quite high ( $\sim 100$  V<sub>rms</sub>). There is an urgent need to reduce the LC operating voltage for high speed LC phase modulators.

Hybrid aligned nematic (HAN) cell<sup>54</sup> is known to have no threshold voltage. In a HAN cell, as shown in Figure 25(a), the top substrate has homogeneous alignment while the bottom substrate has homeotropic alignment. Due to this special molecular configuration, the Freederisckz transition threshold no longer exists. It is therefore possible to achieve grayscales with low voltage which is very beneficial for displays and photonics applications.<sup>55</sup> However, a shortcoming of the HAN cell is that its phase retardation is only about one half of that of a corresponding homogeneous or homeotropic cell. For a LC optical phased array, a  $2\pi$  phase change is required. For a

transmission type VOA, there should be at least a  $\pi$  phase tuning range. The reduced phase change of the HAN cell limits its applications, especially for the photonic applications in the infrared region.

In this chapter, we present a dual-frequency liquid crystal (DFLC)<sup>40</sup> HAN cell for photonic applications with emphasis on VOA at  $l=1.5$  mm. We demonstrate theoretically and experimentally that the dual-frequency electric fields can effectively drive the LC molecules to either parallel or perpendicular position with respect to the substrates. The total obtainable phase change is equivalent to that of a homogeneous cell but at a lower voltage. Furthermore, the optical decay time is Five times faster than that using single frequency addressing. Finally, the DFLC HAN cell has three stable states at high frequency, low frequency, and zero field, respectively, some ternary optical devices are also proposed.

## **4.2 Operation principle**

When there is no external field across a HAN cell, the LC directors vary smoothly from a vertical state to a horizontal state, as shown in Figure 25(a), due to the different surface treatment. Using the Frank elasticity theory, assuming a strong anchoring at both substrates and using the single elastic constant approximation ( $k=k_{11}=k_{22}=k_{33}$ ), we obtain the initial elastic director orientation angle  $\phi_0(z) \approx \pi \cdot \frac{z}{2d}$ ,<sup>55</sup> which is approximately a linear function of the LC layer depth ( $z$ ), assuming the cell gap ( $d$ ) is along the  $z$  axis. The corresponding phase retardation  $\Gamma$  of this cell can be expressed as

$$\Gamma = \frac{2\pi}{\lambda} \cdot n_o \cdot d \cdot \left[ \frac{1}{d} \cdot \int_0^d \frac{dz}{\sqrt{(1 - R \cdot \sin^2 \phi)}} - 1 \right] \quad (7)$$

where  $R \equiv 1 - \frac{n_o^2}{n_e^2}$ ;  $n_e$  and  $n_o$  are the extraordinary and ordinary refractive indices, respectively;  $\lambda$  is the wavelength;  $\phi$  the LC director orientation angle which equals  $\phi_0$  in the field-off state. Although the actual  $\Gamma$  value is determined by the ratio between  $n_o$  and  $n_e$ , it can be proved that the phase retardation of a HAN cell is almost half of that a homogeneous (or homeotropic) cell, provided that the same LC material and cell gap are used. This is because the hybrid molecular alignment where the LCs near the bottom substrate (see Figure 25) makes smaller contribution to the observed phase change.

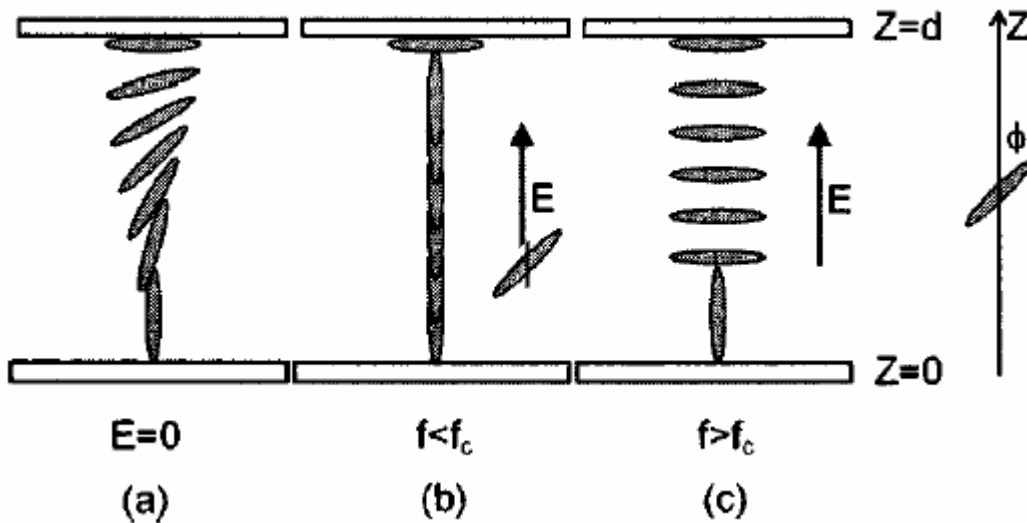


Figure 25: Schematics of a HAN cell. The rods represent the LC molecules with the director orientation of  $\phi(z)$ . (a) Initial state at  $V=0$ ; (b) a high voltage state at  $f < f_c$ ; (c) a high voltage state at  $f > f_c$ .

When a low-frequency electric field  $E$  is applied, the LC directors tend to follow the electric field so that the director orientation angle  $\phi(z)$  is changed. The equilibrium alignment in this field-on case can be determined by minimizing the total free energy

$$F = \frac{1}{2} \int_0^d \left\{ k \cdot \left[ \frac{\partial \phi(z)}{\partial z} \right]^2 - \Delta \varepsilon \cdot E^2 \cdot \cos^2 \phi(z) \right\} dz \quad (8)$$

where  $\Delta \varepsilon = \varepsilon_{//} - \varepsilon_{\perp}$  is dielectric anisotropy, defined by the difference of dielectric constant parallel and perpendicular to the LC director. Assuming a small molecular deformation, the director orientation angle change is given by

$$\phi(z) - \phi_0(z) = -\frac{\Delta \varepsilon \cdot E^2}{2 \cdot k} \left( \frac{d}{\pi} \right)^2 \sin\left( \frac{\pi \cdot z}{d} \right) \quad (9)$$

which is directly proportional to  $E^2$  and shows no threshold. However, for a DF LC mixture the  $\Delta \varepsilon$  is dependent on the driving frequency ( $f$ ).<sup>40</sup> When the frequency is below crossover frequency, i.e.,  $f < f_c$ ,  $\Delta \varepsilon$  is positive, but gradually changes to negative when  $f > f_c$ . In the high frequency regime, the DF LC behaves like a negative  $\Delta \varepsilon$  LC. Thus, the dielectric anisotropy  $\Delta \varepsilon(f)$  in Eq. (2) is frequency dependent. As a consequence,  $\phi(z)$  and  $\Gamma$  are all frequency dependent for a DF LC filled HAN cell.

### **4.3 Sample preparation**

To realize the frequency tuning in a HAN cell as predicted above, an 8.5  $\mu\text{m}$  HAN cell filled with our homemade DF LC is used for the experiments. The physical properties of our DF LC mixture at room temperature ( $T=25^\circ\text{C}$ ) are summarized as follows: crossover frequency  $f_c \approx 6\text{kHz}$ ,  $\Delta n = n_e - n_o = 0.24$  at  $\lambda = 1.55\mu\text{m}$ , and  $\Delta \varepsilon = +4.7$  at  $f=1\text{ kHz}$  and  $\Delta \varepsilon = -3.9$  at  $f=30\text{ kHz}$ . To measure the phase retardation, the DF LC HAN cell was placed between a pair of crossed polarizers.<sup>56</sup> An Ando AQ4321D tunable laser operating at  $\lambda = 1.55\mu\text{m}$  served as the light source. A computer controlled LabVIEW system was used for data recording and processing.

#### **4.4 Experimental results and discussions**

Figure 26 shows the measured phase modulation under different driving frequencies. The solid curve is for  $f=1$  kHz. Because of the positive  $\Delta\varepsilon$ , in the voltage-on state the LC molecules are reoriented along the field direction as described in Figure 25(b). The phase retardation thus decreases. When the frequency is elevated to 4 kHz, the phase retardation follows the similar trend but the phase modulation depth decreases due to the smaller  $|\Delta\varepsilon|$ . As  $f \sim f_c$  which is, 6 kHz, the LC directors are hardly reoriented. However, when  $f > f_c$ ,  $\Delta\varepsilon$  changes sign and becomes negative. The LC directors tend to be perpendicular to the electric field, as shown in Figure 25(c). In this case, the phase retardation increases with the applied voltage. The results of  $f=8$  kHz and  $f=30$  kHz are illustrated in Figure 26.



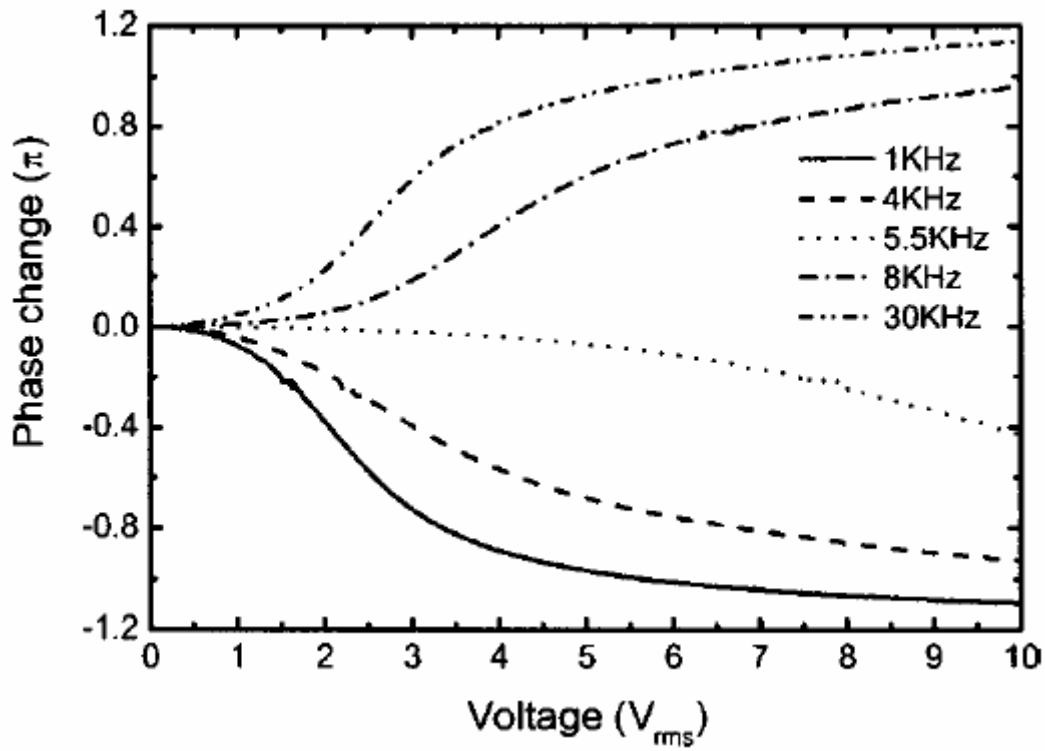


Figure 26: The measured phase change of an 8.5  $\mu\text{m}$  HAN cell as a function of the applied voltage under different driving frequencies. From bottom to top,  $f=1$ , 4, 5.5, 8, and 30 kHz.

From Figure 26, both voltage and frequency can be used to tune the DFCL HAN cell to a desired retardation state, which makes the active driving between two arbitrary states possible. To obtain a larger phase change, the cell normally works at frequencies far from the crossover frequency. In our DFCL mixture, our low and high frequencies are chosen to be  $f=1$  and 30 kHz, respectively. From Figure 26, if we apply a 1 kHz, 10  $V_{rms}$  voltage to the HAN cell, the maximum obtainable phase is  $-1.15\pi$  at  $\lambda = 1.55\mu\text{m}$ . This value is about 50% of the total phase retardation of an 8.5- $\mu\text{m}$ -thick homogeneous LC cell, which is  $2.63\pi$ . However, to obtain the maximum phase change of the DFCL HAN

cell, we could keep voltage at  $V=10 V_{rms}$  but change the frequency from 1 to 30 kHz. The total phase change is thus doubled, which is one of the main advantages of the DFLLC HAN cell.

To compare the DFLLC HAN cell with the homogeneous cell for phase modulation, Figure 27 displays their voltage dependent phase changes. The cell gap and the employed LC material are the same. The HAN cell is driven between 1 and 30 kHz, but the homogeneous cell is driven by a 1 kHz electric field. From Figure 27, the HAN cell has no threshold voltage while the homogeneous cell has  $V_{th} \sim 2V_{rms}$ . Therefore, to achieve the same phase change (say,  $1\pi$ ) the HAN cell has a lower operating voltage than the corresponding homogeneous cell.

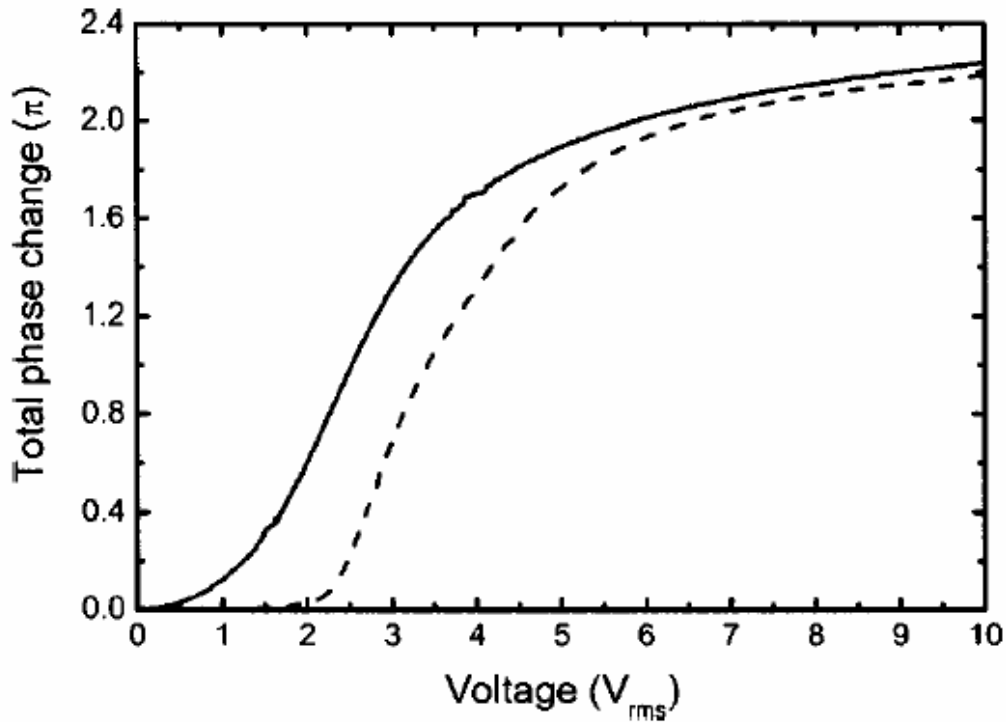


Figure 27: The total achievable phase changes of two  $8.5 \mu m$  LC cells in different alignments. The solid line is for the HAN cell, while the dashed lines are for a homogeneous cell.

Besides the lower operation voltage, the dual-frequency HAN cell also exhibits a much faster response time than the corresponding homogeneous cell. In a homogeneous cell, the rise time can be greatly improved by using the overdrive scheme.<sup>56</sup> However, the decay time relies on the elastic recovery of LC molecules; it is determined by the visco-elastic coefficient of the LC material and the cell gap.<sup>1</sup> To improve response time, polymer network liquid crystal has been considered. However, the high operating voltage and light scattering become serious concerns.<sup>8</sup>

The DF-LC HAN cell offers an advantage for improving response time. In both rise and decay periods, the electric field is present. As a result, both rise and decay time can be improved significantly. Figure 28 shows the optical decay time of a DF-LC HAN cell based zero-threshold VOA working at 1.55  $\mu\text{m}$ . A compensation film is employed so that the VOA is in the bright state at  $V=0$ . When a 5.8  $V_{\text{rms}}$  1 kHz signal is applied, the VOA is in its  $-\pi$  state which corresponds to the “OFF” state. At this time, if the field is removed the VOA changes from its OFF state to ON state. The transition time (10% to 90% intensity) is  $\sim 90$  ms, as shown by the solid line in Figure 28. This is to mimic conventional single frequency driving in a HAN cell. However, because of the dual frequency addressing of the DF-LC HAN cell, we keep voltage on the cell but switch frequency from 1 to 30 kHz for 35 ms before turning off the voltage. The high frequency electric field drives the LC molecules back. Thus, the optical decay time is shortened to  $\sim 18$  ms, as shown by the dashed lines in Figure 28.

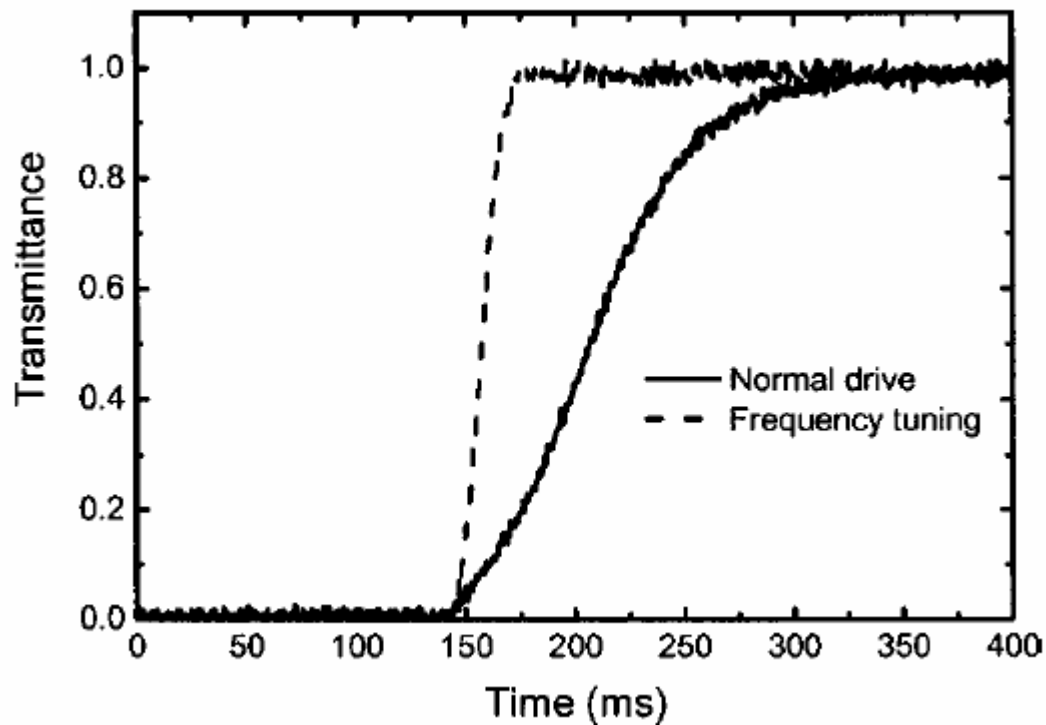


Figure 28: The optical decay time of an 8.5  $\mu\text{m}$  DFCL HAN cell based VOA. The solid line is the normal decay curve by instantly turning off the 5.8  $V_{\text{rms}}$  driving voltage. The dashed lines are for the dual frequency driving, where a 35 ms, 30 kHz voltage burst is used to assist the LC directors relaxation.

Similarly, we could drive the LC to  $+\pi$  phase state by applying a 6  $V_{\text{rms}}$  30 kHz field, then keep the voltage but decrease the frequency to  $f=1$  kHz to tune the VOA back to its ON state. We find that the response time is also remarkably improved, which means that the frequency tuning is really a simple and effective approach to accelerate HAN cell's optical response without scattering. To further improve the response time, the overdrive and undershoot scheme can be employed and a submillisecond response time can be achieved. The tradeoff is in need of a short and high overdrive voltage.<sup>53,57</sup>

A special feature of the above-mentioned VOA is that it has two stable “OFF” states:  $-\pi$  phase and  $\pi$  phase for the low- and high-frequency driving, respectively.

Although it has binary amplitude (0,1) states, it has ternary discrete phase (  $-1,0, +1$  or  $0,1,2$ ) states. The DF LC HAN cell thus supplies a simple tri-stable system in high-frequency, low frequency, and no-field states, respectively. Ternary system is nature's most efficient numbering scheme; it has attracted a lot of attention in different disciplines. The ternary states in LC materials and devices have been explored.<sup>58,59</sup> However, these approaches are either too complicated or not stable enough, while our DF LC addressed HAN cell could generate three stable states easily. Some applications, e.g., the ternary phase modulator, ternary logic device, and positive and negative tunable LC lens, by using the three stable states of the DF LC HAN cell are expected.

#### **4.5 Conclusion**

A dual-frequency addressed HAN cell for VOA application is demonstrated. The VOA shows no threshold voltage and a much faster response time. In comparison with the conventional single-frequency addressed HAN cell, the dual-frequency HAN cell has doubled phase retardation. Because of the unique tri-stability feature of the DF LC HAN cell, some applications such as the ternary optical devices are suggested.

## CHAPTER 5: POLYMER STABILIZED DUAL FREQUENCY LIQUID CRYSTAL MODULATORS

### 5.1 Introduction

Polymer-stabilized liquid crystal (PSLC)<sup>1,3,60</sup> is a fundamentally interesting and practically useful material system. Both anisotropic scattering<sup>61</sup> and scattering-free<sup>8</sup> PSLC systems have been developed depending on the polymer concentration and operating wavelength. The anisotropic light scattering PSLC is useful for amplitude modulation, e.g., reflective display, switchable polarizer, and variable optical attenuator (VOA).<sup>35,62,63,64</sup> On the other hand, the scattering-free PSLC is particularly attractive for phase modulation in the near infrared region.<sup>8</sup> In spite of amplitude or phase modulation, fast response time is a common desire. Especially for VOA operating in the near infrared region ( $\lambda=1.55 \mu\text{m}$ ), a larger cell gap is required which results in a longer response time. In order to keep response time short, a PSLC-based *reflective* VOA has been considered. For a 16- $\mu\text{m}$  reflective PSLC cell using Merck E44 LC mixture, the measured response time is  $\sim 30$  ms and dynamic range  $\sim 30$  dB at room temperature. If we use the cell parameters in transmissive mode, the dynamic range would be reduced to  $\sim 15$  dB. If we want to keep the same dynamic range, then we need to double the cell gap but the response time would be 4X slower.

In this chapter, we demonstrate a polarization-independent transmissive VOA using the polymer-stabilized dual-frequency liquid crystal (PS-DFLC) to obtain a large dynamic range (31 dB) while keeping 30 ms frame time. The unique feature of a DFLC is

that it exhibits a cross-over frequency ( $f_c$ ).<sup>41</sup> The dielectric anisotropy of the DF LC remains positive ( $\Delta\epsilon > 0$ ) when  $f < f_c$  but changes to negative when  $f > f_c$ . For practical applications, the cross-over frequency is usually in the 5-10 kHz range. For the DF LC-based homogeneous cell, we use a low frequency ( $\sim 1$  kHz) electric field to drive the VOA and use a high frequency ( $\sim 30$  kHz) electric field to accelerate the relaxation process. Due to the presence of electric field in both turn-on and turn-off processes, fast rise and decay times can be obtained simultaneously.

## **5.2 Light Modulation Mechanism for fast response variable optical attenuator**

Figure 29 illustrates the light modulation mechanism of the PS-DF LC cell. If a low frequency ( $f < f_c$ ) voltage is applied to the cell, as shown in Figure 29(a), the polymer networks tend to resist LC directors from being reoriented by the electric field. As a result, microdomains are formed which scatter the extraordinary ray because of the refractive index mismatch between the DF LC and the polymer networks. The ordinary ray is not affected because of good index match with the polymer matrix. If we keep the ac voltage unchanged but switch the frequency to a high frequency ( $f > f_c$ ), the electric field exerts a torque to bring the LC directors back to their original homogeneous position, as shown in Figure 29(b). Thus, the PS-DF LC cell is highly transparent. The anisotropic light scattering behavior of the PS-DF LC cell is polarization dependent. For fiber-optic communication, it is highly desirable to have a VOA whose performance is independent of light polarization.

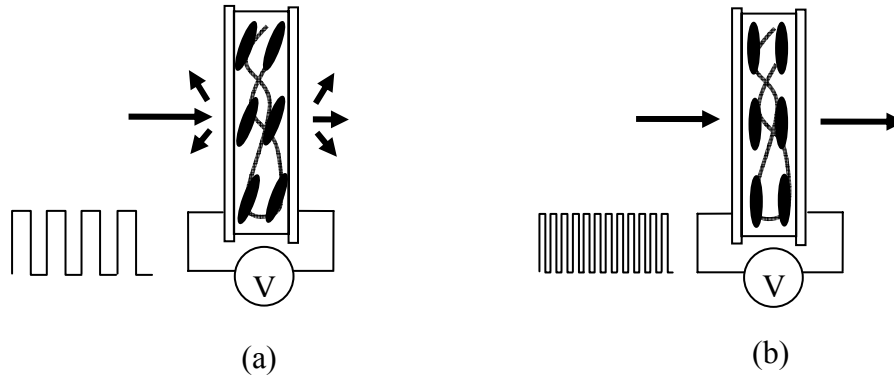


Figure 29: Light modulation mechanism of a PS-DFLC cell. (a) At low frequency (1 kHz), light scattering occurs for the extraordinary ray. (b) At high frequency (30 kHz), the device is highly transparent.

Since the PS-DFLC cell only attenuates the extraordinary ray, we need to convert the incident unpolarized light into a linearly polarized light. Figure 30 shows such a device configuration. The polarization beam displacer (BD) used in Figure 30 is a  $45^\circ$ -cut birefringence crystal, e.g.,  $\text{YVO}_4$  or calcite. Inside the beam displacer, the incident unpolarized light is separated into two components: ordinary ray (upper trace) and extraordinary ray (lower trace). The half-wave plate on the top part of the beam displacer transforms the ordinary ray into extraordinary. The rubbing axis of the PS-DFLC cell is positioned parallel to the polarization axis. The outgoing light intensity is modulated by the voltage applied to the LC cell. To recombine the two separated outgoing beams, a second but erected beam displacer is used, as depicted in Figure 30. Continuous optical attenuation can be achieved by varying the frequency or amplitude of the applied voltage. The preferred approach is to keep the same voltage while switching the frequency. A relatively fast rise and decay time can be obtained because electric field is present in both switching states. Increasing the bias voltage is favorable for shortening the rise and decay



times. However, a high voltage driver is costly. It is our interest to keep the operating voltage as low as possible.

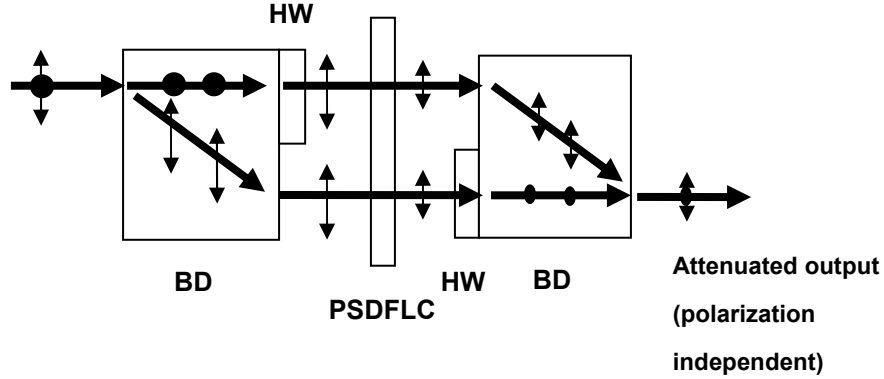


Figure 30: Polarization independent PS-DFLC-based VOA. HW: Half wave plate, BD: Beam displacer.  $\lambda=1.55 \mu\text{m}$ .

### 5.3 Experimental results and discussions

To fabricate the PS-DFLC cell, we mixed 4 wt% of a rod-like monomer bisphenol-A-dimethacrylate (M1) to DFLC-25. The physical properties of DFLC-25 mixture have described in previous chapter. The LC/monomer mixture was injected into an empty homogeneous cell with gap  $d=16 \mu\text{m}$  and then exposed to UV light ( $\lambda \sim 365 \text{ nm}$ ) at intensity  $I \sim 6 \text{ mW/cm}^2$  for  $\sim 30 \text{ min}$  at an elevated temperature and then followed by 4 hours at room temperature ( $25^\circ\text{C}$ ). After curing, the cross-over frequency of the PS-DFLC cell was found to increase from 6 to 8 kHz.

To characterize the PS-DFLC performance, a tunable laser (Ando AQ4321D) at  $\lambda=1.55 \mu\text{m}$  was used as the light source. Figure 31 depicts the voltage-dependent transmittance measured by a computer-controlled LabVIEW system. At  $f=1 \text{ kHz}$ , the

optical threshold voltage of the PS-DFLC ( $V_{th} \sim 8.5 V_{rms}$ ) is much higher than that of the pure DFCLC because of the polymer network effect.<sup>8</sup> As the applied voltage increases, light scattering gradually increases so that the transmittance decreases. The photodetector was set at 7 cm behind the second beam displacer, which corresponds to  $1.2^\circ$  acceptance angle. At  $V=24 V_{rms}$ , a good dark state is achieved and the measured dynamic range reaches 31dB. In an actual fiber-to-fiber system, the dynamic range should be higher than 31dB because of the smaller acceptance angle. The large dynamic range originates from two mechanisms: the enhanced light scattering from micron-sized domains, and large index mismatch between DFCLC-25 and polymer networks. To obtain gray levels, we simply vary the frequency of the bias voltage. For example, in Figure 30 if we bias the VOA at  $24 V_{rms}$  and increase the frequency from 1 kHz to 8 kHz, various gray levels can be obtained.

The dotted lines in Figure 31 represent the measured transmittance using a high frequency electric field. For a homogeneous cell at  $f=30$  kHz, the effective dipole of the LC directors is parallel to the electric field. Such an electric field cannot reorient the LC molecules so that the transmittance is independent of voltage.

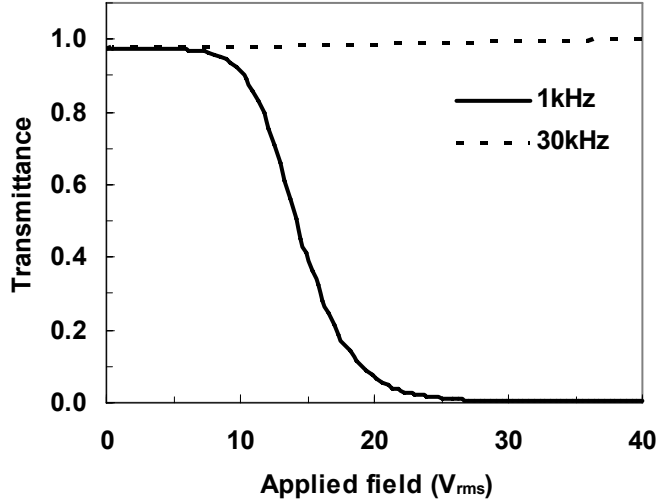


Figure 31: Voltage-dependent transmittance of a PS-DFLC-based VOA.  $\lambda=1.55 \mu\text{m}$ .

For fiber-optic applications, a VOA is desired to have a broad bandwidth over the whole spectral range defined by the International Telecommunication Union (ITU). To investigate the wavelength dependency, an ANDO ASE light source ( $\lambda=1525$  to  $1575 \text{ nm}$ ) and an optical spectrum analyzer were used. Figure 32 shows the wavelength dependent optical attenuation of the PS-DFLC VOA. The attenuation ratio remains relatively flat in the entire c-band. This is because the microdomain sizes are comparable to the wavelength.

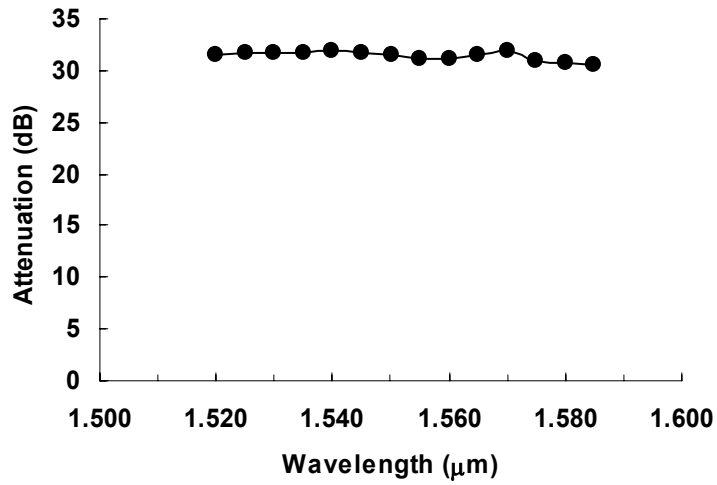


Figure 32: Wavelength-dependent attenuation ratio of the PS-DFLC VOA.

Polarization dependent loss (PDL) is another important parameter for fiber-optic application. Figure 33 plots the wavelength-dependent PDL of the VOA measured at normal-on state. The variation is around 0.1~0.2 dB. The PDL increases as the attenuation increases. The PDL at 15 dB attenuation is around 0.5 ~ 0.6 dB. Based on the data shown in Figure 32 and Figure 33, the PS-DFLC exhibits promising properties for VOA applications.

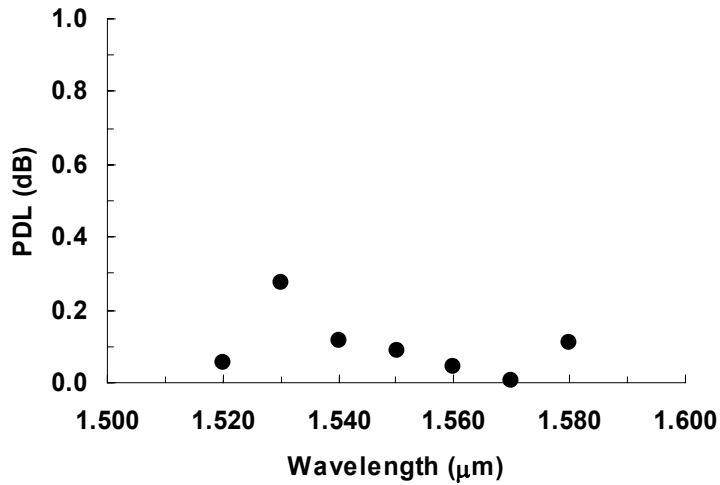


Figure 33: The measured polarization dependent loss (PDL) of the PS-DFLC VOA.  $d=16 \mu\text{m}$ .

#### **5.4 Discussion**

To obtain a wider dynamic range of a PS-DFLC device, we could increase the cell gap, LC birefringence, and UV curing temperature. Light scattering increases as the cell gap increases. However, the thicker cell gap leads to a slower response time and higher operating voltage. High birefringence liquid crystals help to increase the dynamic range due to the larger refractive index mismatch, but their viscosity is increased because of the elongated molecular structures. A higher viscosity increases the response time.

Curing temperature affects the domain size, dynamic range, and response time of a polymer-stabilized liquid crystal.<sup>65</sup> Figure 34 shows the relationship between the curing temperature and the measured total response (rise and fall) time. As the curing temperature increases, the response time of a regular PSLC cell increases dramatically. This is because the domain sizes increase with the increased curing temperature. In

contrast, the polymer-stabilized DF LC cell is inert to the curing temperature; its response time is kept at ~30 ms (rise time ~17 ms and decay time ~13 ms) when the curing temperature increases from 25°C to 120°C. This is because the rise and decay times of the polymer-stabilized DF LC cell are driven by the applied low and high frequency electric fields. Therefore, fast rise and decay time can always be achieved, regardless of the curing temperature. High curing temperature plays a key role for enhancing the dynamic range. Thus, we can use high curing temperature to achieve large dynamic range without sacrificing response time.

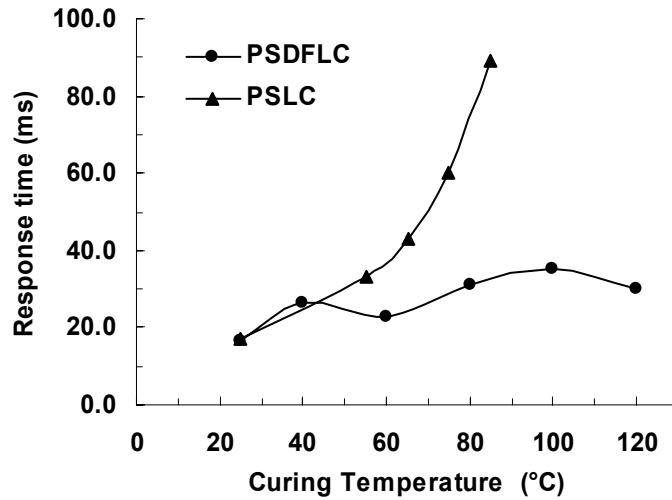


Figure 34: Curing temperature dependent response time of a PS-DFLC (circles) and a PSLC (triangles) cells.

In Figure 34, the PSLC data represent a reflective scattering-type VOA using a non-DFLC material.<sup>6</sup> If the same LC layer thickness is used for a transmissive PSLC device, the dynamic range would be lower than 15dB at  $\lambda=1.55\mu\text{m}$  in each curing temperature. In the present transmissive PS-DFLC VOA, the dynamic range is around 30

dB from 60 °C to 120 °C curing temperature. Therefore, the optical setup is much simpler while preserving a high dynamic range and fast response time.

To further improve the PS-DFLC VOA's response time, one could use the overdrive and undershoot method<sup>44,66</sup> or use a high birefringence and low viscosity dual-frequency liquid crystal mixture. The overdrive method is to shorten the rise time by applying a short but high voltage to kick the LC molecules to the desired tilt angle while undershoot is particularly useful for reducing the gray scale response time. Although the overdrive and undershoot method could lead to sub-millisecond response times, the required voltage is about 100 V<sub>rms</sub>.

The insertion loss of the PS-DFLC cell is around -3 dB due to the quadruple passes of the uncoated glass substrates and initial scattering effect in the transparent state. To further reduce the insertion loss, anti-reflection coating of the LC cell are recommended. In addition, by choosing proper polymer material to match the refractive index of the LC material, the insertion loss can be improved as low as possible. The hysteresis is small when employing higher curing temperature. For example, the hysteresis of the 120 °C curing temperature sample is smaller than 0.1 volts.

## **5.5 Conclusion**

We have demonstrated a transmissive VOA using a polymer-stabilized dual-frequency liquid crystal. By using the high birefringence dual-frequency LC material and polymer networks, we obtain a very high dynamic range and fast response time device. In addition, the response time does not increase with the increased curing temperature. Therefore, we could choose a higher curing temperature to achieve a larger

dynamic range without sacrificing the response time. The PS-DFLC approach can be extended to other scattering type devices for photonic applications.



## CHAPTER 6: SHEARED POLYMER NETWORK LIQUID CRYSTALS

### 6.1 Introduction

Nematic liquid crystal (LC)-based variable optical attenuator (VOA) has been used widely for fiber-optic telecommunications because of its low cost, gray scale capability, low optical loss, and low power consumption.<sup>35,63,64,67</sup> For these applications, fast response time (<1 ms) and large dynamic range (>30 dB) are highly desirable. The response time of a LC device is mainly determined by the visco-elastic coefficient ( $\gamma_1 / K_{11}$ ), LC cell gap ( $d$ ), and applied voltage.<sup>1</sup> In the near infrared ( $\lambda=1.55 \mu\text{m}$ ) region, to achieve  $1\pi$  phase retardation using a homogeneous cell the required  $d\Delta n$  (where  $\Delta n$  is the LC birefringence) is  $\lambda/2$ , or  $0.78 \mu\text{m}$ . High birefringence LC materials<sup>2</sup> help to reduce the required cell gap and therefore reduce the response time. However, high birefringence liquid crystals are usually associated with an increased viscosity and high melting temperature. The former can be overcome by operating VOA at an elevated temperature, but the latter is unfavorable for formulating eutectic mixtures. For practical applications, the melting temperature should be lower than  $-40 \text{ }^\circ\text{C}$  for the purpose of storage.

To obtain fast response time at room temperature, various polymer-stabilized liquid crystal (PSLC; also known as anisotropic gel) approaches have been investigated.<sup>4,3,6,5</sup> In a PSLC, the polymer concentration is 3-8 wt %. The response time decreases as the polymer concentration increases. Two problems associated with the LC

gels are strong light scattering and high operating voltage. As the polymer concentration increases, the operating voltage increases substantially.

Recently, stressed liquid crystal<sup>7</sup> and polymer-network liquid crystal (PNLC)<sup>8</sup> have been developed for achieving fast response time and scattering-free phase modulators. In a PNLC, rod-like monomers are used and the substrate surfaces are treated with homogeneous alignment. Usually, a PNLC exhibits strong light scattering in the visible spectral region. To suppress light scattering at  $\lambda=1.55 \mu\text{m}$ , a minimal polymer concentration of  $\sim 10\%$  is required in order to make domain sizes smaller than the wavelength. Under such a circumstance, the LC domains are surrounded by polymer networks so that the required operating voltage is increased substantially ( $\sim 7 V_{\text{rms}} / \mu\text{m}$ ).

Mechanical shearing of LC layer has been investigated on the starching plasticized PVA films containing 5-20 wt % LC for making scattering-type polarizers.<sup>9,10</sup> Similar shearing technique has also been applied to the polymer-dispersed LC composites for improving response time and reducing light scattering.<sup>7,11</sup> The major difference between stressed LC and PNLC is that the stressed LC uses a softer monomer NOA-65 ( $\sim 15 \text{ wt } \%$ ) and does not require surface alignment. A major technical challenge for the stressed LC is that it requires mechanical shearing after the two-step UV curing in order to eliminate light scattering. Before shearing, the cell scatters light strongly. After shearing, the cell becomes highly transparent in the near IR region. The stressed LC has potential for display applications, provided that the operating voltage can be reduced and the light scattering in the blue region can be eliminated.

In this chapter, we demonstrate a reflective-mode normally-on VOA using a sheared PNLC cell. The measured response time at room temperature is  $\sim 0.24 \text{ ms}$  and dynamic range is  $-32 \text{ dB}$  at  $\lambda=1.55 \mu\text{m}$  and voltage  $V \sim 35 V_{\text{rms}}$ .

## **6.2 Sample fabrication**

To prepare a PNLC cell, we mixed 15 wt % of photopolymerizable monomer (Norland optical adhesive NOA65) in a commercial Merck E7 LC mixture. The mixed LC and monomer was sandwiched between two ITO (indium-tin-oxide) glass substrates separated by two stripe mylar spacers. The cell gap was controlled at  $\sim 9 \mu\text{m}$ . To polymerize the LC cell, a two-step UV curing process was adopted.<sup>7</sup> In the first step, the LC cell was illuminated to a UV light ( $\lambda \sim 365 \text{ nm}$ ,  $I = 50 \text{ mW/cm}^2$ ) for 15 min at  $T = 110 \text{ }^\circ\text{C}$ . The clearing temperature of E7 is  $\sim 60 \text{ }^\circ\text{C}$ . In the second step, the cell was cured in the same condition but at  $20 \text{ }^\circ\text{C}$ . Since the ITO glass has no surface treatment, the LC domains are randomly distributed so that the cell appears translucent after UV curing. In order to align the LC molecules in a uniform direction, we applied a shearing force to the top substrate while keeping the bottom glass substrate fixed. The shearing distance and speed were controlled by a precise motor motion system (Newport ESP-300). The shearing speed was controlled at  $0.1 \text{ mm/s}$  and the shearing distance was  $\sim 400 \mu\text{m}$ . After shearing, the PNLC cell became highly transparent. To prevent the sheared LC molecules from relaxing back, the peripherals of the cell were hermetically sealed by a UV adhesive. All our measurements were performed using the sealed LC cell. No noticeable performance change was detected before and after the hermetic sealing. Throughout this article, we abbreviate the sheared polymer-network liquid crystal as SPNLC.

## **6.3 Theory of sheared polymer network liquid crystal**

Figure 35 shows the shearing processes and LC director orientation of a SPNLC cell. During UV exposure, the bottom substrate faced the UV light. After the two-step

curing processes, a thin (sub-micron) isotropic polymer composite film<sup>68</sup> and polymer networks were formed. However, these LC microdomains in the polymer networks are randomly distributed, as sketched in Figure 35 (a). The film scatters light because of the refractive index mismatch between the LC and the polymer matrix. After shearing, the LC domains are aligned and light scattering is eliminated. Since the shearing force has gradient distribution, each layer of LC microdomains is expected to have different tilt angles, as depicted in Figure 35(b). Near the top substrate, the shearing force is strong so that the LC domains are aligned nearly parallel to the substrate. Deeper from top substrate, the shearing torque is weaker so that the LC tilt angle is larger. This gradient tilt angle distribution makes important contributions to the electro-optic properties of the SPNLC cell. Firstly, the increased tilt angle smears the threshold behavior. For a PNLC without gradient tilt angle, its threshold voltage is quite high. Secondly, the gradient tilt angle lowers the dark state (between crossed polarizers) voltage. However, the gradient tilt angle reduces the effective birefringence of the LC layer. At  $\lambda=1.55 \mu\text{m}$ , the effective birefringence of the E7/NOA65 mixture (85:15 wt % ratios) is  $\sim 0.17$ , but the average birefringence of the SPNLC is decreased to  $\sim 0.12$ . Some LC molecules could be imbedded in the polymer networks, but the major birefringence loss is believed to originate from the tilted LC alignment.

The response time of the SPNLC is governed by the domain size, shape, and polymer network binding strength, and is insensitive to the cell gap. We could increase the cell gap to obtain more phase change without sacrificing response time. The tradeoff is the increased voltage.

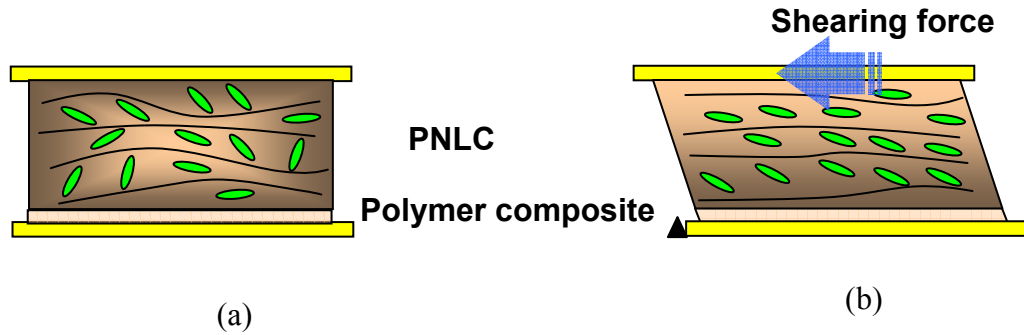


Figure 35: Shearing processes and LC domain orientations of the SPNLC film. (a) Before and (b) after shearing.

## **6.4 Properties of sheared polymer network liquid crystal**

### **6.4.1 Cell gap independent response time**

To prove that the SPNLC exhibits a fast response time and large phase change, we measured the electro-optical properties of a SPNLC cell. Figure 36 shows the voltage dependent transmittance of several SPNLC cells whose gap is thicker than 10  $\mu\text{m}$ . The results were measured at  $\lambda = 632.8 \text{ nm}$ . Compared to the pure E7 liquid crystals, the driving voltage of the SPNLC cells is over 100 volts. This is because the LC directors inside the SPNLC are anchored strongly by the sub-micron sized polymer networks. As a result, the required operating voltage is high. From Figure 36, there is almost no threshold voltage for the SPNLC cell because of the high pretilt angle of the HAN structure. Figure 37 shows the maximum phase retardation change in each cell studied. The phase retardation increases as the cell gap increases. The maximum phase change reaches  $5\pi$  for the 38  $\mu\text{m}$  cell gap. Light scattering remains negligible even though the

cell gap is larger than 38  $\mu\text{m}$ . This is a very attractive feature for the LC phase modulators which demand a fast response time and a large phase change.

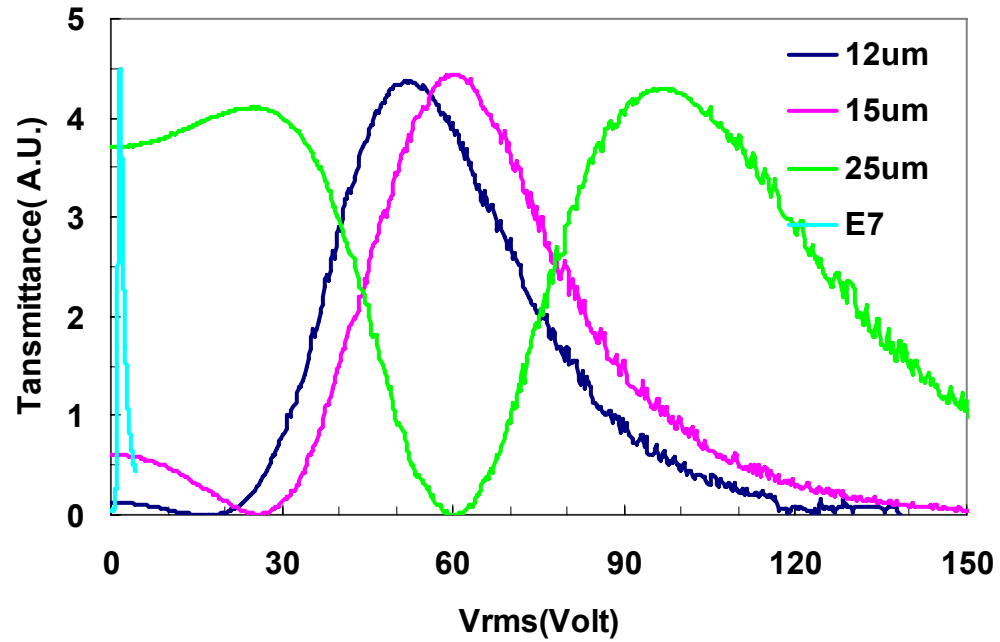


Figure 36: Voltage dependence transmittance curve in various cell gaps.

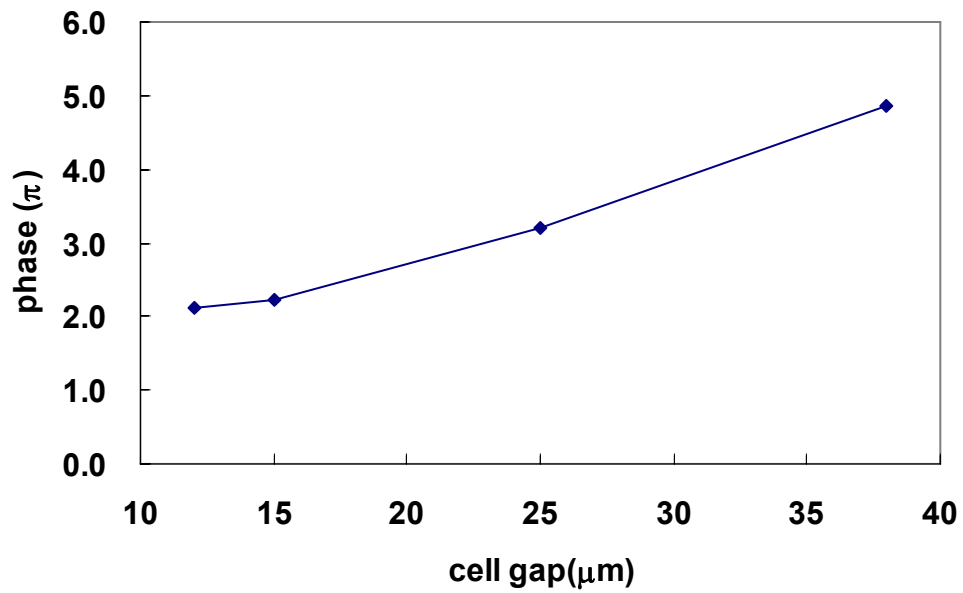


Figure 37: Maximum phase retardation change increases with the cell gap.

In order to obtain the response time for the phase change, we convert the measured time-dependent transmittance data into phase. Figure 38 plots the phase decay time for four different cell gaps. The slope of each cell gap within the first  $\pi$  phase change is almost the same, meaning the response time is independent of the cell gap.

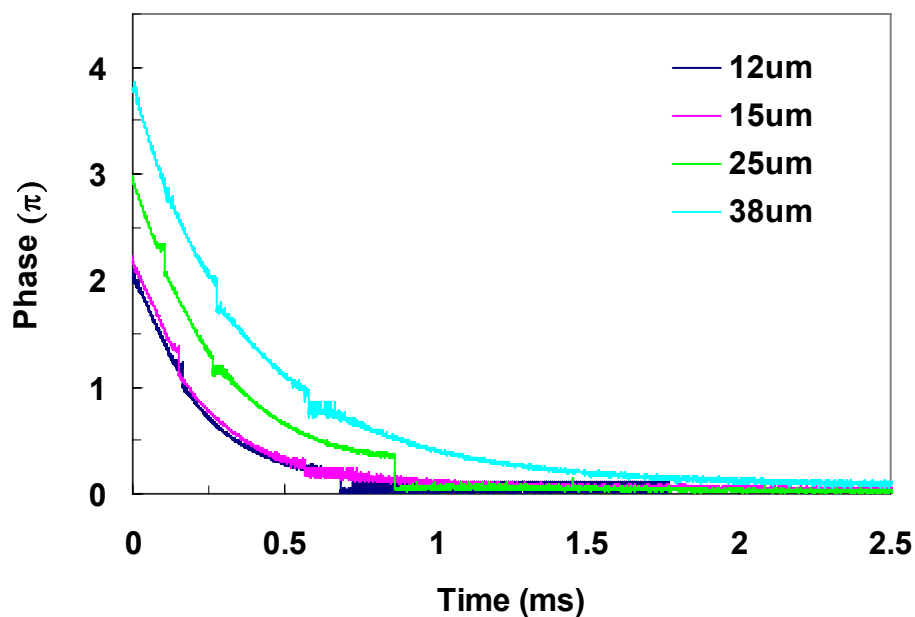


Figure 38: Transient phase decay time of four SPNLC cells.

Figure 39 shows the measured relaxation time constant as a function of cell gap. The response time is less than 1 ms as cell gap is smaller than 40  $\mu\text{m}$ . The response time increases less than 0.4 ms as the cell gap change from 10  $\mu\text{m}$  to 40  $\mu\text{m}$ . Compare to the response time of the pure liquid crystal without polymer network, the response time of 10  $\mu\text{m}$  and 40  $\mu\text{m}$  has 16 times different. The SPNLC has almost the same response time as the cell gap increases. Therefore, we claim the response time is independent of the cell gap.



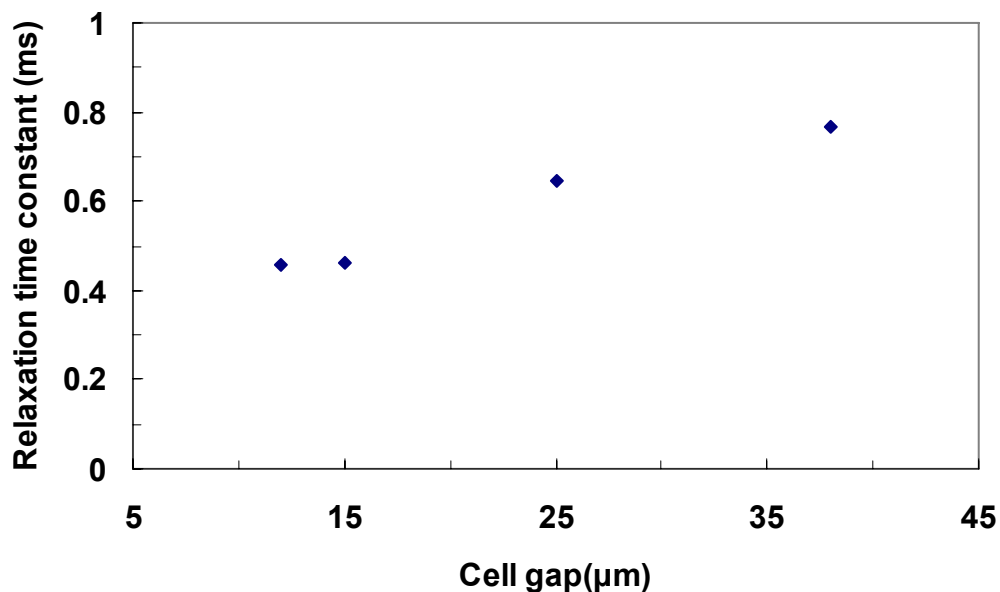


Figure 39: Relaxation time constant as the function of the cell gaps.

#### 6.4.2 SPNLC composite layer

As shown in Figure 35, there is a polymer composite film formed under the PNLC layer. This composite film is formed in some SPNLC samples. It contains high density polymer network with few liquid crystals. It is hardly driven by the electric field and can be treated as a passive compensation film. The composite film is formed on the glass substrate which faces to the light source during the UV exposure process. This is because the side which faces the light source receives stronger UV intensity and generates higher density polymer network. Figure 40 is the evidence showing the existence of this composite film which has compensation film effect. In Figure 40, the transmittance curve of the SPNLC cell does not touch zero (the perfect dark state) in the high voltage region

where nearly all the liquid crystal directors are reoriented perpendicular to the glass substrates. That means the SPNLC sample contain residual phase retardation.

Furthermore, Figure 41 shows a SPNLC sample cell with or without a compensator. We intend to choose a SPNLC sample which does not have any residual phase retardation in the high voltage regime as an example. An 8- $\mu\text{m}$  E7 homogenous cell was employed and applied at 1.65  $V_{\text{rms}}$  to function as a phase compensator. After adding this compensator to the SPNLC sample, the voltage dependent transmittance curve (blue solid line) shows the same result as Figure 40. That implies the curve in Figure 40 consists of a phase compensator. In other word, the composite film exists and has compensation effect. This is an indirect verification for the compensation effect of the composite film.

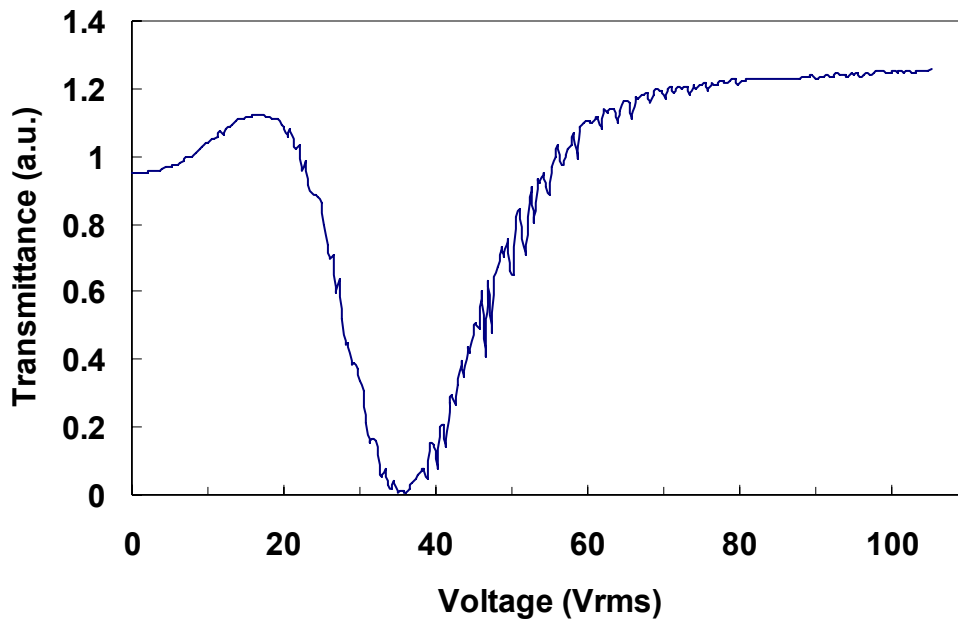


Figure 40: SPNLC sample with a composite film which has the compensation film effect.

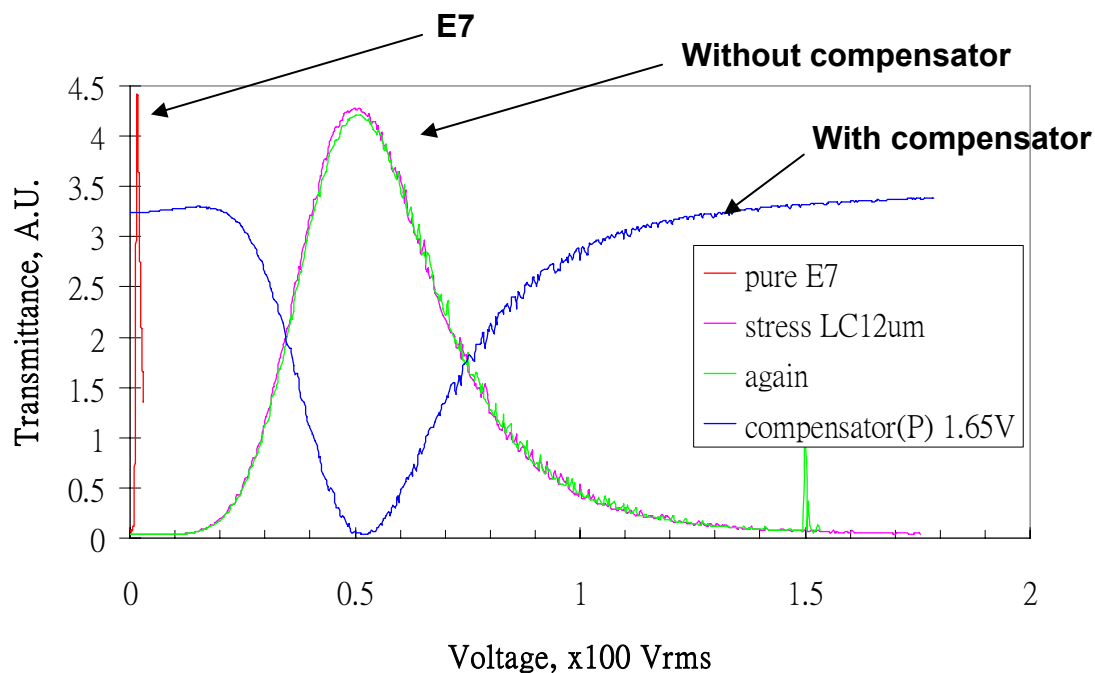


Figure 41: SPNLC cell with or without a compensator.

### 6.4.3 SPNLC morphologies

Figure 42 shows the SPNLC morphologies before and after the shearing process. The picture was taken by the optical microscope (50X) under crossed polarizers. These two structures have similar morphologies except their colors are different. There are many small sub-domains which consist of liquid crystal inside the small cavities. When we rotate a SPNLC sample before the shearing process, the color of the sub-domain will not change too much. It is direct evidence that the liquid crystal is randomly distributed around the domain. After shearing, a significant color change is observed when rotating the SPNLC sample. The color change is caused by the birefringence of the liquid crystal

molecules within the domain. That means the liquid crystal directors are aligned along the shearing direction after the shearing process. Therefore, the color change is easy to observe.

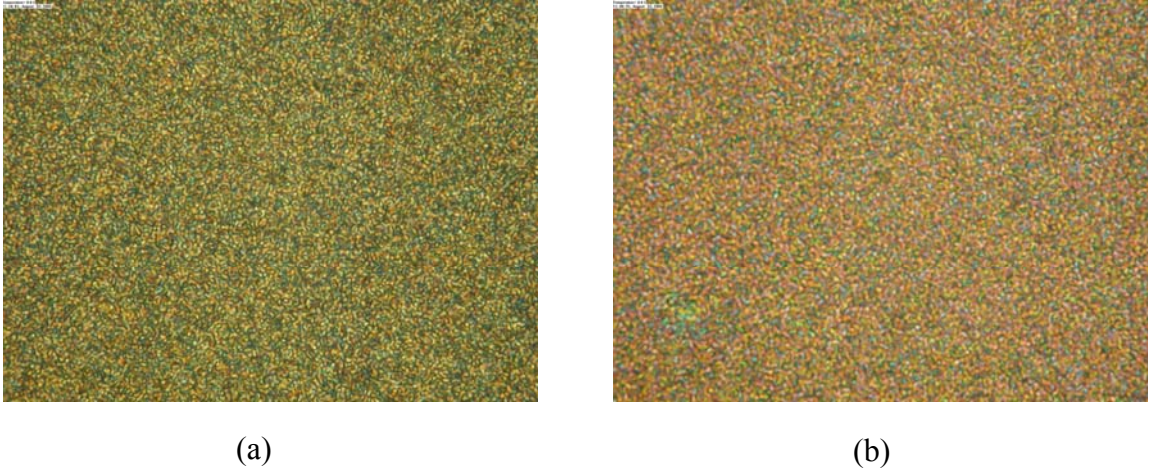


Figure 42: SPNLC morphologies (a) without and (b) with a shearing force.

Figure 43 shows the transmittance with respect to the rotation angle of a SPNLC cell. It also proves that the LC directors are aligned along in the same direction. In Figure 43, the transmittance curve fit the electro-optical properties of the homogeneous cell,  $T = T_0 \cdot \sin^2(2 \cdot \phi)$  where  $\phi$  is the orientation of the sample.

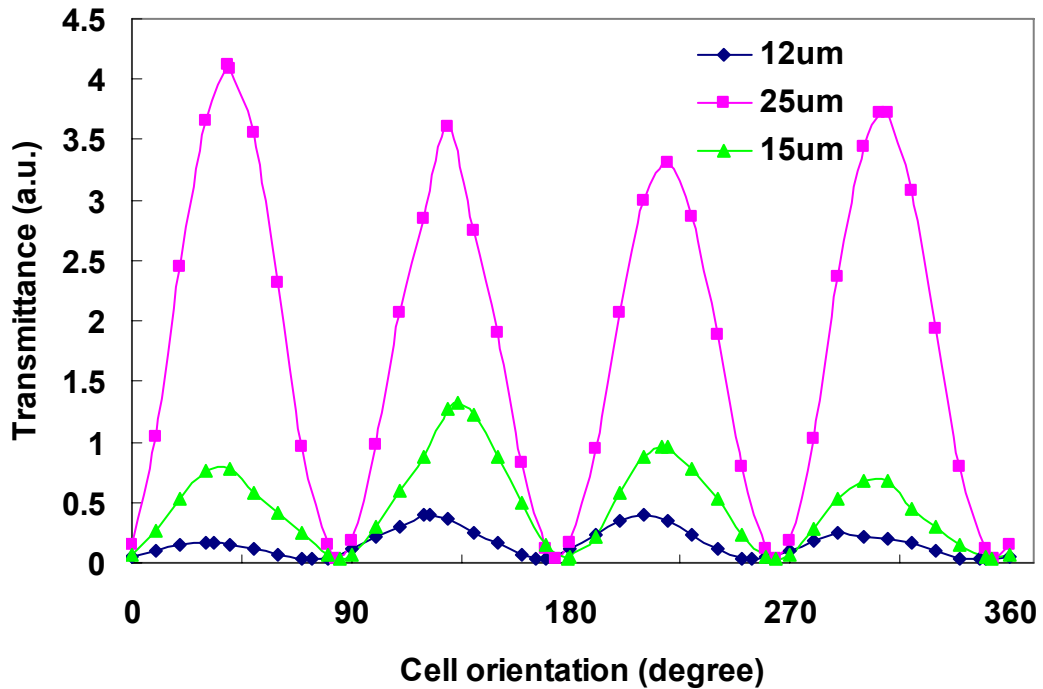


Figure 43: The transmittance with respect to the rotation angle of SPNLC cell

## **6.5 Sheared vertical aligned polymer network liquid crystal**

### **6.5.1 Motivation**

A SPNLC exhibits attractive features such as fast response time, large phase change, and scattering free. However, the driving voltage is high and there is a need to further suppress the light scattering due to the random distribution of the liquid crystal directors. In order to eliminate the light scattering completely, we need to shear a longer distance to better align the liquid crystal. This action would cause the driving voltage to increase and break the polymer network. In contrast, PNLC is easier to fabricate because it does not require the shearing process. PNLC also possesses fast response time and is

free from scattering in the near infrared region. The scattering behavior of both PNLC and sheared PNLC depends on the  $d\Delta n$  and wavelength. For a given wavelength and LC material, a thicker cell gap would lead to a larger phase change, but the tradeoffs are larger scattering loss, higher operating voltage, and increased response time.

To minimize light scattering, we propose to shear the vertical aligned polymer network liquid crystal. We call it VA-SPNLC. There are several reasons to use this approach. First, the VA alignment has very good alignment properties in the initial state. If we shear a VA cell, we may get a larger phase change and put less effort to align the random molecules like the above-mentioned SPNLC method. Second, we can use the PNLC formula to fabricate the scattering-free polymer network. Although the PNLC has strong light scattering properties, the shearing process would eliminate the scattering problems in the visible spectral range. Third, the expected driving voltage is lower than the SPNLC method because the VA has better alignment than the SPNLC.

The biggest problem incurred in SPNLC is the flexibility of the polymer network. Not every PNLC composition can afford the stress. That means some of the polymer network cannot afford the long shearing process. Some polymer networks will break even the shearing distance is short because they are too rigid. We intend to change the polymer network ingradient and increase its flexibility by adding different monomers with various concentrations. There are few monomers that can withstand the shearing stress.

In this chapter, we report the study results and discuss the possibility of making faster response, lower driving and larger phase change devices by using a vertically aligned sheared polymer network liquid crystal.

### 6.5.2 VA-SPNLC fabrication process

To fabricate a VA-SPNLC, we tried three kinds of monomers, AMA, (1,3) BDA, and (1,4) BDA. These monomers do not contain any benzene in the structure. The best result is the PNLC using (1,3) BDA in a commercial Merck E44 LC mixture. The mixed LC and monomer was sandwiched between two ITO-glass substrates. The cell gap was controlled at  $\sim 9 \mu\text{m}$ . To polymerize the LC cell, a two-step UV curing process was adopted.<sup>7</sup> In the first step, the LC cell was illuminated to a UV light ( $\lambda \sim 365 \text{ nm}$ ,  $I = 50 \text{ mW/cm}^2$ ) for 15 min at  $T = 110 \text{ }^\circ\text{C}$ . In the second step, the cell was cured in the same condition but at  $20 \text{ }^\circ\text{C}$ . Since the ITO glass has vertical alignment treatment, the LC domains are vertically distributed. The cell is transparent after UV curing because of the good liquid crystal alignment. In order to get a phase change, we applied a shearing force to the top substrate while keeping the bottom glass substrate fixed. The shearing distance and speed were controlled by a precise motor motion system (Newport ESP-300). The shearing speed was controlled at  $0.1 \text{ mm/s}$  and the shearing distance was  $\sim 100 \mu\text{m}$ . After shearing, the PNLC cell is still transparent. To prevent the sheared LC directors from relaxing back, the peripherals of the cell were hermetically sealed by a UV adhesive.

Figure 44 shows the shearing process of the VA-SPNLC. After the UV curing process, VA-SPNLC cell is transparent and polymer network grows vertically along the liquid crystal alignment. Then, we applied the shearing process to align the LC directors along the shearing direction and have tilt angles. The longer the shearing distance, the larger the phase change due to the more pronounced birefringence effect from the reoriented liquid crystal layer.

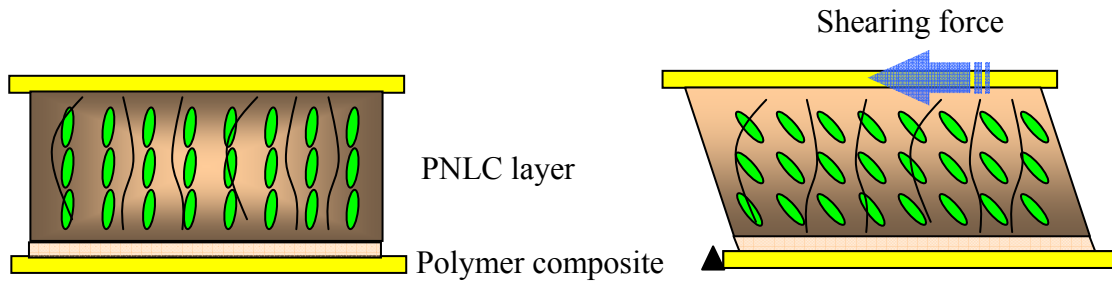


Figure 44: The VA-SPNLC shearing process.

### 6.5.3 Experiment results

Figure 45 plots the voltage-dependent transmittance of the VA SPNLC and pure E44 sample at  $\lambda=1.55 \mu\text{m}$ . The cell gap is around  $9 \mu\text{m}$ . The VA-SPNLC cell was addressed by 1 kHz square waves. There is no threshold voltage because of the large pretilt angle. Compared to the traditional SPNLC, the VA SPNLC has a more uniform LC alignment structure after the cell is sheared. That also means less phase loss. In reference to a pure E44 cell, the VA-SPNLC is almost scattering-free. As the applied voltage increases, the detected phase also increases. At  $70 V_{\text{rms}}$ , the phase change is about  $1.25\pi$  and at  $V=160V_{\text{rms}}$ , the corresponding phase change reaches around  $1.6\pi$ .



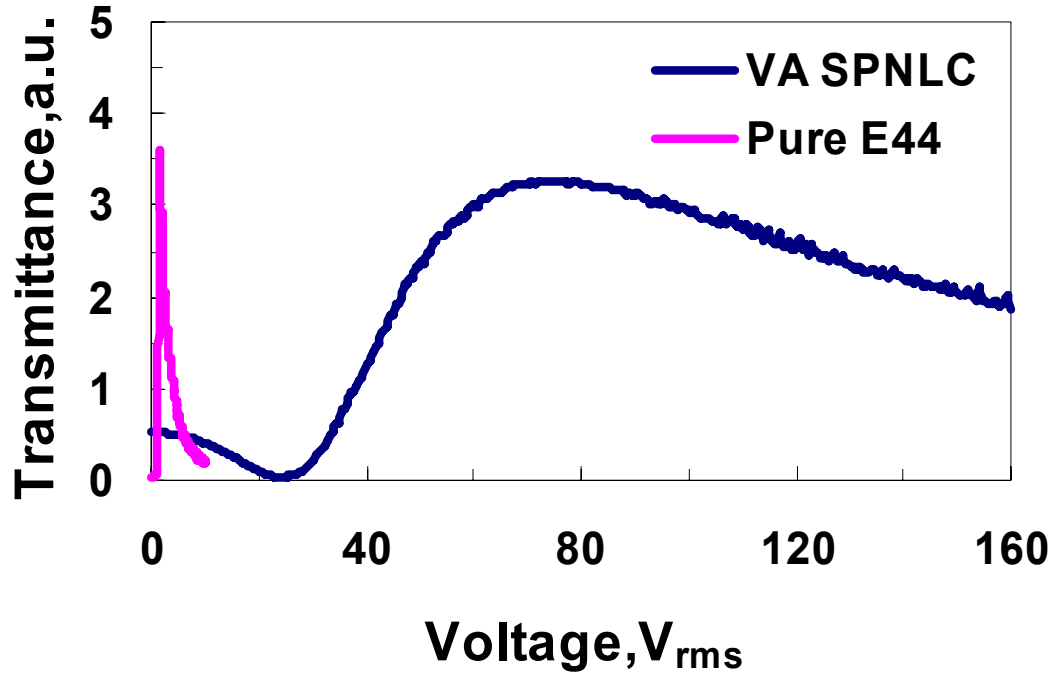


Figure 45: The voltage dependent transmittance curve of the VA SPNLC and pure E44 sample between crossed polarizers. The cell gap  $d \sim 9 \mu\text{m}$ , and  $\lambda = 1.55 \mu\text{m}$ .

Figure 46 shows the dynamic response of the VA-SPNLC under different driving voltages (at  $\lambda = 1.55 \mu\text{m}$ ). To measure the response time, a  $160 V_{\text{rms}}$  (upper traces) at  $f = 1$  kHz square waves with 1 s duration was periodically applied to the VA-SPNLC cell. The rise time and fall time are defined as 10 $\rightarrow$ 90% and 90 $\rightarrow$ 10% transmittance change, respectively. The measured optical response times are shown in the lower traces. Figure 46(a) and (b) show the optical rise and decay times, respectively. From Figure 46, we find the rise time is  $10 \mu\text{s}$  and decay time is  $980 \mu\text{s}$ . The corresponding phase change is around  $1.4 \pi$ .

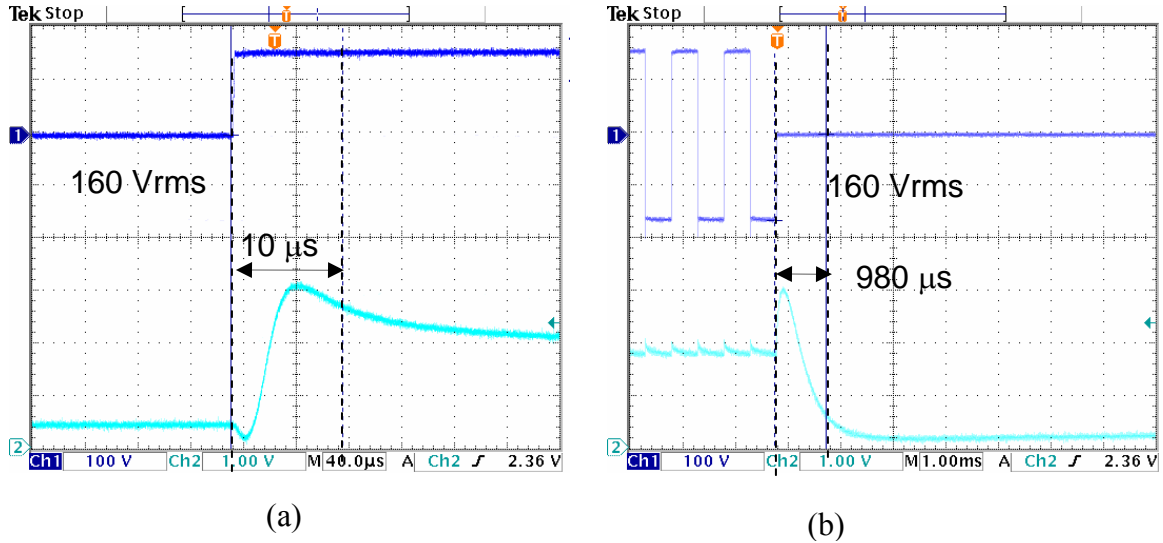


Figure 46: Optical response time of the VA-SPNLC cell at  $V=160V_{rms}$ : (a) rise time, and (b) decay time. Cell gap  $d\sim 9\ \mu\text{m}$  and  $\lambda=1.55\ \mu\text{m}$ .

If we applied a lower voltage, the phase retardation change would be smaller. Figure 47 shows similar response time results for the  $1\ \pi$  phase change. The total response time becomes faster. From Figure 47, we find the rise time is  $190\ \mu\text{s}$  and decay time  $404\ \mu\text{s}$ . The faster rise time of the Figure 46 is caused by the initial acceleration with a larger voltage swing. The slower decay time in Figure 46 results from the larger phase change which takes a longer time to relax back to the original homotropic state. Although Figure 46 and Figure 47 show the different response time characteristics under different driving conditions, their total response time are all below 1 ms. In order to use for fast liquid crystal modulators, the performance optimization between the applied voltage and response time is needed.

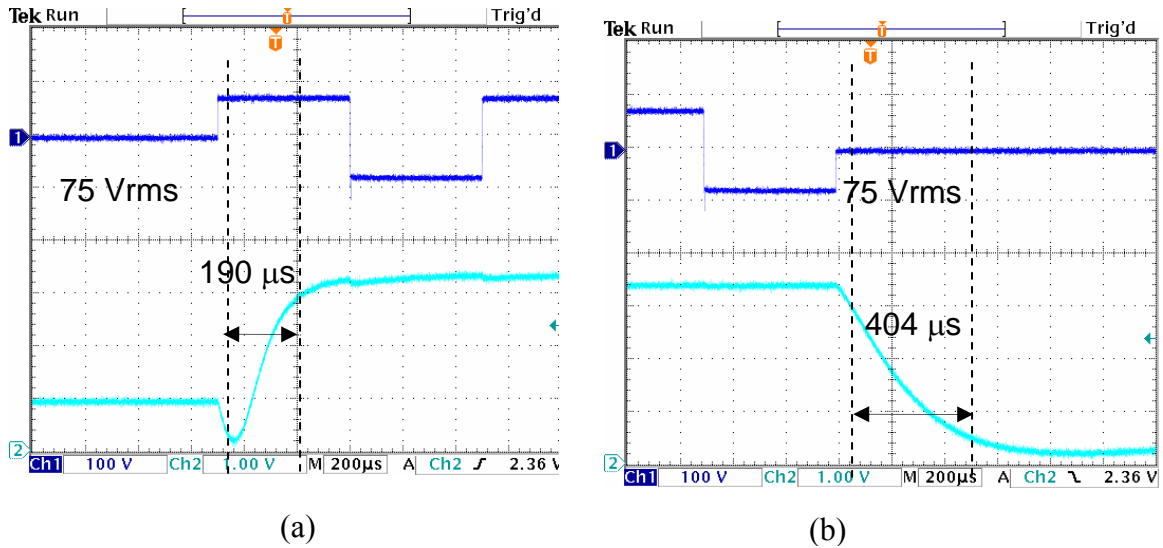


Figure 47: Optical response time of the VA-SPNLC cell at  $V=75 V_{rms}$ : (a) rise time, and (b) decay time. Cell gap  $d\sim 9 \mu m$  and  $\lambda=1.55 \mu m$ .

#### 6.5.4 Discussion and future work

We have demonstrated a VA-SPNLC modulator with submillisecond response time. The phase change is over  $2\pi$  at  $\lambda=1.55 \mu m$  when the driving voltage is over  $200 V_{rms}$ . It is almost scattering-free at IR. There are several improvements we can make in the future work. First, to obtain a larger phase change and lower driving voltage, we need to search a new polymer network which has sufficient flexibility to afford the shearing stress. To do this, we can optimize the monomer concentration and try out different kinds of monomers. Thus, we can make a longer shearing distance to gain larger phase change. Second, to improve the response time, we can optimize the driving scheme to achieve the best performance between the driving voltage and the maximum phase retardation change.

Third, to obtain a larger phase change, we can make a larger cell gap while suppressing scattering-free in the visible to IR spectral range.

### **6.6 VOA experiment and results**

Figure 48 depicts the schematic diagram of a SPNLC-based VOA. The light source ( $\lambda=1.55 \mu\text{m}$ ) could come from a tunable laser source (ANDO AQ4321D) or from an ASE light source. The port 1 of a fiber-optic circulator is connected to the light source, port 2 to the collimator with an 8-cm working distance from a mirror, and port 3 to an optical spectrometer or a photo-detector. A phase modulator module is located between the collimator and the dielectric mirror. An ac voltage is applied to the LC cell for controlling the phase retardation through LabVIEW data acquisition system. By adjusting the driving voltage, we can modulate the light transmittance of the phase modulator. The reflected light from the mirror through the phase modulator module is collected by the same collimator. The circulator redirects the reflected light to port 3 which is captured by a spectrometer or a detector.

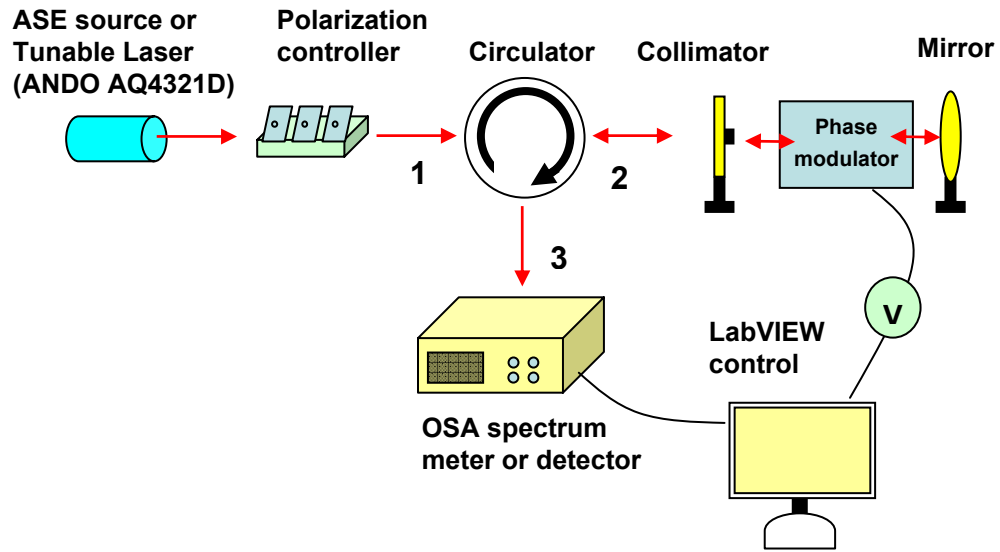


Figure 48: The schematic diagram of a SPNLC-based VOA.

The detailed operation mechanism of the phase modulator module is illustrated in Figure 49(a) and (b). The module contains a polarization beam displacer (PBD), a half-wave plate (HWP) which is laminated on the backside (upper half) of the PBD, a quarter-wave plate (QWP), and a SPNLC cell. Figure 49 (a) shows the ON state (i.e.,  $V=0$ ) of the VOA. At  $V=0$ , the LC directors of the SPNLC cell are aligned along the sheared direction. The optical axes of the SPNLC and QWP are crossed, thus, their phase retardations are subtractive. Let us assume the incident light is unpolarized. When the light impinges the PBD, it is separated into two components: ordinary (top trace) and extraordinary (bottom) rays. The ordinary ray traverses through the HWP and becomes the extraordinary ray. At this stage, the incoming unpolarized light is converted to a linearly polarized light. In this experiment, the SPNLC cell is intentionally designed to possess a quarter-wave phase retardation ( $\delta=\pi/2$ ) at  $\lambda=1.55 \mu\text{m}$ . Thus, the phase of

SPNLC cancels with that of QWP. Upon reflection from the mirror, the total phase difference of the outgoing beams from QWP remains 0. Therefore, two retro-beams have the same polarization states as they enter the QWP and will go back to the PBD along the same paths as shown in Figure 49 (a). This is the normally-on state of the VOA.

Figure 49(b) shows the off-state of the VOA. At  $V=35 V_{\text{rms}}$ , the phase retardation of the SPNLC cell is vanished (i.e.,  $\delta \sim 0$  at  $\lambda=1.55 \mu\text{m}$ ). Therefore, the SPNLC cell causes no phase retardation to the incoming beams. The incoming beams only experience a  $\pi$  phase change after having passed the QWP twice. The polarization states of the top and bottom outgoing beams from QWP remain linear except that they have been rotated by  $90^\circ$ . As a result, they go back to the PBD at different paths. No light is coupled into the collimator, as shown in Figure 49(b). This is the dark state of the VOA. The gray levels can be obtained by controlling the applied voltage.

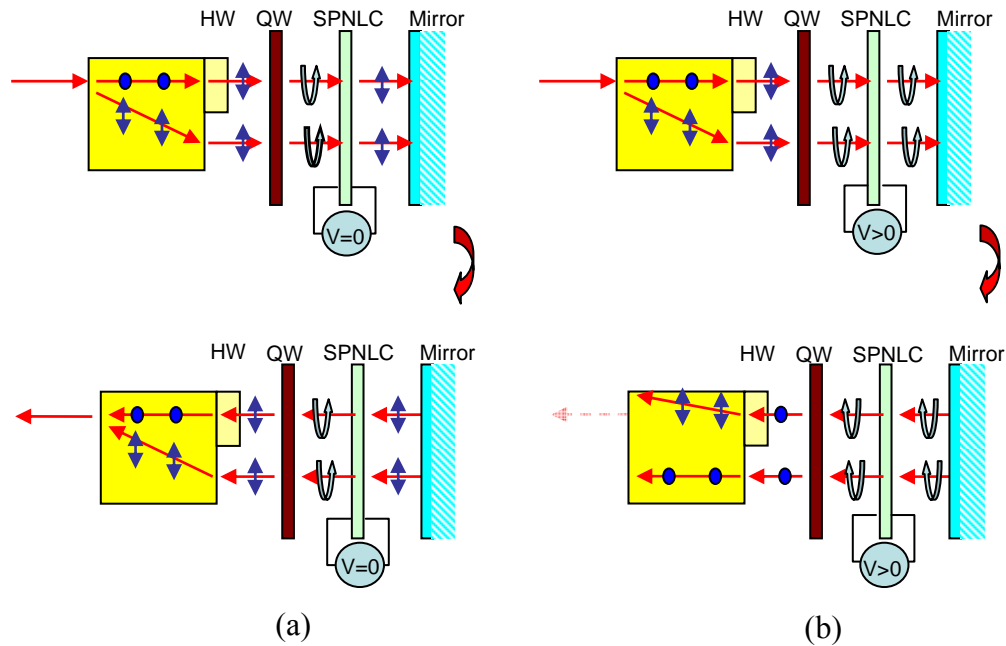


Figure 49: The detailed operation mechanisms of the phase modulator module: (a) VOA ON state,  $V=0$ , and (b) VOA OFF state,  $V=35 V_{\text{rms}}$ . HW: half-wave plate, QW: quarter-wave plate, and SPNLC: sheared polymer network liquid crystal.

In experiment, we demonstrated a SPNLC-based VOA by using an Ando AQ4321D tunable laser operated at  $\lambda=1.55 \mu\text{m}$ . The output light is captured by a detector in port 3. We acquired the detector data by a LabVIEW computer program. Figure 50 plots the voltage-dependent VOA attenuation. The VOA was addressed by 10 kHz square waves. Little attenuation is observed below  $7.5 V_{\text{rms}}$ . This threshold voltage is  $\sim 3X$  lower than that of the PNLC cell using rod-like monomers and rubbed polyimide surface alignment layers.<sup>8</sup> The observed lower threshold voltage is believed to result from the gradient tilt angle of the LC domains, as illustrated in Figure 35(b). As the applied

voltage increases, the detected reflectance decreases almost linearly. At  $V= 35 V_{\text{rms}}$ , the dynamic range reaches  $-32\text{dB}$ .

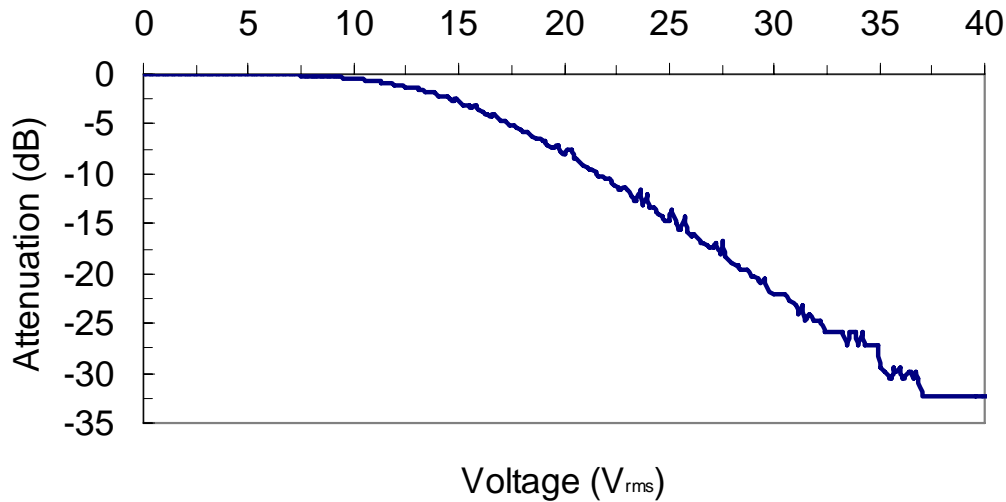


Figure 50: The VOA attenuation at different drive voltages.  $\lambda=1.55 \mu\text{m}$ .

Figure 51(a) and Figure 51(b) show the dynamic response of the SPNLC VOA. To measure the response time, a  $35 V_{\text{rms}}$  (upper traces) at  $f=10 \text{ kHz}$  square waves with 1 s duration was periodically applied to the VOA. The rise time and fall time are defined as  $10 \rightarrow 90\%$  and  $90 \rightarrow 10\%$  reflectance change, respectively. The measured optical response times are shown in the lower traces. Please note that this is a normally-on VOA. Figure 51(b) and Figure 51(a) show the optical rise and decay times, respectively. From these figures, we find the rise time is  $35 \mu\text{s}$  and decay time  $205 \mu\text{s}$ . The faster turn-on time is due to the voltage effect and the slower decay time is due to the weaker elastic restoring force. Nevertheless, the response time of our SPNLC VOA is at least one order magnitude faster than the state-of-the-art nematic competitors. Such a fast response time is contributed by two physical mechanisms: sub-micron LC domain sizes and elliptical



domain shapes. The latter is quite common for the polymer-dispersed LC droplets, especially with a shearing force. Based on the observed fast response time, we estimate that the LC domain size is around  $0.5 \mu\text{m}$ .

We also made SPNLC cells with different LC layer thicknesses. Results indicate that the response time is quite insensitive to the cell gap. This phenomenon is not surprising because the response time of a SPNLC is mainly determined by the LC domain size and shape. The cell gap does not play an important role here.

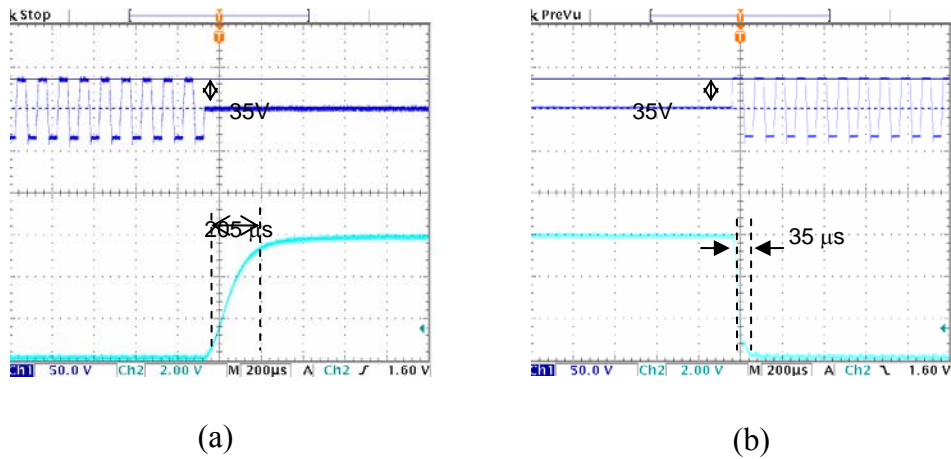


Figure 51: Optical response time of the  $9\text{-}\mu\text{m}$  SPNLC VOA: (a) decay time, and (b) rise time.

We also measured the wavelength-dependent transmittance of the SPNLC cell. In order to calibrate for the surface reflections, a homogeneous LC cell filled with E7 was used as reference. Results are shown in Figure 52. From Figure 52, the SPNLC has  $\sim 15\%$  scattering loss at  $\lambda \sim 500 \text{ nm}$ . As the wavelength increases, it becomes transparent gradually. At  $\lambda > 700 \text{ nm}$ , the transmittance is nearly the same as that of the E7 cell. In another experiment, we compared the voltage-dependent transmittance of our SPNLC cell with the homogeneous E7 cell between crossed polarizers at  $\lambda = 1.55 \mu\text{m}$ . Their

transmittance peaks are almost the same. This experiment proves that the SPNLC film is free from light scattering at  $\lambda=1.55 \mu\text{m}$ . The transmittance result shown in Figure 52 is consistent with our estimated domain size, which is  $\sim 500 \text{ nm}$ , based on the response time data.

To make the SPNLC cell suitable for active matrix direct-view or color sequential displays, we need to eliminate light scattering in the entire visible spectral region and reduce the operating voltage to  $\sim 5 V_{\text{rms}}$ . To eliminate light scattering at  $\lambda \sim 400 \text{ nm}$ , we could use a low birefringence LC mixture or slightly increase the monomer concentration in order to reduce domain sizes. Increasing monomer concentration would increase the operating voltage. Thus, using a low birefringence LC mixture is more feasible. However, the detailed two-step UV curing processes remain to be optimized. To reduce operating voltage, we could use a thinner cell gap or use a LC mixture with a lower threshold voltage.

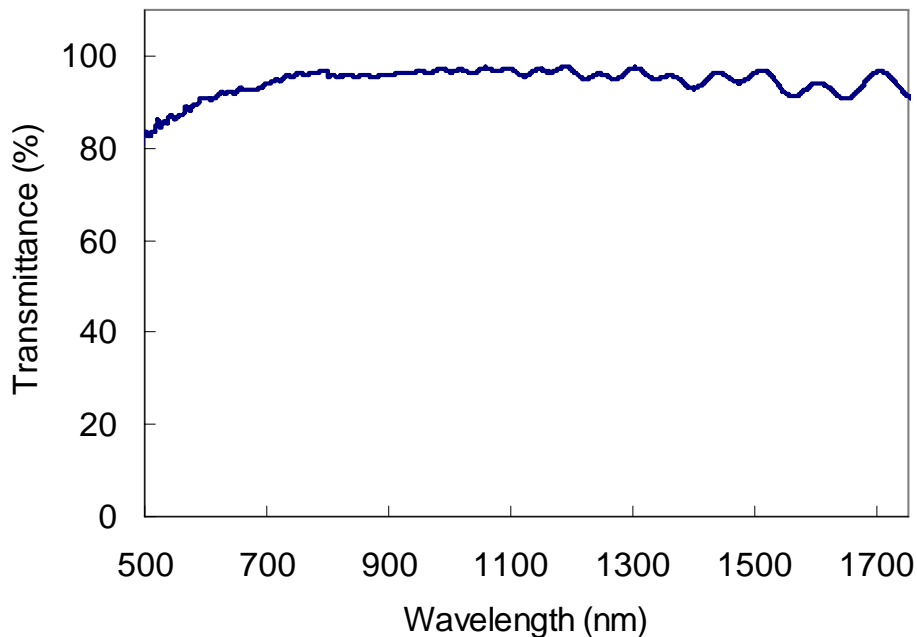


Figure 52: Wavelength-dependent transmittance of the E7 SPNLC cell.  $d \sim 9 \mu\text{m}$ .

For fiber-optic applications, it is highly desirable that a VOA has a broad bandwidth over the whole spectral range defined by the International Telecommunication Union (ITU). To investigate the wavelength dependency, an ANDO ASE light source ( $\lambda=1525\text{-}1575 \text{ nm}$ ) and an optical spectrum analyzer were used. Figure 53 shows the wavelength-dependent attenuations of the SPNLC VOA. The attenuation variations from wavelength 1530 to 1570 nm was measured at 0, 5, 10, 15, 20, 25 and 30 dB, respectively. Based on the results, the attenuation of our VOA is rather insensitive to wavelength over the ITU C-band. In addition, the polarization-dependent-loss (PDL) stays at around  $-0.2 \text{ dB}$  over this spectral range. The insertion loss of the SPNLC cell is around  $-2\text{dB}$  due to the quadruple passes of the uncoated glass substrates. To reduce this insertion loss, anti-reflection coating of the LC cell should be considered. Moreover, in order to avoid the circulator loss, a dual fiber collimator can be employed as well.

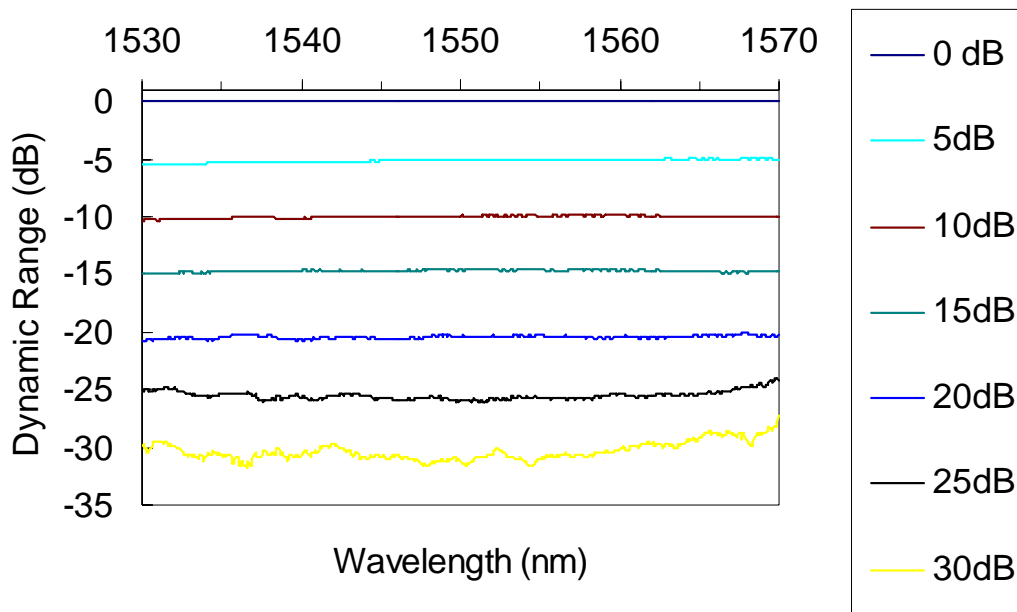


Figure 53: The wavelength-dependent attenuations of the VOA at different attenuation range.

The device depicted in Figure 49 is in a normally-on mode. However, a normally-off VOA is also needed in dynamic optical networks for some special demands such as channel blocking and system protection. To achieve a normally-off mode, we could remove the QWP shown in Figure 49. Since the SPNLC cell has a phase retardation  $\delta=\pi/2$  at  $\lambda=1.55 \mu\text{m}$ , the total phase retardation of the output beams is  $\pi$  after passing the modulator module twice. Therefore, the polarization states of the two retro-beams from LC cell remain linearly polarized but their axes are rotated by  $90^\circ$ . The return paths of these beams in the PBD are deviated from those of the incident beams and no light is coupled into the collimator. The VOA is normally-off at  $V=0$ . As the applied voltage increases, the transmittance increases.

## **6.7 Conclusions**

We have demonstrated a reflective-mode VOA with  $\sim 0.24$  ms response time at room temperature ( $\sim 21^\circ\text{C}$ ) and -32 dB dynamic range using a sheared polymer-network liquid crystal. Such a VOA exhibits no light scattering at  $\lambda=1.55 \mu\text{m}$ . Its application for high speed optical networks is foreseeable.

## **CHAPTER 7: AXIALLY SYMMETRY SHEARED POLYMER NETWORK LIQUID CRYSTALS**

### **7.1 Introduction**

An axially-symmetric liquid crystal (LC) structure can be used as a wavelength selection Fabry-Perot filter and a spatial polarization converter. A particularly attractive feature of the axially-symmetric LC structure is its polarization independence because the LC directors are oriented symmetrically in the radial directions. Therefore, we can use it as an optical device which is insensitive to the polarization change<sup>12</sup>. Besides, there is an emerging interest in developing the space-variant polarized light with axial symmetry<sup>13,14,15</sup>. Several approaches for achieving this kind of spatial polarization characteristic have been explored. One approach uses the interference of two linearly polarized beams<sup>16</sup>. The major shortcoming of this method is the relatively low light efficiency and complicated fabrication process. Others use special LC cells with circularly rubbing<sup>13,14</sup> or subwavelength gratings<sup>15</sup> to realize the radially or azimuthally polarized light. However, these approaches require a complicated fabrication procedure such as circular rubbing or micro-fabrication process.

In this chapter, we report a new axially-symmetric sheared polymer network liquid crystal (SPNLC). This structure has attractive features such as fast response time and polarization independence. Through analyzing the structure of this axially-symmetric SPNLC, we constructed a 3-dimensional model to explain the observed phenomena. The simulation results agree well with the experiment. The axially-symmetric SPNLC can be

used as a tunable-focus negative lens and a spatial polarization converter. Moreover, we also develop a new method for simultaneous detection of phase retardation and optical axis of a phase compensation film using an axially-symmetric SPNLC.

## **7.2 Sample preparation**

To prepare an axially-symmetric PNLC cell, we mixed 15 wt % of a photopolymerizable monomer (Norland optical adhesive NOA65) in a commercial Merck E7 LC mixture. The mixed LC and monomer was filled in two ITO (indium-tin-oxide) glass substrates with the cell gap  $d \sim 9 \mu\text{m}$ . In order to polymerize the LC cell, a two-step UV curing process was adopted<sup>7,8</sup>. After UV curing, we applied an off-axis shearing force to the top substrate while keeping the bottom glass substrate fixed. This shearing force stretches the entangled polymer networks and suppresses the light scattering completely<sup>7,8</sup>. If the shearing torque is large enough, the polymer networks begin to contract and form an axially-symmetric pattern owing to the restoring force. The axially-symmetric sheared PNLC cell is transparent after shearing process. For example, Figure 54 shows the off axis shearing of the glass substrates. The applied shearing force is not in the axis of the center of the bottom substrates fixed by the stop. The extra torque results in the contraction of the polymer network and forms the axially symmetric structure of the liquid crystal molecules. To control the radial SPNLC patterns, we employed a precise motor motion system (Newport ESP-300) to control the initial acceleration, shearing speed, deceleration, and total shearing distance. The shearing conditions are listed as follows: acceleration =  $10 \text{ mm/s}^2$ , speed =  $2.5 \text{ mm/s}$ , deceleration =  $-10 \text{ mm/s}^2$ , and shearing distance  $\sim 150 \mu\text{m}$ . To prevent the sheared LC directors from

relaxing back, the peripherals of the cell were sealed by a UV adhesive. All our measurements were performed using the sealed LC cell. No noticeable performance change was detected before and after the sealing.

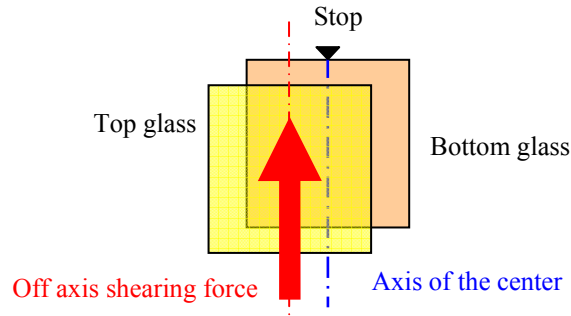


Figure 54: The illustration of the off-axis shearing of the SPNLC cell

Figure 55 shows the primitive structure of the axially symmetric SPNLC. After the shearing process, the LC directors align toward the center of the pattern. Polymer network forms a radial structure and constrains the LC directors within a circle. The screen shows the image of the axially symmetric SPNLC structure under the crossed polarizers. The black cross is caused by the passing light whose polarization direction is perpendicular to the transmittance axis of the polarizer or analyzer. In order to verify the axially symmetric properties of the SPNLC structure, we rotated the polarizer/analyzer pairs from  $0^\circ$  to  $360^\circ$  while keeping them crossed. In principle, we could fix the polarizer and analyzer but rotate the sample. The former method is preferred because it keeps the laser beam at the same spot of the sample. Experimental error due to nonuniformity of the sample can thus be ruled out. The experimental results show that the crossed-hair patterns rotate in correspondence of the polarizer/analyzer rotation. The output is identical,

independent of the rotation angle of the incident light polarization. This observation confirms that the LC directors indeed are axially symmetric.

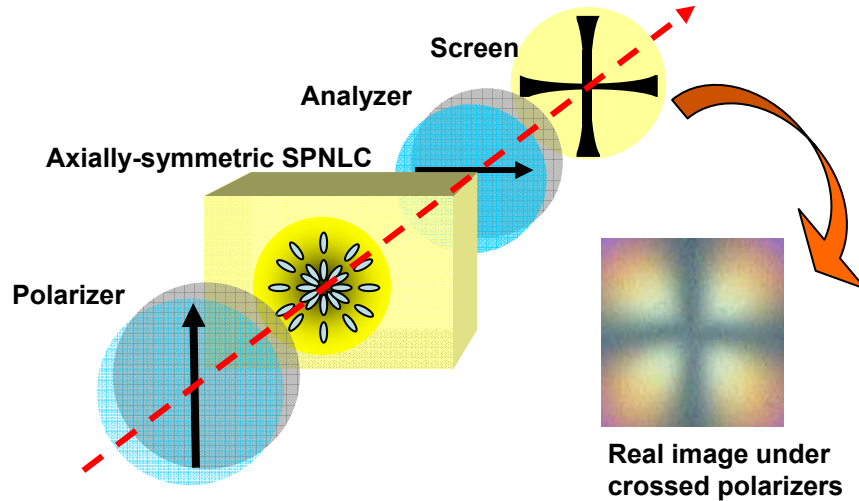


Figure 55: SPNLC structure observed under crossed polarizers.

### **7.3 Properties of axially sheared polymer network liquid crystals**

#### **7.3.1 Polarization independence**

Figure 56 shows the polarization independence of the axially-symmetric SPNLC structure to the linearly polarized light in the azimuthal angles. To verify the polarization independence, we measure the voltage-dependent transmittance curves (V-T curve) under three different rotation angles of the crossed polarizers. The input light ( $\lambda=632.8$  nm) was expanded and collimated to 10 mm to cover the central portion of the LC sample. The diameter of the whole sample is  $\sim 20$  mm. The reason we narrow down the aperture size



to 10 mm is because the central part has better LC alignment and less defects. The V-T curves were measured at three polarizer angles:  $0^\circ$ ,  $45^\circ$ , and  $90^\circ$ . The analyzer is always crossed to the polarizer. As shown in Figure 56, the three V-T curves overlap very well. That means the LC directors are distributed in radial directions, as sketched in Figure 55.

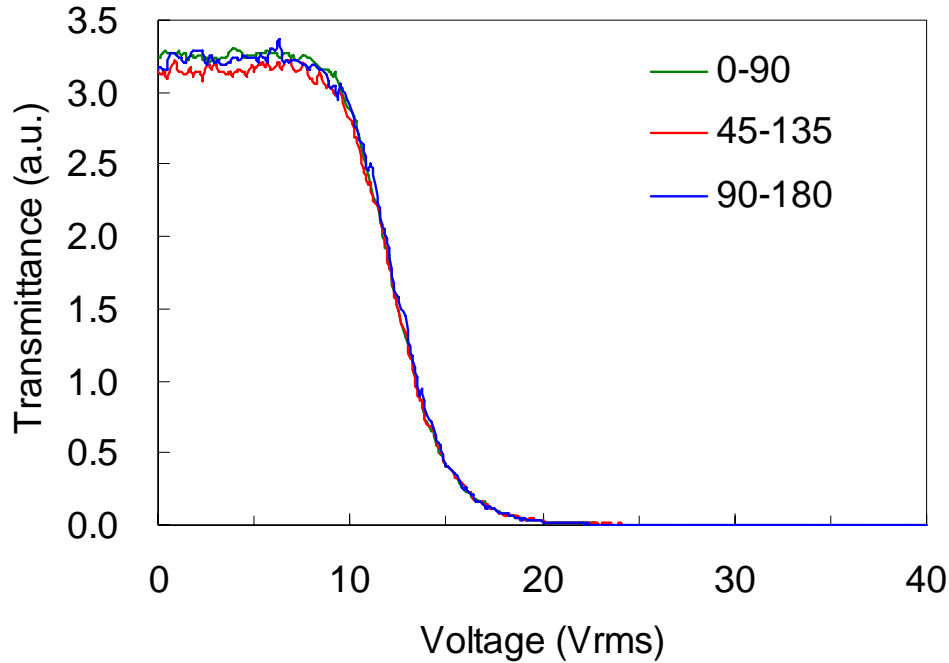


Figure 56: Voltage-dependent transmittance of the axially symmetric SPNLC cell.  $d=9 \mu\text{m}$  and  $\lambda=633 \text{ nm}$ .

### 7.3.2 Fast response time

Figure 57(a) and (b) show the measured response time of the axially-symmetric SPNLC. To measure the response time, we applied a  $20 \text{ V}_{\text{rms}}$  at  $f=1 \text{ kHz}$  square waves to the LC cell. The rise time and decay time are defined from  $90 \rightarrow 10 \%$  and  $10 \rightarrow 90 \%$  transmittance change, respectively. The measured optical response times are recorded in

the lower traces. From Figure 57(a) and (b), the measured rise time is 0.6 ms and decay time 1.8 ms. From previous studies<sup>7,8</sup>, SPNLC exhibit a fast response time because of the small LC domain sizes and, moreover, the response time is insensitive to the cell gap. Thus, we can use a thick cell gap to gain phase change while still keeping a fast response time. The tradeoff of using a thick LC layer is the increased voltage.

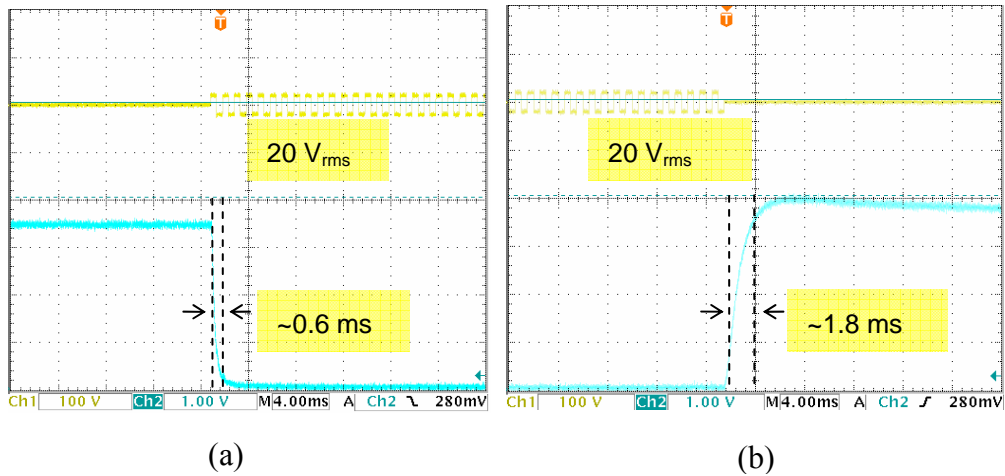


Figure 57: Optical response time of the 9- $\mu\text{m}$  axially-symmetric SPNLC: (a) rise time, and (b) decay time.

### 7.3.3 Gradient phase retardation distribution

To understand the detailed structure of the axially-symmetric SPNLC, we analyze the phase difference at different positions of the pattern. Figure 58(a) shows the top view and cross-section of the structure. The diameter of the pattern is  $\sim 20$  mm. We measured the phase retardation from the center to the edge of the ring at  $V=0$ . Figure 58 (b) shows the gradient distribution of the phase retardation from the center to the outer ring of the

SPNLC structure. The phase difference increases from 0 at center to 450 nm at the edge of the pattern. The different phase retardation in each position at  $V=0$  represents the different LC alignment in the initial state. The larger phase retardation implies the lower pretilt angle. Based on the simulation results, the average pretilt angle is larger than  $60^\circ$ .

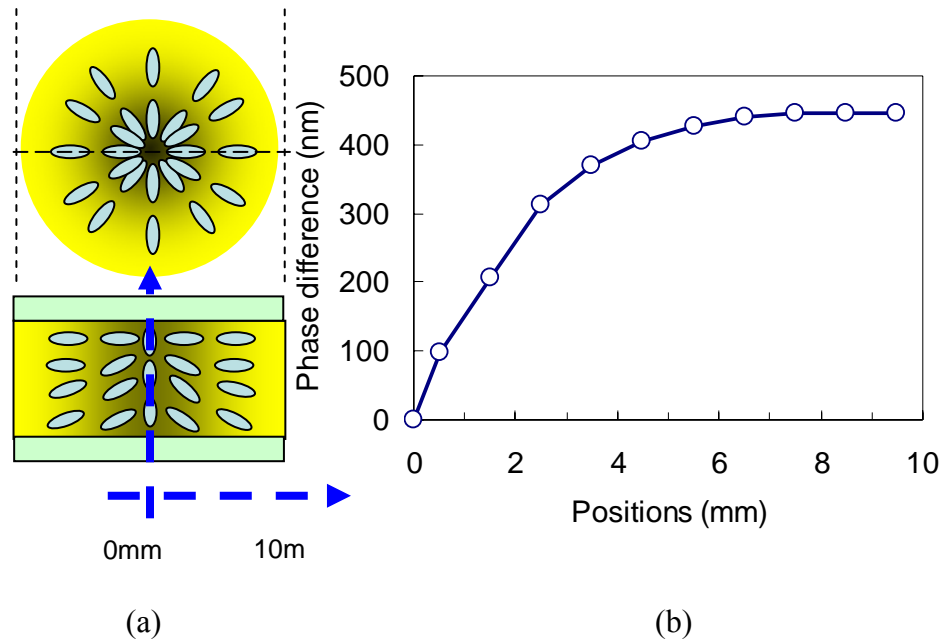


Figure 58: (a) Top view and cross-section of the LC structure; (b) Measured gradient distribution of the phase retardation.

Figure 59 shows the simulated LC tilt angle distribution. At center, the tilt angle is nearly  $90^\circ$ . That means the LC directors are nearly perpendicular to the substrates. This explains why the central spot always appears dark under crossed polarizers. As the radial distance increases, the tilt angle gradually decreases. At each position of the cross-section, the LC directors possess a hybrid structure, i.e., the LC near the top and bottom substrates

have different tilt angles. The relatively large tilt angle helps to lower the threshold voltage and the dark state voltage, but the tradeoff is the reduced phase retardation.

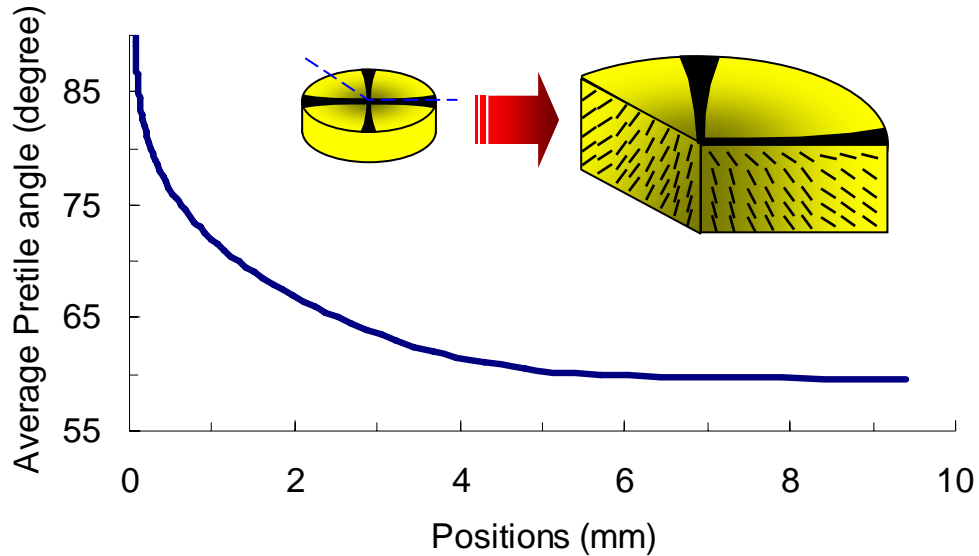


Figure 59: Simulated pretilt angle distribution of the axially-symmetric SPNLC cell.

Figure 60 plots the measured V-T curves at different radial positions in the pattern. The high driving voltage implies the LC directors are tightly anchored by the polymer networks. It also implies the large elastic constant for the axially-symmetric SPNLC structure. Besides, we should also consider the weak surface boundary condition because there is no surface treatment on the glass substrates. The different transmittance of the V-T curve at the initial point represent the different alignment structure at  $V=0$ . The higher transmittance means the larger phase retardation. The phase retardation decreases as the position moves toward the center of the pattern.

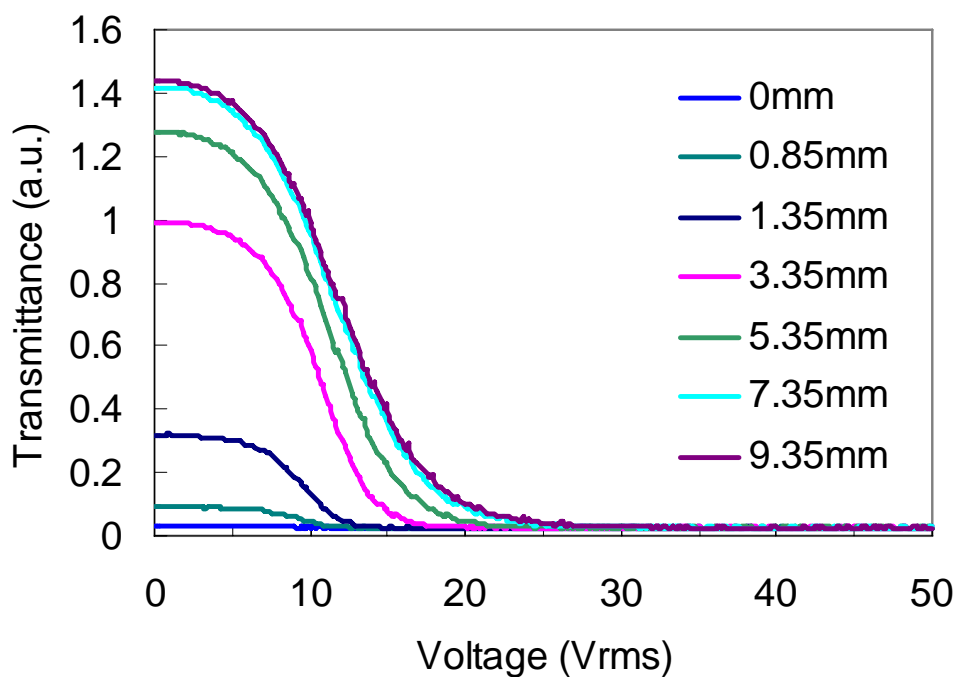


Figure 60: Measured V-T curves at different positions of the axially-symmetric SPNLC cell.

From Figure 60, the axially-symmetric SPNLC has a lower threshold voltage than PNLC. This is because the axially-symmetric SPNLC has hybrid LC alignment in each cross-section and the increased tilt angle smears the threshold behavior and lowers the dark state (between crossed polarizers) voltage. On the other hand, a PNLC cell has surface alignment and the employed polymer is quite rigid. The small polymer network domains significantly reduce the response time, but the tradeoffs are the increased threshold and operating voltages<sup>8</sup>.

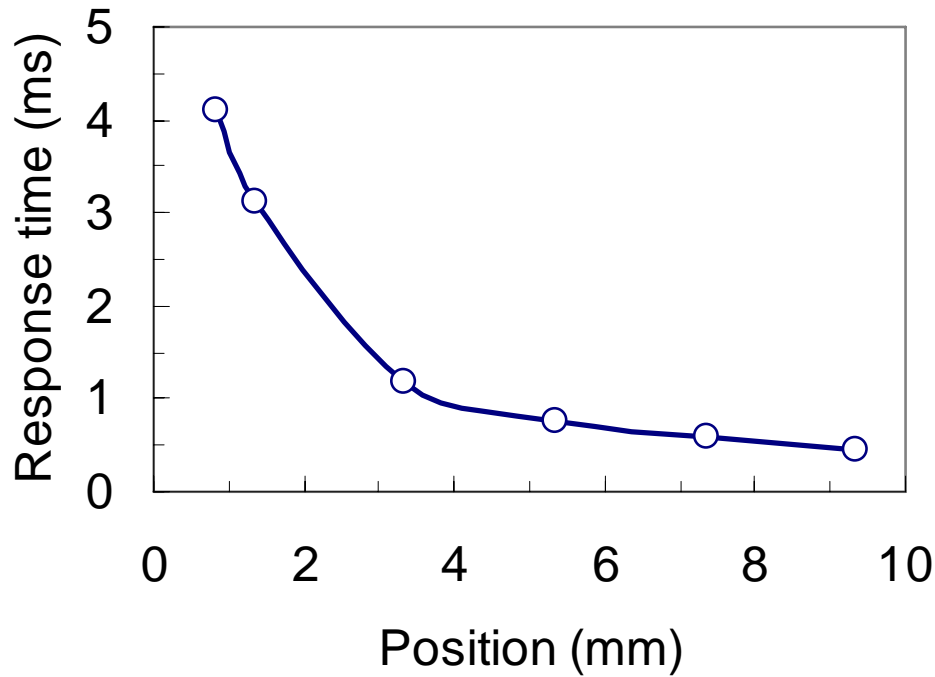


Figure 61: Measured response time at different positions of the axially-symmetric SPNLC cell.

Figure 61 plots the measured response time at different positions of the axially symmetric SPNLC. Since the LC tilt angle varies spatially, to reduce experimental error we should keep the laser spot size as small as possible. In our lab, we have a  $1.55 \mu\text{m}$  laser whose beam diameter is less than 1 mm. Therefore, we used this laser for the response time measurements. From Figure 61, the measured response time is slower near the center of the pattern than at the edge. Two reasons contribute to the slower response time observed in the central portion. First, the LC directors near the central section have less restoring force than those in the edge because of the high tilt angles. Second, the central LC directors are bounded by weaker polymer networks which produce a smaller restoring torque than the border.

### 7.3.4 AS-SPNLC properties in different diameter

In this section, we describe the optical properties of the AS-SPNLC with different diameter. As we mention in the previous section, the AS-SPNLC has a diameter around 5~10 mm. In the diameter changes, the properties of the average phase and response time will change as well. Figure 62 shows the experimental setup for measuring the AS-SPNLC properties. A He-Ne laser beam was expanded and collimated to a desired size. The AS-SPNLC sample was placed between two crossed polarizers. A LabView data acquisition system was used to collect data and provide voltage to the cell.

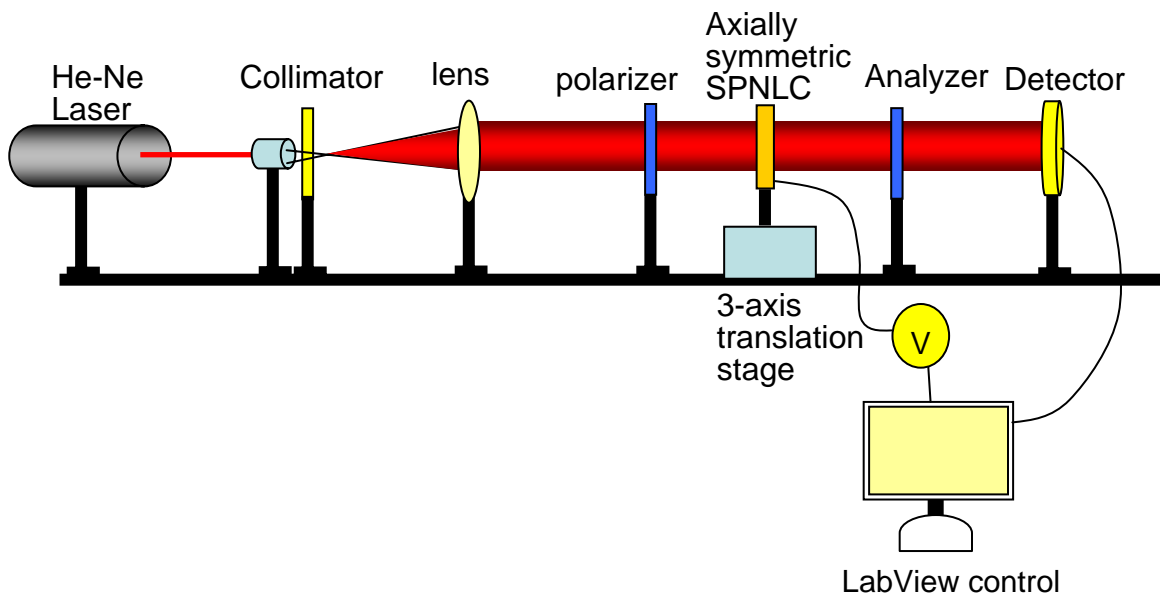


Figure 62: Experimental setup for measuring the AS-SPNLC properties in different diameter

Figure 63 defines the measured size of the SPNLC. In Figure 63, we observed two concentric rings with a black crisscross in the middle under the crossed polarizer. Each ring represents a  $2\pi$  phase difference to the nearby one. The phase is zero in the center

and increases toward the edge of the ring. We define three measured sizes within the AS-SPNLC structure. Their diameters are 2 mm, 6 mm and 10 mm as regions I, II and III, respectively.

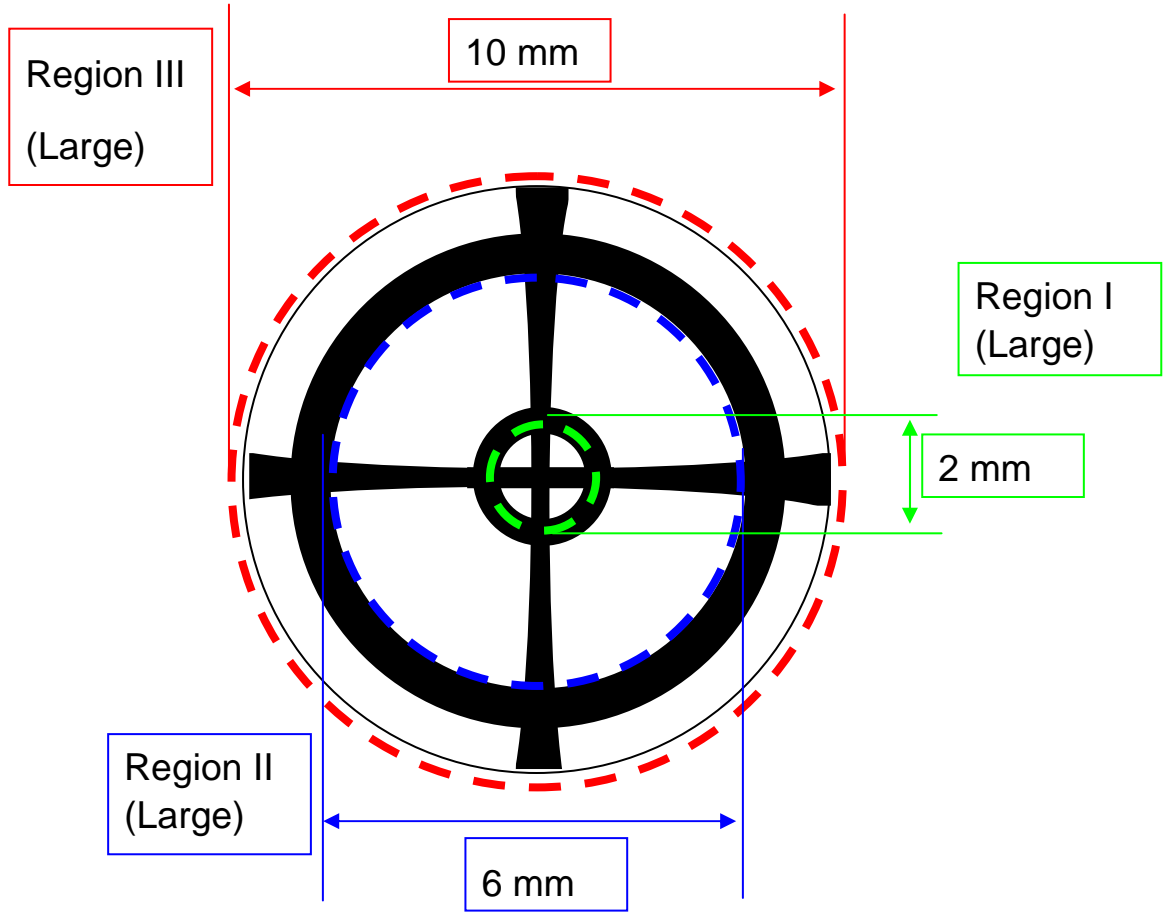


Figure 63: Diameter definitions of the axially symmetric SPNLC structure

Table 2 shows the measured results for the response time and phase changes in each region. Based on Table 2, the average phase change is around  $1.9 \pi$ . However, the response times are different in each region. Region II has the fastest response time among the three regions studied. In general, the larger area should have a faster average response time than the smaller region. This is because the larger one has faster switching LC areas



than the smaller one. Figure 61 also shows the response time trend. The inner circle of the LC directors shows slower response time than the outer circle. Hence, region II is faster than region I. However, region III does not agree with this trend. It is slower than region II even though the measured area is bigger than region II. After analyzing the data, it may happen because the outer ring of the AS-SPNLC is too close to the AS-SPNLC boundary, which contains many gray areas between AS-SPNLC and the normal LC areas with polymer network. Therefore, the average response time is slower than region II. This measurement helps us to understand the relationship between the response time and the size of the AS-SPNLC. These results play an important role for making the photonic devices using AS-SPNLC.

Table 2: Response time results of AS-SPNLC properties in different diameter

	Driving voltage	Total phase	Rise time	Decay time	Total time
Region I (Small)	0-100V	$1.90 \pi$	0.3ms	6ms	6.3ms
Region II (Medium)	0-100V	$1.86 \pi$	0.5ms	2ms	2.5ms
Region III (Large)	0-120V	$1.88 \pi$	0.2ms	5ms	5.2ms

### 7.3.5 Physics model of the AS-SPNLC

To understand the formation mechanism of AS-SPNLC, we propose a physical model based on the experimental results and validate the model by computer simulation. First, within the AS-SPNLC region, the polymer network is very strong. Compared to the

LC model we mentioned in Chapter 2, the elastic constants (K values) should be at least 10 to 100 times larger. Figure 64 shows the simulation results of the elastic constant v.s. voltage-dependent transmittance (VT) curve. As the elastic constants increase from 10 to 600 times, the VT-curve shifts to the higher voltage region (right side). It takes stronger electric force to drive the liquid crystals because of the stronger polymer network. Figure 65 shows the elastic constants v.s. LC response curve. As elastic constants increase from 10 to 600 times, the response time curve becomes steeper. In other words, the response time of the LC becomes faster because of the stronger restoring force of the polymer network.

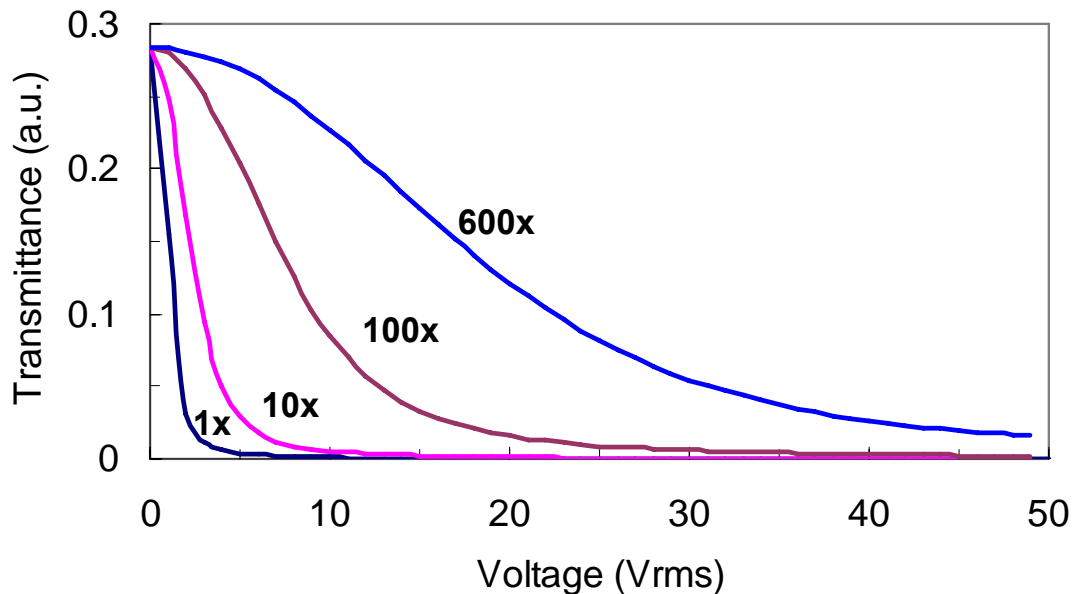


Figure 64: The simulation results of the elastic constant v.s. voltage-dependent transmittance (VT) curve as the elastic constants increase from 10 to 600 times

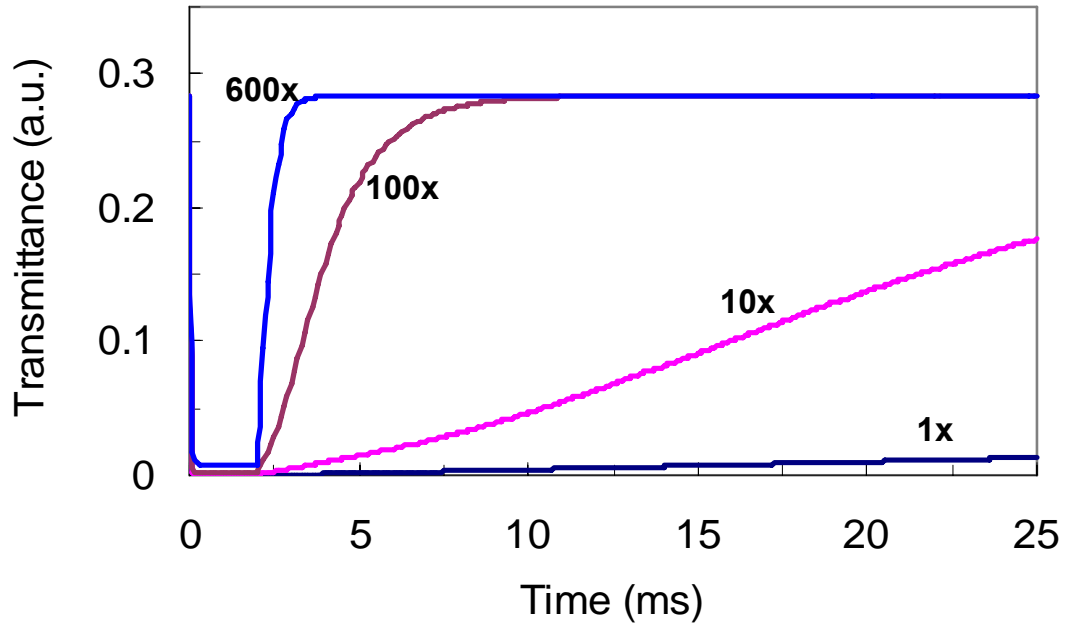


Figure 65: Elastic constants v.s. LC response time curve

Second, Figure 61 shows the response time with respect to the radius. The polymer network far away from the center has a faster response time. We propose that there are different distributions of the polymer network strength from the center to the outer ring of the SPNLC. Hence, the effective elastic constants ( $K$  values) increase with the radius.

Third, since there is no rubbing treatment on the surface of the SPNLC, the physical model should include the weak anchoring surface effect. Therefore, the operating voltage ( $V_{op}$ ) should be smaller than the modes which consider a hard boundary effect. Moreover, the dark state with a weaker surface effect should be better. To determine the anchoring surface effect, a surface anchoring energy  $W_s$  is defined as eq. (10), where  $\lambda_0$  is a surface anchoring factor.

$$W_s = \frac{\pi \cdot K_1}{2 \cdot \lambda_0 \cdot d} \sin^2(2 \cdot \alpha) \quad (10)$$

The weak surface anchoring effect means the lower surface anchoring energy  $W_s$ . The surface anchoring energy  $W_s$  decrease as the surface anchoring factor  $\lambda_0$  increases. Figure 66 shows the VT-curve with different weak surface anchoring factors. As the  $\lambda_0$  increases, the operating voltage ( $V_{op}$ ) drops and the slope of V-T curve become steeper. In other word, the weak surface anchoring effect results in the lower operating voltage ( $V_{op}$ ) and the VT-curve shifts to the lower voltage side.

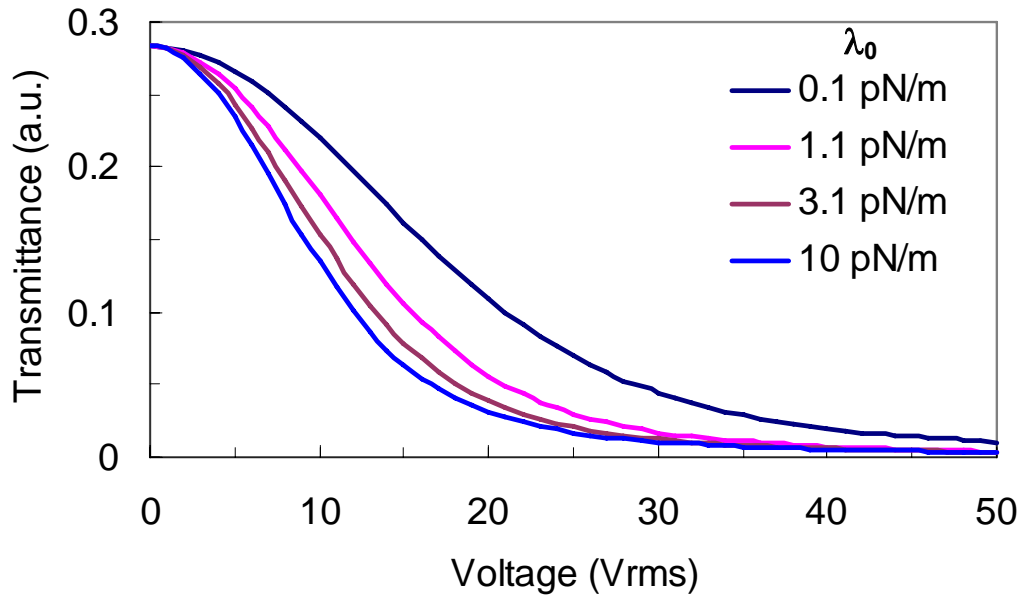


Figure 66: VT-curves of different weak surface anchoring factors

Fourth, the average pretilt angle decreases with radius. Figure 59 shows the simulation result of the pretilt angle distributions. In Figure 70, we will discuss the formation analysis of this gradient distribution of the liquid crystal directors.

Figure 67 shows the simulation and experimental results of the VT-curve based on the physical model we described above. The fitting parameters are  $K_{11}=35000$  pN,  $K_{33}=1000$  pN and  $K_{11}/K_{33}=35$ . The large  $K_{11}$  and  $K_{33}$  result from the extra shearing force. The simulation results agree with experiment reasonably well.

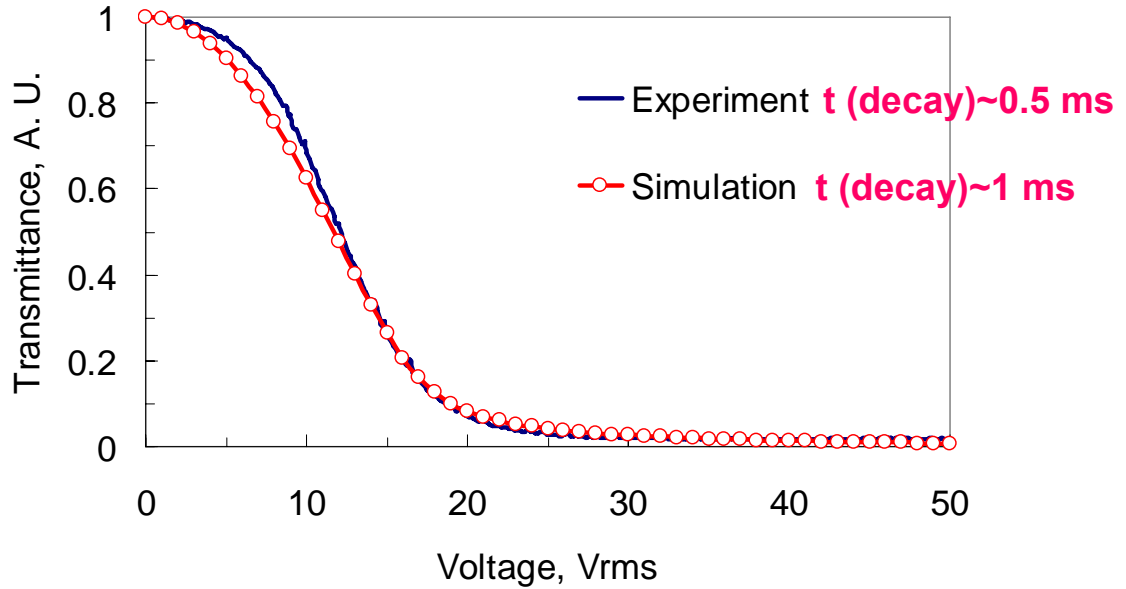


Figure 67: Simulation and experimental results of the AS-SPNLC

### 7.3.6 Simulation of axially sheared polymer network liquid crystals

Figure 68(a) is a series of pictures showing the experimentally observed dynamic image when a voltage is applied to the AS-SPNLC. Based on the measured birefringence, V-T curve, and response time at different radial positions of the structure, we construct a 3-dimensional model of the LC directors and simulate the dynamic response under crossed polarizers. Figure 68(b) shows the simulated results of the dynamic change when a voltage is applied. The simulation results agree quite well with experiment.

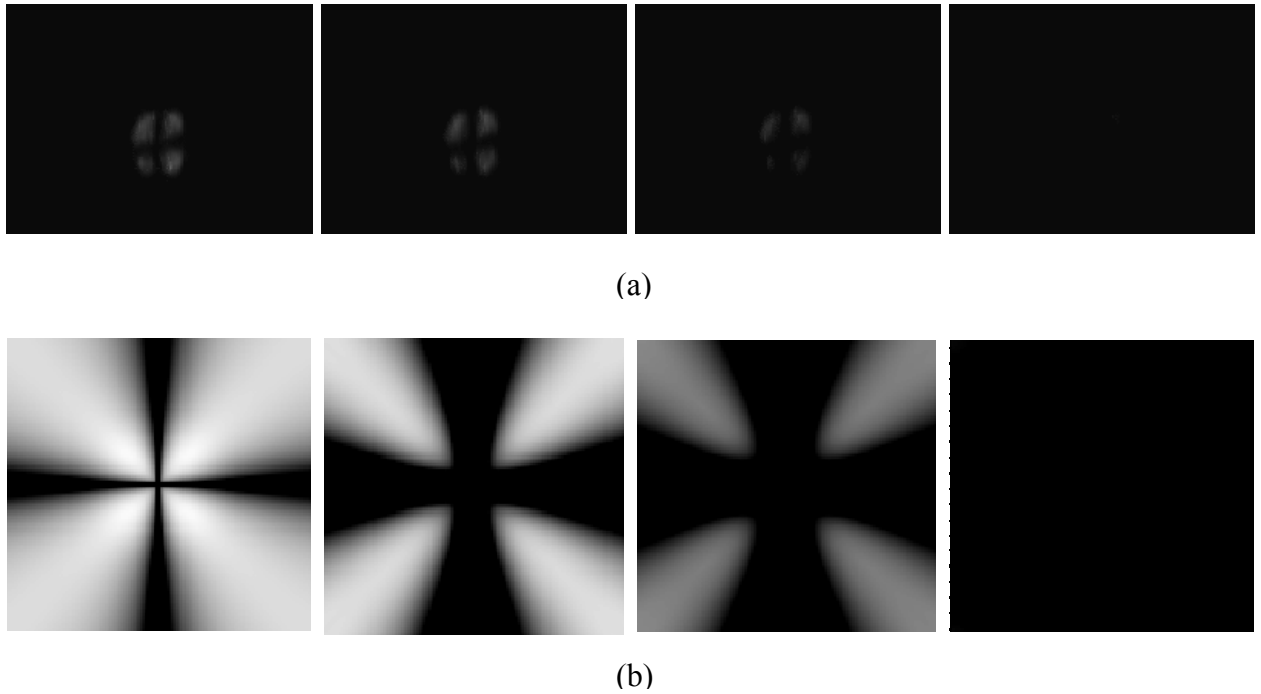


Figure 68: (a) Experimental results when a voltage is applied to the AS-SPNLC, and (b) simulated results.

#### **7.4 Formation analysis of the axially sheared polymer network liquid crystals**

To understand the pattern formation of the AS-SPNLC, we use a vertical alignment (VA) SPNLC cell as an example. Compared to the non-rubbing sample with scattering conditions, the VA SPNLC is easier to investigate the formation process. In order to enhance the formation phenomena of the AS-SPNLC, we fabricated the VA SPNLC by a quick UV exposure (~15 sec). After UV curing process, the VA cell is scattering-free and looks quite transparent. When viewed between crossed polarizers at  $V_{\text{rms}}=0$ , the cell appears black. This is because of the good vertical alignment of the liquid crystal cell. To observe the AS-SPNLC formation in situ, we applied a shearing force to

the top glass substrate while keeping the bottom one fixed. Figure 69(a) shows the AS-SPNLC formation while slightly pushing the lower position of the top glass substrate. Under the cross polarizer, we observed several concentric rings with a black cross bar in the middle. Each ring represents a  $2\pi$  phase difference to the adjacent one. The more rings means the larger phase difference between the center and the outmost edge. The black cross bar is caused by the traversed light whose polarization direction is perpendicular to the transmission axis of the polarizer or the analyzer.

Figure 69(a)-(f) show a sequential pattern change VA SPNLC cell before and after pushing the top glass substrate. The number of the rings increases when we push the glass substrate. The increment of the rings implies that more and more liquid crystal molecules tilt away from the vertical alignment because of the external shearing force. The larger tilt angle means the shearing force is stronger and the produced phase difference is larger. The pattern shows the gradient distribution of the phase retardation from the center to the outer ring of the SPNLC structure. The different phase retardation in each position at  $V_{rms}=0$  represents the different LC alignment in the initial state. The larger phase retardation implies a smaller pretilt angle, defined between the optic axis of the LC director and the horizontal direction. After releasing the shearing force of the top glass substrate, the AS-SPNLC relaxes back to the homeotropic state so that the phase difference around the pattern vanishes and the rings disappears. To summarize our experimental observation, we saw the liquid crystal directors tilt down from outside to center and relax back to the vertical alignment.

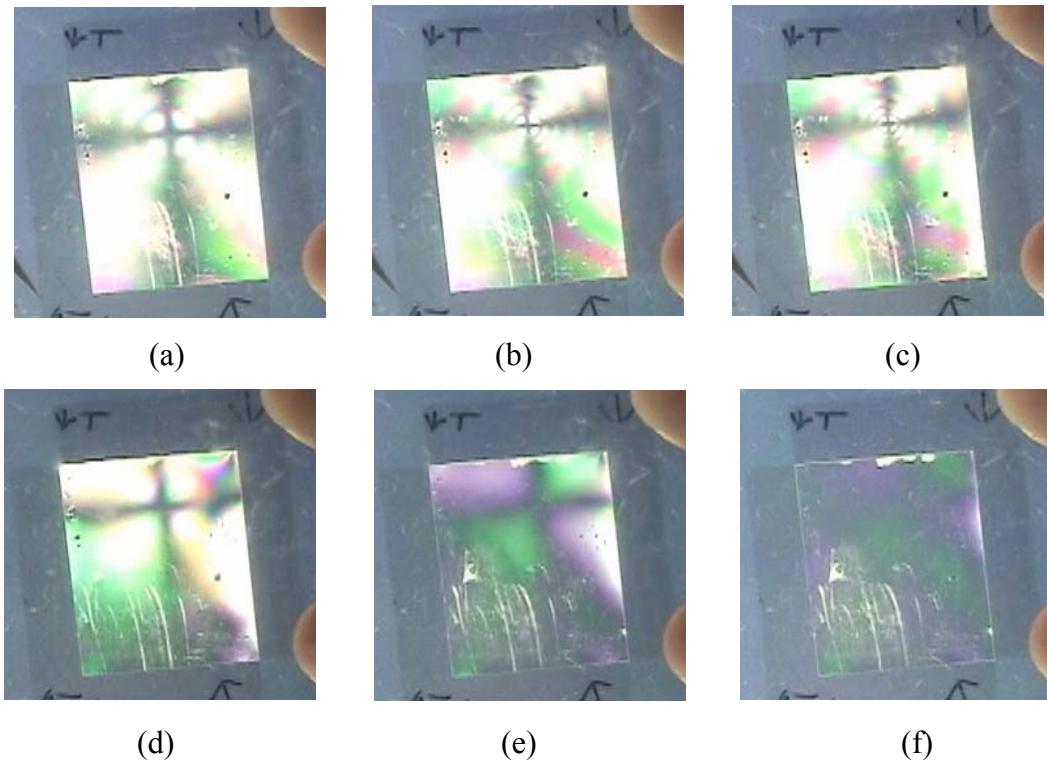


Figure 69: (a)-(f) A sequential change of the pattern while pushing the top glass substrate.

Figure 70 shows the illustration of external force and the movement of the liquid crystal directors. Based on the observation, the liquid crystal molecules receive the external forces from outside toward the center. Hence, the alignment of the liquid crystal molecules is axially symmetric. Figure 70 (a) shows the cross-section of the LC director distribution from side view. The gradient force distributes from the top to the bottom of the glass substrate. The liquid crystal directors near the top substrate receive a stronger external force causing a smaller pretilt angle. In contrast, the bottom part receives a weaker force causing a larger pretilt angle. Thus, it forms a hybrid structure, meaning the pretilt angle gradually increases from the top to the bottom glass substrate. Figure 70(b) illustrates the LC director's redistribution after the shearing force is released. The



AS-SPNLC relaxes back to the homeotropic state due to the intrinsic elastic force of the liquid crystal directors.

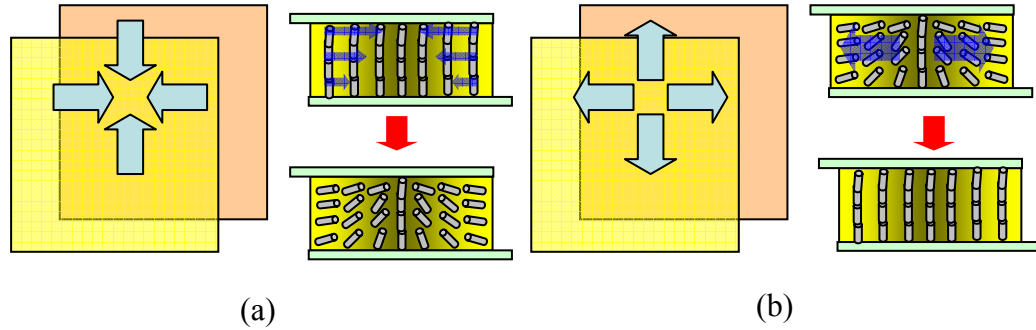


Figure 70: Illustration of external force and movement of the liquid crystal directors (a) initial state, and (b) relaxed state

The external force causes the distortion of AS-SPNLC cell. Figure 71 shows an example of the bulk distortion. The surface of the bulk is warped by this external force. To simplify the model, we consider AS-SPNLC as a bulk with elasticity. The top substrate exerts torsion to the bulk molecules when we apply a tangential force to the cell. Figure 72 shows the top view and side view of the distortion. The top glass substrate slightly rotates if we apply an off-axis force. Then, the AS-SPNLC will be distorted while the bottom glass substrate is fixed. A normal stress to the surface is generated while the bulk is distorted. This normal stress has a gradient distribution from the top to the bottom and toward the center. Therefore, the liquid crystal directors are reoriented inside the bulk and followed the direction of this external force.

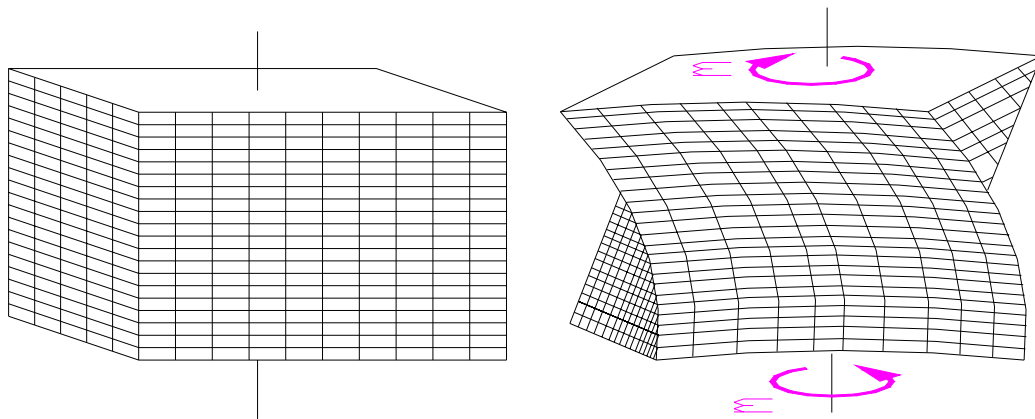


Figure 71: An example of the bulk distortion.

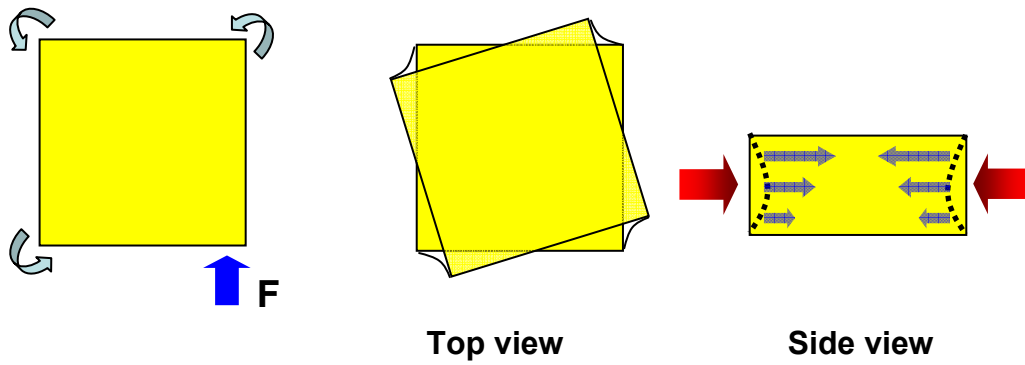


Figure 72: Top view and side view of the cell distortion.

## **7.5 Phase retardation measurement methods using AS-SPNLC**

### **7.5.1 Introduction**

Phase compensation films have been commonly used for improving the viewing angle and contrast ratio of liquid crystal display devices. For a compensation film, the refractive indices and optic axis need to be specified. Several methods, such as Soleil-Babinet compensator and photoelastic modulator, have been developed for measuring the phase retardation value of a phase compensation film.<sup>18,19,20,21,22</sup> Figure 73 shows Soleil-Babinet compensator measurement method. This compensator is a mechanically adjustable retardation plate using two crystal wedges. The latter one, photoelastic modulator, is an electrically controllable compensator. This measurement method is also called “Photoelastic modulator (PEM) method”. The PEM consists of a photoelastic material whose birefringence changes as the electric field is applied. By analyzing the modulated signal from photoelastic modulators, we can determine the phase retardation information. Figure 74 shows the PEM compensator measurement method. After applying a signal to the PEM, we can obtain the birefringence by analyzing the output of the Lock-in amplifier. The advantage of this method is the high accuracy for small birefringence measurement. However, the experiment setup is expensive and complicated. The major shortcoming of these methods is that they cannot determine the retardation and optic axis simultaneously.

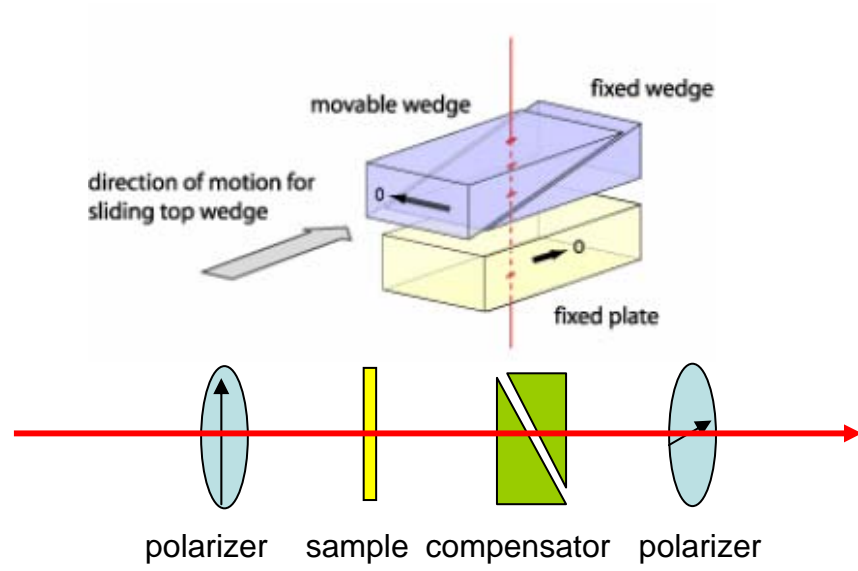


Figure 73: Soleil-Babinet compensator measurement method

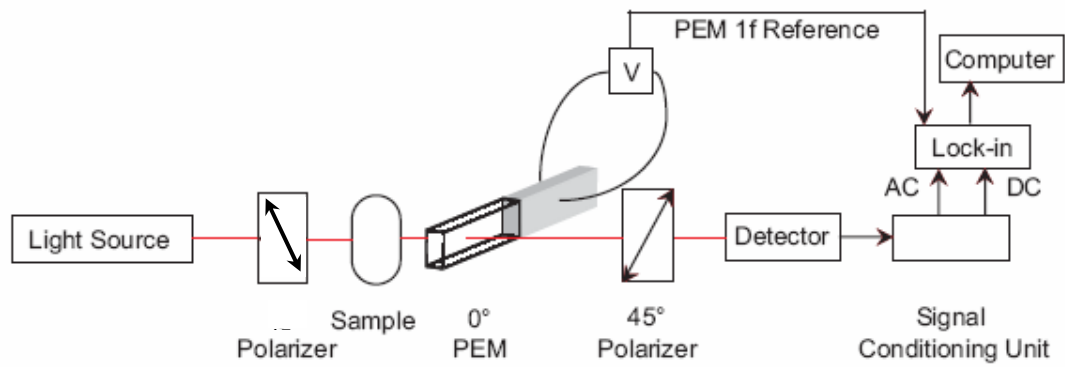


Figure 74: PEM compensator measurement method

In this chapter, we develop a new method for simultaneous detection of phase retardation and optical axis of a phase compensation film using an axially-symmetric Sheared Polymer Network Liquid Crystal (SPNLC).<sup>17,23</sup> The axially-symmetric SPNLC

exhibits two unique features: 1) its optical axis is radial in all directions, and 2) its phase retardation has a gradient distribution from center to edges. In experiment, we first characterize the phase retardation profile of our axially-symmetric SPNLC film. Then we overlay a phase compensation film, whose retardation value and optical axis is yet to be determined, on top of our SPNLC film. The transmitted image between crossed polarizers is recorded by a CCD camera. After analyzing the compensation pattern of the CCD image, we can precisely identify the phase retardation value and optical axis of the tested phase compensation film. To demonstrate this powerful technique, we use a quarter-wave plate with an arbitrary axis as an example to illustrate the measurement principles. Excellent agreement between experiment and simulation is obtained. This new method is particularly useful for those optical systems whose optical axis and phase retardation are dynamically changing.

### 7.5.2 Measurement methods

To measure the phase retardation,  $d\Delta n(\lambda)$ , of the sample, we first characterize the phase retardation profile of our axially-symmetric SPNLC film. Figure 75 shows the gradient distribution of the phase retardation from the center to the outer ring of the SPNLC cell at  $\lambda=656$  nm and 532 nm. The phase retardation increases from 0 at center to 470 nm at the edge of the pattern. The different phase retardation at each position originates from the different LC hybrid alignment. At a given position, the shorter wavelength exhibits a higher phase retardation because of the birefringence dispersion, i.e.,  $\Delta n(\lambda)$  is higher at a shorter  $\lambda$ .<sup>69</sup>

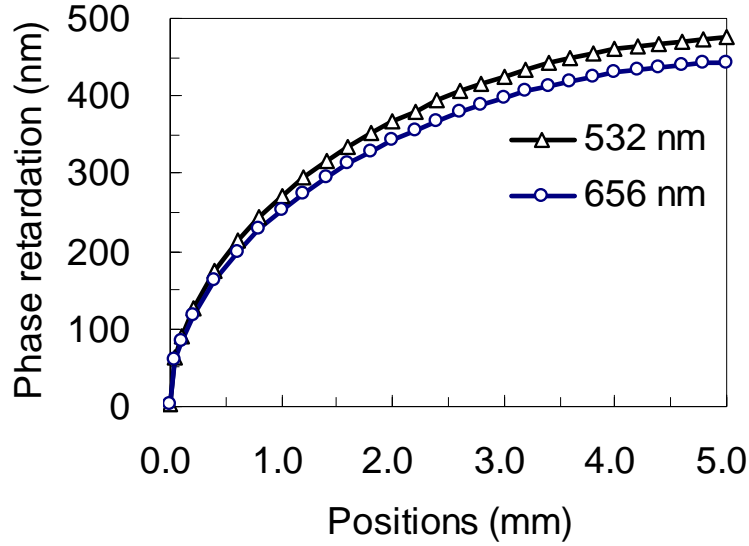


Figure 75: Phase retardation ( $d\Delta n$ ) profile of the axially-symmetric SPNLC layer. Cell gap  $d=9\ \mu\text{m}$ .

Then we overlay a phase compensation film, whose retardation value and optic axis are yet to be determined, on top of our SPNLC film. Figure 76(a) depicts the experimental setup. To demonstrate this powerful technique, we used a quarter-wave plate with an arbitrary axis as an example. Figure 76(b) shows the concept of our measurement methods. We put our sample and SPNLC film under an optical microscope and took images from a CCD camera. All we need to do is to look for the compensated dark spots of the stacked SPNLC and  $\lambda/4$  films. Since our SPNLC has continually varying retardation values, we can always find a point that would cancel the phase of our measured object. At the same time, we can also determine the optical axis of the tested object. For example, Figure 76(b) shows that the slow axis of the SPNLC is compensated with the fast axis of the  $\lambda/4$  film. After analyzing the CCD image, we obtain the direction of the fast axis of the object under study. Furthermore, we can obtain the phase

retardation value of the measured object by comparing the location of the dark spots with respect to the SPNLC phase retardation chart plotted in Figure 75.

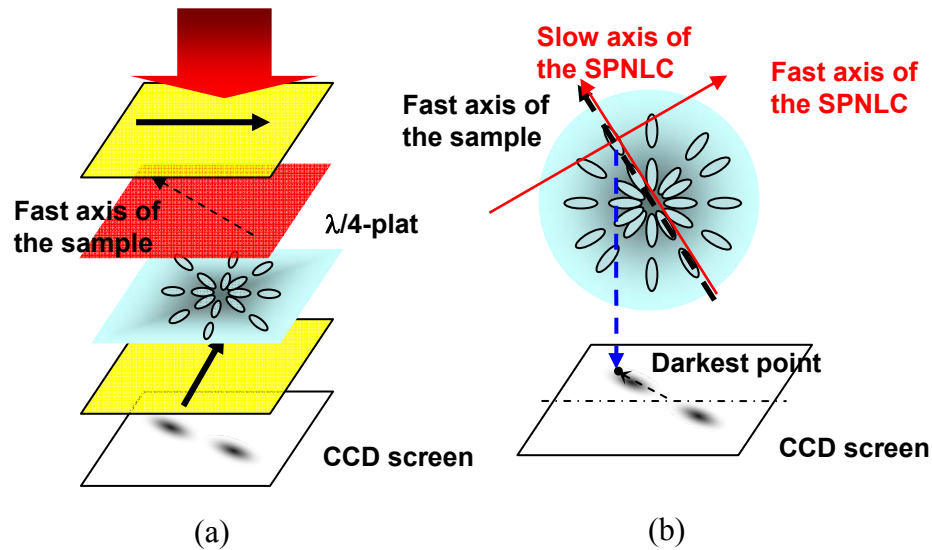


Figure 76: (a) Measurement setup and (b) illustration of the measurement methods.

Figure 77 shows the measurement setup of the C-plate. The measurement method is similar to the A-plate measurement in previous description. To measure the phase retardation of the C-plate, we need to obtain the  $30^\circ$  and  $45^\circ$  tilt retardation information and calculate by the following equations.

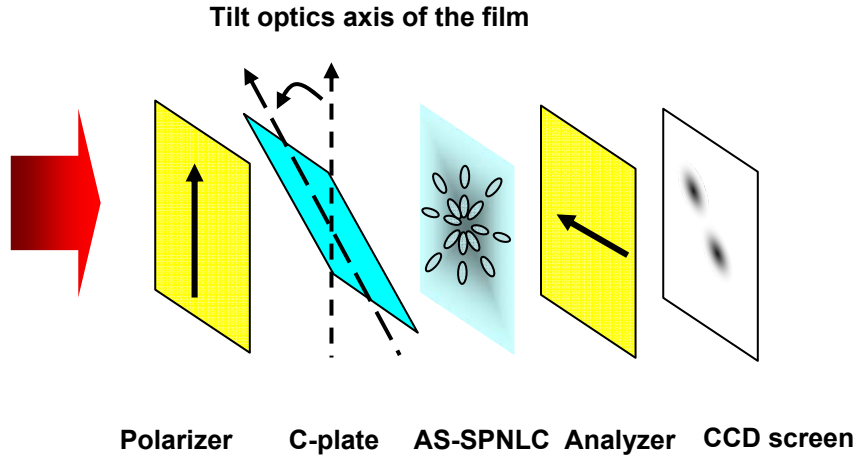


Figure 77: The measurement setup of the C-plate

The equations (11) and (12) show the retardation value with the relation to the birefringence ( $n_e$ ,  $n_o$ ) and thickness ( $d$ ) of the C-plate.  $\Gamma_{30}$  and  $\Gamma_{45}$  represent the retardation value when we flip over the C-plate to  $30^\circ$  and  $45^\circ$  with respect to the original position.

$$\Gamma_{30} = \frac{2\sqrt{3}}{3} \left( \sqrt{\frac{4 \cdot n_e^2 \cdot n_o^2 \cdot d^2}{3 \cdot n_e^2 + n_o^2}} - n_o \cdot d \right) \text{ (nm)} \quad (11)$$

$$\Gamma_{45} = \sqrt{2} \cdot \left( \sqrt{\frac{2 \cdot n_e^2 \cdot n_o^2 \cdot d^2}{n_e^2 + n_o^2}} - n_o \cdot d \right) \text{ (nm)} \quad (12)$$

To extract the retardation value of the C-plate from the equations (11) and (12), we substitute  $n_e = n_o + \Delta n$ ,  $R = d \times \Delta n$  and  $R_o = d \times n_o$ . The equations (13) and (14) show the relationship between the retardation value ( $\Gamma_{30}$  and  $\Gamma_{45}$ ) and  $R$ . After obtaining the retardation value  $\Gamma_{30}$  and  $\Gamma_{45}$  at  $30^\circ$  and  $45^\circ$ , we can determine the retardation value  $R$  of the C-plate by solving the equations (13) and (14).



$$\Gamma_{30} = \frac{4\sqrt{3} \cdot (R_o^2 - R_o \cdot R)}{3\sqrt{4 \cdot R_o^2 - 6 \cdot R_o \cdot R + 3 \cdot R^2}} - \frac{2\sqrt{3}}{3} R_o \quad (13)$$

$$\Gamma_{45} = \frac{2 \cdot (R_o^2 - R_o \cdot R)}{\sqrt{2 \cdot R_o^2 - 2 \cdot R_o \cdot R + R^2}} - \sqrt{2} R_o \quad (14)$$

### 7.5.3 Experimental results

Figure 78 (a) shows the transmitted image between crossed polarizers, which is recorded by a CCD camera. The employed light source is incoherent white light with a red ( $\lambda \sim 656$  nm) color filter. We could convert the measured phase compensation pattern of the CCD image to transmittance by a computer program. Figure 78 (b) plots the transmittance distribution corresponding to the measured results shown in Figure 78 (a). From Figure 78 (b), there are two transmission minima, represented by the blue color. This is because the alignment of the liquid crystal directors is  $180^\circ$  symmetric. Therefore, there are two completely compensated points in the image.

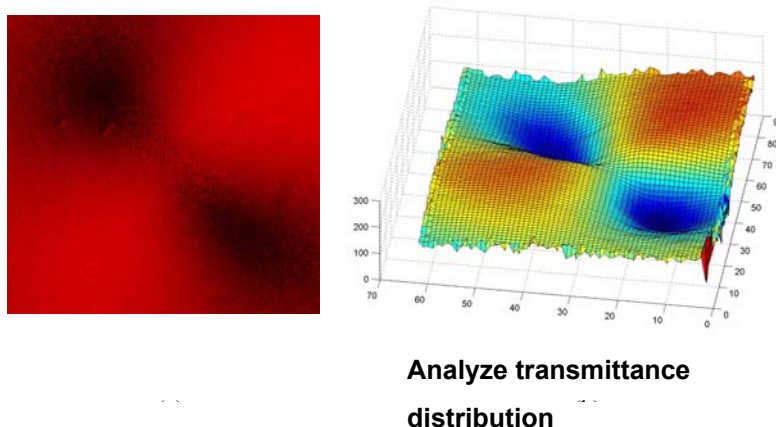


Figure 78: (a) The transmitted image recorded by a CCD camera, and (b) the converted transmittance distribution.

To extract the phase retardation value and optical axis of the compensation film from Figure 78, we need to find the fast axis and the distance of the transmission minima from the center, as illustrated in Figure 79(a). From Figure 79 (a), the fast axis (white dashed lines) is at  $135^\circ$  with respect to the horizontal axis. That means the optical axis of the uniaxial compensation film is oriented at  $135^\circ$  with respect to the horizontal axis. Next, we need to determine the  $d\Delta n$  value of the compensation film. To do so, we measure the distance of the transmittance minima from the center. From Figure 79 (a), we find that these two dark spots are quite symmetric; their distance to the center is  $\sim 399 \mu\text{m}$ . Next, we need to convert the measured distance to phase retardation from a corresponding phase retardation chart at a selected wavelength. The procedure is shown in Figure 79 (b). Figure 79 (b) plots the phase retardation value of the axially-symmetric SPNLC cell we fabricated. At the indicated position, we find the corresponding phase

retardation value is 162.1 nm. This is in a very good agreement with the expected quarter-wave plate, whose retardation value is 163.8 nm at  $\lambda = 656$  nm.

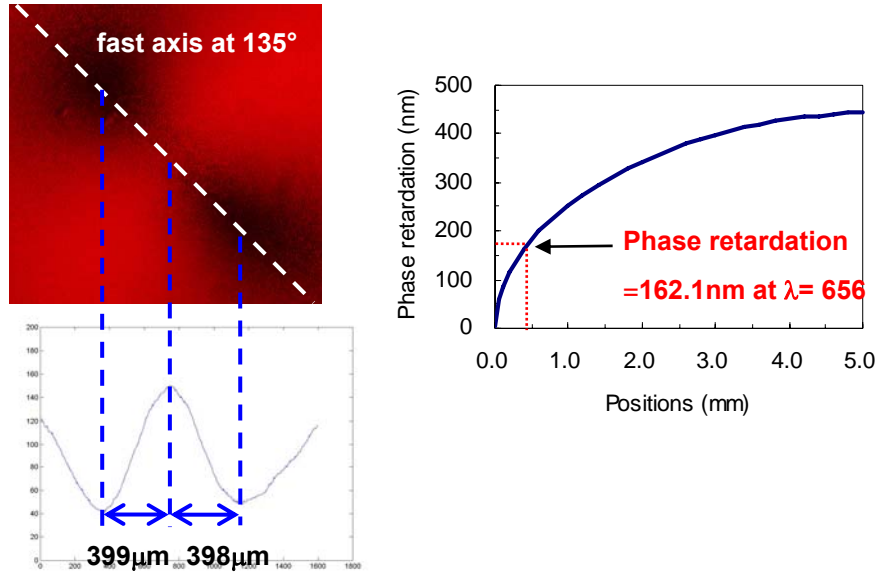


Figure 79: (a) The relative distance of the two transmission minima recorded by a CCD camera. (b) The corresponding phase retardation of the quarter-wave film.

### 7.5.4 Discussions

When we overlay a uniaxial film on top of the axially-symmetric SPNLC cell, the phase could be subtractive or additive depending on the optical axis of the uniaxial film. Both phase cancellation and accumulation could lead to the dark spots observed in Figure 79 (a). Phase cancellation occurs when the slow axis of the referenced SPNLC ( $\Gamma_{R,slow}$ ) is parallel to the fast axis of the sampled uniaxial film ( $\Gamma_{S,fast}$ ). At the transmission minima, the net phase retardation is zero:

$$\Gamma_{R,slow} - \Gamma_{S,fast} = 0 \quad (15)$$

Therefore, the dark spots represent that the phase retardation of the sample is equal to that of the SPNLC at the wavelength of measurement. The procedures for obtaining the phase retardation of the uniaxial film are illustrated in Figure 79.

The slow axis of a uniaxial film is  $90^\circ$  with respect to its fast axis. Therefore, in the orthogonal direction the phase of the slow axis of the sampled uniaxial compensation film  $\Gamma_{S,slow}$  is additive to the slow axis of the referenced SPNLC cell ( $\Gamma_{R,slow}$ ). When the total phase retardation equals to  $m\lambda$  (where  $m$  is an integer 1, 2, 3, etc) dark spots appear:

$$\Gamma_{R,slow} + \Gamma_{S,slow} = m\lambda \quad (16)$$

From Eq. (2), the positions of the dark spots are wavelength dependent. The wavelength information is needed for calculating the phase retardation of the measured sample,  $\Gamma_{S,slow}$ .

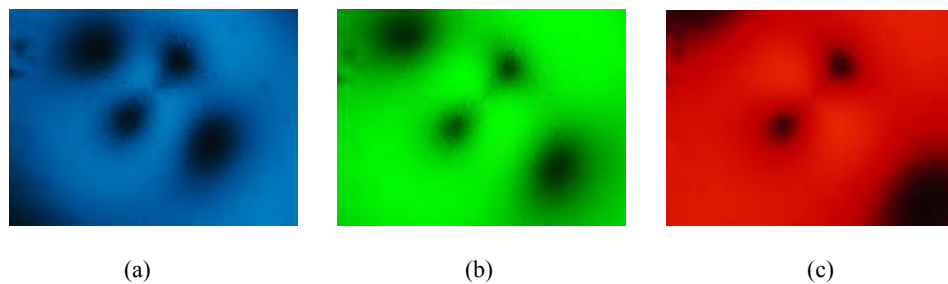
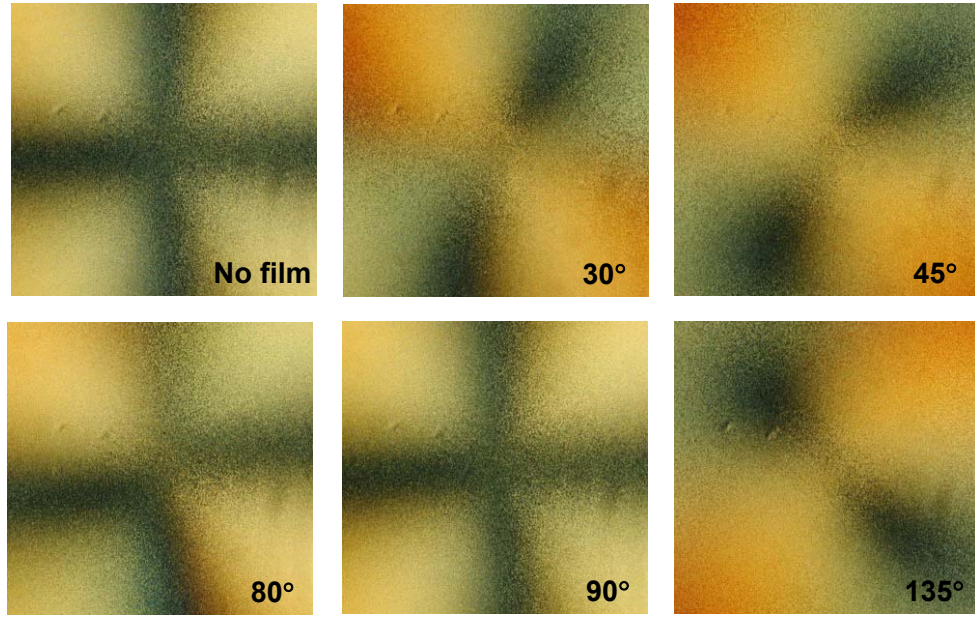


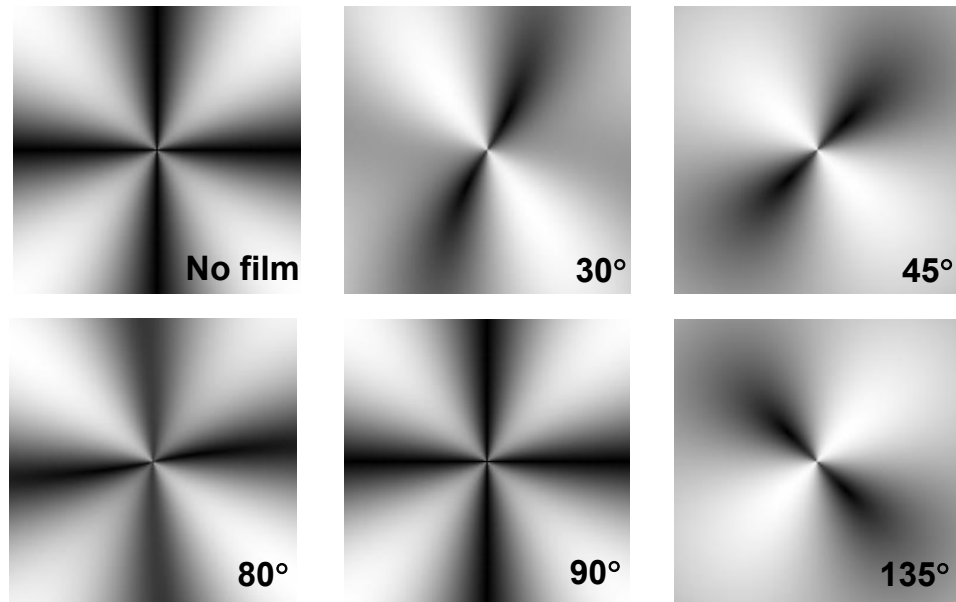
Figure 80: CCD images taken under three different color filters (a) 486 nm, (b) 532 nm, and (c) 632 nm.

Figure 80 shows the CCD images taken under three different color filters:  $\lambda=486$  nm, 532 nm and 632 nm. The fast axes in Figure 80 are along  $45^\circ$  with respect to the horizontal axis. The dark spots locate in the  $45^\circ$  axes present the phase cancellation at the compensated points. They change slightly as the wavelength changes due to the dispersion of the SPNLC film. On the other hand, the dark spots located at the  $135^\circ$  axes stand for the phase accumulation at the compensated points. The distance of the dark spots increases noticeably as the wavelength increases from blue, to green, and then to red.

The phase cancellation method is a better and more reliable approach to measure the phase retardation. This is because the result is more straightforward and does not need additional calculation and wavelength information. Figure 81(a) is a an example of dynamic image with a rotation of a quarter wave plate under the white light illumination. After analyzing the image data from the movie, we can simultaneously obtain the rotation angles of the optical axis and the phase retardation values. We then constructed a model based on the results obtained in Figure 81 (a). Figure 81 (b) shows the simulated results based on Figure 81 (a). The simulation shows the same trend as the quarter-wave plate rotates from  $0^\circ$  to  $135^\circ$ . The simulation results agree quite well with our experiment.



(a)



(b)

Figure 81: (a) A series of pictures show the real dynamic image changes when the quarter-wave plate rotates at different angles; and (b) The simulation results show the same trend when we rotate the slow axis of the quarter-wave plate from  $0^\circ$  to  $135^\circ$ .

## **7.6 Other applications**

### **7.6.1 Spatial polarization converter**

In the beginning of this chapter, we mention that an axially-symmetric liquid crystal structure can be used as a wavelength selection Fabry-Perot filter and a spatial polarization converter. This is because an axially-symmetric LC structure has particularly attractive feature of the symmetrical LC directors in the radial directions. Hence, we can use it as an optical device which is independent of linearly polarized light in the azimuthal angles because it is insensitive to the polarization change.

In order to understand the polarization converter, we need to define the spatial polarization first.<sup>14</sup> This is the geometric-optic properties of a linearly polarized light with axial symmetry characteristics. The polarization orientation  $\phi(\theta)$  of such an optical field depends only on the azimuthal angle  $\theta$ , and it can be written as


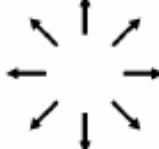


$$\phi(\theta) = P\theta + \phi_0 \quad (17)$$

The integer  $P$  is the polarization order number of the polarized light field.  $P$  is the number of polarization rotations ( $P=1,2,\dots,N$ ), and  $\phi_0$  is the initial polarization orientation for  $\theta = 0$ . The light field can also be explained by a Jones vector  $J$ :

$$J(\theta) = \begin{bmatrix} \cos(P \cdot \theta + \phi_0) \\ \sin(P \cdot \theta + \phi_0) \end{bmatrix} \quad (18)$$

Table 3 shows the spatial polarized light with axially symmetry properties. For example,  $P=1$  represent the radially polarized light and  $P=2$  means the azimuthally polarized light. Figure 82 shows the polarized light of orders ( $P = 1, 2, 3$ ) analyzed with a linear polarizer.

Table 3: Linear polarized light with axially symmetry properties

$P = -1$	$P = 1$	$P = 1$	$P = 2$
	Radially polarized light	Azimuthally polarized light	
			

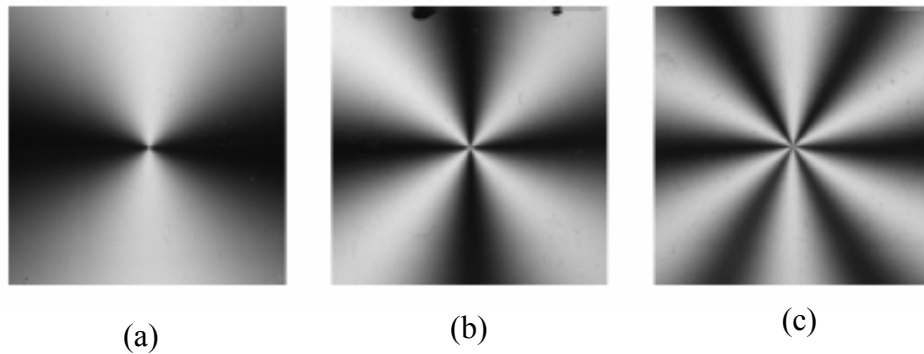


Figure 82: Polarized light of orders (a)  $P = 1$ , (b)  $P = 2$ , and (c)  $P = 3$  analyzed with a linear polarizer

Several approaches for achieving this kind of spatial polarization characteristic have been explored. Figure 83 shows the generation of radially and azimuthally polarized lights using circularly rubbed LC cells. This cell structure consists of one unidirectional and one circularly rubbed alignment layer. The local LC orientation in the cell is that of a twisted cell with a variable twist angle defined by the local alignment layers. As long as the cell gap is large enough, the incident polarized light can follow the rotation of the liquid crystal director, which is also called “adiabatic following”. Therefore, the output light in Figure 83 becomes a spatially polarized light.



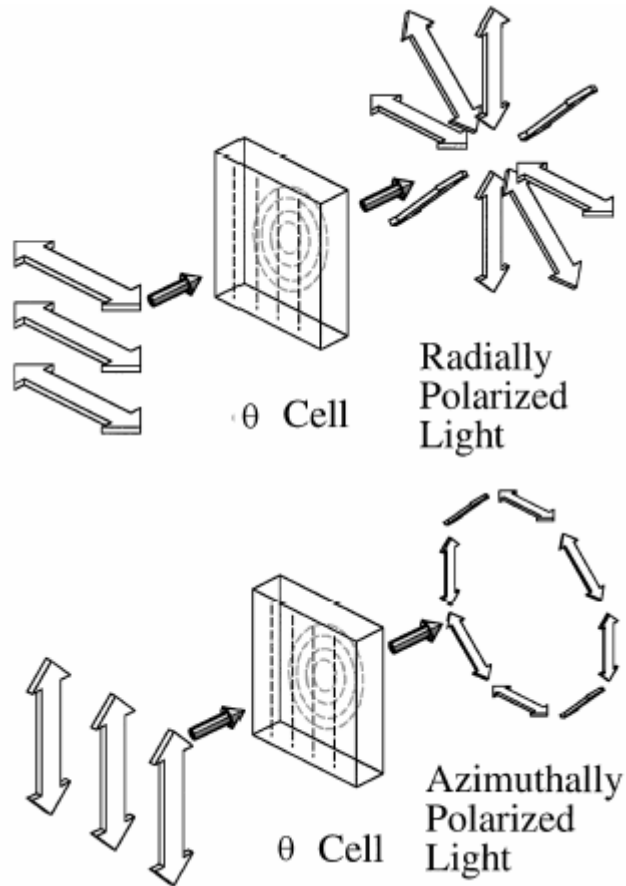


Figure 83: Methods for generating the radially and azimuthally polarized light using circularly rubbing cell.

Another approach is to use interference of two linearly polarized beams.<sup>16</sup> Figure 84 shows the method for generating a spatially polarized light using interference of two linearly polarized beams. The spatially polarized light is created by using two orthogonal polarization states, modifying appropriately their intensity and phase profiles, and recombining the states. Actually, the principle shows that we can create any arbitrary polarization state using this interference approach.

The major shortcoming of this method is the relatively low light efficiency and complicated fabrication process. Others use special LC cells with circular rubbing or

subwavelength gratings to realize the radially or azimuthally polarized light. However, these approaches require a complicated fabrication procedure such as circular rubbing or micro-fabrication process.

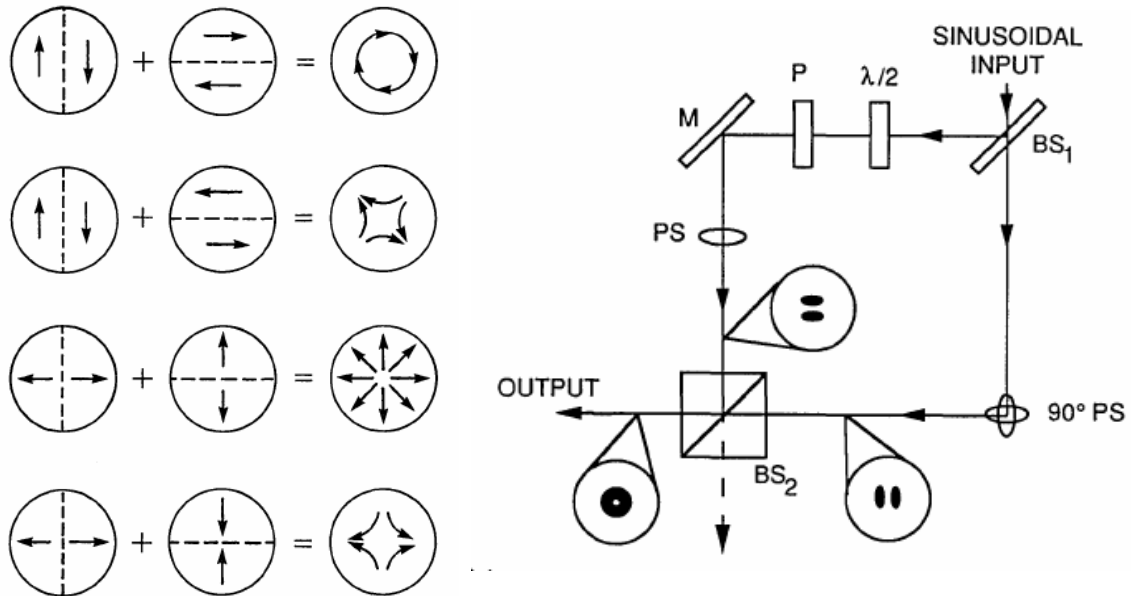


Figure 84: Generation of the spatial polarized light using interference of two linearly polarized beams.

In this section, we report a new axially-symmetric sheared polymer network liquid crystal (AS-SPNLC) for a spatial polarization converter. For example, we can make a rotationally symmetric half-wave plate using the axially-symmetric SPNLC cell if its average  $d\Delta n$  value is equal to  $\lambda/2$ <sup>14</sup>. Figure 85 shows the concept of such a polarization converter for the case of  $P=2$ ; where  $P$  is the polarization order number of the polarized light field<sup>14</sup>. In Figure 85 (a), we illuminate a linearly polarized light to this device. The rotationally half-wave plate shown in Figure 85 (b) would rotate the linearly polarized light to a different angle in each position. This is because the  $\lambda/2$  wave plate in each position rotates the linearly polarized light to twice the angle which is between the

incoming linear polarized light direction and the slow axis. Therefore, the output polarization, as shown in Figure 85 (c) is converted to a circularly symmetric but linearly polarized light field ( $P=2$ ). Thus, the proposed axially-symmetric SPNLC cell will act as a spatial polarization converter.

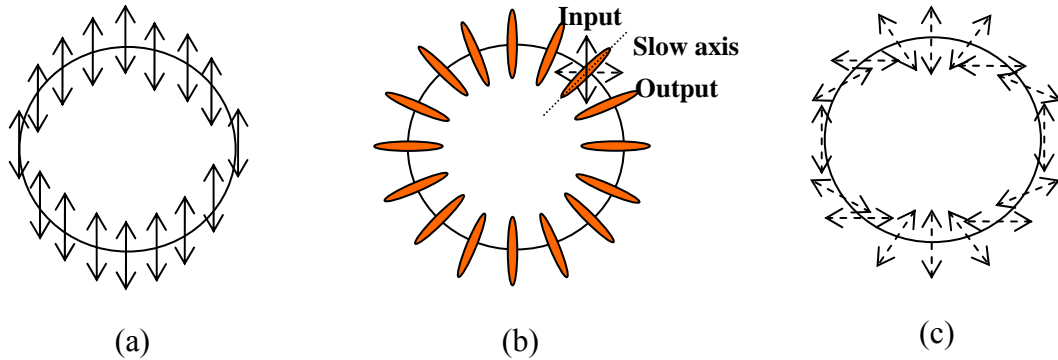


Figure 85: (a) Incident light with vertical linear polarization, (b) Rotationally symmetric half wave plate, and (c) Output light with polarization  $P=2$  field.

### 7.6.2 Tunable-focus liquid crystal lens

Another interesting application is the tunable-focus LC lens. The axially-symmetric SPNLC device has potential application as a tunable-focus lens and a spatial polarization converter. For instance, by illuminating with a radially polarized light<sup>70</sup> the axially-symmetric SPNLC cell functions like a tunable-focus lens. At  $V=0$ , the cell has a natural gradient phase profile from the center to the edge, as shown in Figure 58 so that the lens effect appears. As the voltage increases, the phase profile becomes flatter and the lens effect is gradually vanishing. Since the structure is axially symmetric,

the lens performance is independent of the incident light polarization, as shown in Figure 86.

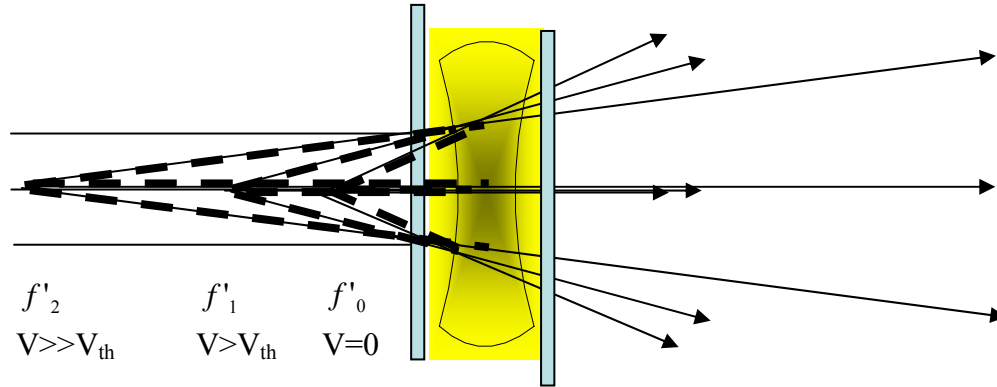


Figure 86: A tunable-focus lens using AS-SPNLC

## 7.7 Conclusion

We have demonstrated an axially-symmetric SPNLC structure for polarization independent photonic devices. The structure of the axially-symmetric SPNLC is analyzed by measuring the birefringence, V-T curve, and response time at different radial positions of the cell. We also constructed a 3D model based on the simulation results. The results agree well with our experiment.

We also developed a new method to measure the phase retardation and the optical axis simultaneously using an axially-symmetric SPNLC layer. To prove principle, a quarter-wave film was used as an example for demonstrating the measurement procedures. The measured results agree with theory well. This method is particularly

attractive for those optical systems whose optical axis and phase retardation are dynamically changing.

## LIST OF REFERENCES

1. S. T. Wu and D. K. Yang: *Reflective Liquid Crystal Displays* (Wiley, New York, 2001).
2. S. Gauza, H. Wang, C. H. Wen, S. T. Wu, A. J. Seed and R. Dąbrowski, “High birefringence isothiocyanato-tolane liquid crystals,” *Jpn. J. Appl. Phys. Part 1* **42**, 3463-3466 (2003).
3. R. A. M. Hikmet, “Electrically induced light scattering from anisotropic gels,” *J. Appl. Phys.*, **68**, 4406-4412 (1990).
4. Y. Q. Lu, F. Du, Y. H. Lin and S. T. Wu, “Variable optical attenuator based on polymer-stabilized twisted nematic liquid crystal,” *Opt. Express* **12**, 1221-1227 (2004).
5. F. Du, Y. Q. Lu, H. W. Ren, S. Gauza, and S. T. Wu, “Polymer-stabilized cholesteric liquid crystal for polarization-independent variable optical attenuator,” *Jpn. J. Appl. Phys.* **43**, 7083–7086 (2004).
6. F. Du, S. Gauza, and S. T. Wu, “Influence of curing temperature and high birefringence on the properties of polymer-stabilized liquid crystals,” *Opt. Express* **11**, 2891-2896 (2003).
7. J. L. West, G. Zhang, and A. Glushchenko, “Stressed liquid crystals for electrically controlled fast shift of phase retardation,” *Soc. Information Display, Tech. Digest* **34**, 1469-1471 (2003).

8. Y. H. Fan, Y. H. Lin, H. Ren, S. Gauza, and S. T. Wu, "Fast-response and scattering-free polymer network liquid crystals for infrared light modulators," *Appl. Phys. Lett.* **84**, 1233 (2004).
9. O. A. Aphonin, Y. V. Panina, A. B. Pravdin, and D. A. Yakovlev, "Optical-properties of stretched polymer-dispersed liquid-crystal films," *Liq. Cryst.* **15**, 395-407 (1993).
10. I. Amimori, J. N.Eakin, G. P.Crawford, N. V.Priezjev, and R. A. Pelcovits, "Optical and mechanical properties of stretched PDLC films for scattering polarizers," *Soc. Information Display, Tech. Digest* **33**, 834-837 (2002)
11. P. Sixou, C. Gautier, and H. Villanova, "Nematic and cholesteric PDLC elaborated under shear stress," *Mol. Cryst. Liq. Cryst.* **364**, 679-690 (2001).
12. J. H. Lee, H. R. Kim, and S. D. Lee, "Polarization-insensitive wavelength selection in an axially symmetric liquid-crystal Fabry-Perot filter," *Appl. Phys. Lett.* **75**, 859-861 (1999).
13. R. Yamaguchi, T. Nose, and S. Sato, "Liquid crystal polarizers with axially symmetrical properties," *Jpn. J. Appl. Phys.* **28**, 1730-1731(1989).
14. M. Stalder and M. Schadt, "Linearly polarized light with axial symmetry generated by liquid-crystal polarization converters," *Opt. Lett.* **21**, 1948-1950 (1996)
15. A. Niv, G. Biener, V. Kleiner, and E. Hasman, "Formation of linearly polarized light with axial symmetry by use of space-variant subwavelength gratings," *Opt. Lett.* **28**, 510-512 (2003)
16. S. C. Tidwell, D. H. Ford, and W. D. Kimura, "Generating radially polarized beams interferometrically," *Appl. Opt.* **29**, 2234-2239 (1990).

17. Y. H. Wu, Y. H. Lin, Y. Q. Lu, H. Ren, Y. H. Fan, J. R. Wu and S. T. Wu "Submillisecond response variable optical attenuator based on sheared polymer network liquid crystal," *Optics Express*, **12**, 6377-6384 (2004).
18. E. Hecht, *Optics*, (Addison Wesley, New York, 2002).
19. T. Oakberg, "Measurement of low-level strain birefringence in optical elements using a photoelastic modulator," in *International Symposium on Polarization Analysis and Applications to Device Technology*, T. Yoshizawa and H. Yokota, eds., Proc. SPIE **2873**, 17-20 (1996).
20. T. Oakberg, "Measurement of waveplate retardation using a photoelastic modulator," in *Polarization: Measurement, Analysis, Remote Sensing*, D. H. Goldstein and R. A. Chipman, eds., Proc. SPIE **3121**, 19-22, (1997).
21. S. Nakadate, "High precision retardation measurement using phase detection of Young's fringes," *Appl. Opt.* **29**, 242-246 (1990).
22. Y. L. Lo and P. F. Hsu, "Birefringence measurements by an electro-optic modulator using a new heterodyne scheme," *Opt. Eng.* **41**, 2764-2767 (2002).
23. Y. H. Wu, Y. H. Lin, H. Ren, X. Nie, J. H. Lee, and S. T. Wu, "Axially-symmetric sheared polymer network liquid crystals" , *Opt. Express* **13**, 4638-4644 (June 13, 2005).
24. G. W. Gray *Introduction and Historical Introduction in Physical Properties of Liquid Crystals*, editors D. Demus, J. Goodby, G. W. Gray, H. W. Spiess, and V. Vill page 1 Wiley-VCH, New York (1998).
25. F. Reinitzer *Montash. Chem.* **9**, 421 (1888).
26. G. Friedel *Ann. Physique.* **18**, 273 (1922).



27. M. J. Escuti, C. C. Bowley, G. P. Crawford, and S. Zumer, "Enhanced dynamic response of the in-plane switching liquid crystal display mode through polymer stabilization," *Applied Physics Letters* **75** (21), 3264-3266 (1999).
28. M. Hasegawa, "Response time improvement of the in-plane-switching mode," *SID Symposium Digest* **28**, 699 (1997).
29. R. A. M. Hikmet, "Electrically induced light-scattering from anisotropic gels with negative dielectric anisotropy," *Molecular Crystals and Liquid Crystals* **213**, 117-& (1992).
30. G. P. Crawford and S. Zumer, *Liquid crystal in complex geometries*. (Taylor & Francis, London, 1996).
31. Y. K. Fung, D. K. Yang, S. Ying, L. C. Chien, S. Zumer, and J. W. Doane, "Polymer networks formed in liquid-crystals," *Liquid Crystals* **19** (6), 797-801 (1995).
32. R.-Q. Ma and D.-K. Yang, "Fréedericksz transition in polymer-stabilized nematic liquid crystals," *Physical Review E* **61** (2), 1567-1573 (2000).
33. M. Xu, W. Feng, T. Huang, K. Wu, and J. Wu, "Liquid-crystal applications in optical telecommunication," in *Liquid Crystal Materials, Devices, and Applications IX*, L. C. Chien, ed., *Proc. SPIE* **5003**, 121-129 (2003).
34. L. Eldada: *Review of Scientific Instruments* **75** (2004) 575.
35. J. J. Pan, H. Wu, W. Wang, X. Qiu, and J. Jiang, "Temperature independent, accurate LC VOA through electric feedback control," in *Proceedings of National Fiber Optics Engineers Conference* (Telcordia, Orlando, Florida, 2003), pp. 943-949.
36. N. A. Riza and S. F. Yuan: *J. Lightwave Technol.* **17** (1999) 1575.
37. S. T. Wu and U. Efron: *Appl. Phys. Lett.* **48** (1986) 624.

38. V. V. Belyaev, S. Ivanov and M. F. Grebenkin: *Sov. Phys. Crystallogr.* **30** (1985) 674.
39. S. T. Wu, U. Efron and A. M. Lackner: *Appl. Opt.* **26** (1987) 3411.
40. H. K. Bucher, R. T. Klingbiel, and J. P. Van Meter, "Frequency-addressed liquid crystal field effect," *Appl. Phys. Lett.* **25**, 186-188 (1974).
41. M. Schadt, "Low-frequency dielectric relaxation in nematics and dual-frequency addressing of field effects," *Mol. Cryst. Liq. Cryst.* **89**, 77-92 (1982).
42. M. Xu and D. K. Yang: *Appl. Phys. Lett.* **70** (1997) 720.
43. I. C. Khoo and S. T. Wu: *Optics and Nonlinear Optics of Liquid Crystals* (World Scientific, Singapore, 1993).
44. S. T. Wu, "A nematic liquid crystal modulator with response time less than 100  $\mu$ s at room temperature," *Appl. Phys. Lett.* **57**, 986-988 (1990).
45. S. T. Wu: *J. Appl. Phys.* **73** (1993) 2080.
46. R. Ozaki, Y. Matsuhisa, M. Ozaki, and K. Yoshino, *Appl. Phys. Lett.* **84**, 1844 (2004).
47. U. Efron, *Spatial Light Modulator Technology* (Dekker, New York, 1995).
48. P. F. McManamon, T. A. Dorschner, D. L. Corkum, L. Friedman, D. S. Hobbs, M. Holz, S. Liberman, H. Q. Nguyen, D. P. Resler, R. C. Sharp, and E. A. Watson, *Proc. IEEE* **84**, 268 (1996).
49. C. Mao, M. Xu, W. Feng, T. Huang, K. Wu, and J. Liu, *Proc. SPIE* **5003**, 121 (2003).
50. M. Schadt and W. Helfrich, *Appl. Phys. Lett.* **18**, 127 (1971).
51. M. F. Schiekkel and K. Fahrenschon, *Appl. Phys. Lett.* **19**, 391 (1971).
52. S. T. Wu and U. Efron, *Appl. Phys. Lett.* **48**, 624 (1986).

53. A. B. Golovin, S. V. Shiyonovskii, and O. D. Lavrentovich, *Appl. Phys. Lett.* **83**, 3864 (2003).
54. S. Matsumoto, M. Kawamoto, and K. Mizunoya, *J. Appl. Phys.* **47**, 3842 (1976).
55. J. P. Drolet, J. S. Patel, K. G. Haritos, W. Xu, A. Scherer, and D. Psaltis, *Opt. Lett.* **20**, 2222 (1995).
56. S. T. Wu, U. Efron, and L. D. Hess, *Appl. Opt.* **23**, 3911 (1984).
57. S. T. Wu, *Appl. Phys. Lett.* **57**, 986 (1990).
58. A. Au, C. S. Wu, S. T. Wu, and U. Efron, *Appl. Opt.* **34**, 281 (1995).
59. J. H. Kim, M. Yoneya, and H. Yokoyama, *Nature (London)* **420**, 159 (2002).
60. R. A. M. Hikmet and H. J. Boots, "Domain structure and switching behavior of anisotropic gels," *Phys. Rev. E* **51**, 5824-5831 (1995).
61. H. Ren and S. T. Wu, "Anisotropic liquid crystal gels for switchable polarizers and displays," *Appl. Phys. Lett.*, **81**, 1432-1434 (2002).
62. R. A. Soref and D. H. McMahon, "Total switching of unpolarized fiber light with a four-port electro-optic liquid-crystal device," *Opt. Lett.* **5**, 147-149 (1980).
63. E. G. Hanson, "Polarization-independent liquid-crystal optical attenuator for fiberoptics applications," *Appl. Opt.* **21**, 1342-1344 (1982).
64. K. Hirabayashi, M. Wada, and C. Amano, "Optical-fiber variable-attenuator arrays using polymer-network liquid crystal," *IEEE Photon. Technol. Lett.*, **13**, 487-489 (2001).
65. F. Du and S. T. Wu, "Curing temperature effects on liquid crystal gels," *Appl. Phys. Lett.*, **83**, 1310-1312 (2003).
66. S. T. Wu and C. S. Wu, "High speed liquid crystal modulators using transient nematic effect," *J. Appl. Phys.* **65**, 527-532 (1989).

67. R. A. Soref and D. H. McMahon, "Total switching of unpolarized fiber light with a four-port electro-optic liquid-crystal device," *Opt. Lett.* **5**, 147-149 (1980).
68. V. Vorflusev and S. Kumar, "Phase-separated composite films for liquid crystal displays" *Science* **283**, 1903-1905 (1999).
69. S. T. Wu, "Birefringence dispersion of liquid crystals," *Phys. Rev. A* **33**, 1270-1274 (1986).
70. A. V. Nesterov and V. G. Niziev, "Laser beams with axially symmetric polarization," *Phys. D: Appl. Phys.* **33**, 1817-1822 (2000).
71. Mughal MJ, Riza NA, "Compact acoustooptic high-speed variable attenuator for high-power applications", *IEEE Photo. Tech. Lett.* **14** (4): 510-512 (2002).
72. Riza NA, Yaqoob Z, "Submicrosecond speed variable optical attenuator using acoustooptics", *IEEE Photo. Tech. Lett.* **13** (7): 693-695 (2001).